ABSTRACT

Title of Dissertation: DEVELOPMENT OF A $ZnO/SiO_2/Si$ HIGH SENSITIVITY INTERLEUKIN-6 BIOSENSOR

Soumya Krishnamoorthy, Doctor of Philosophy, 2007

Dissertation Directed By: Agis A. Iliadis

Department of Electrical and Computer Engineering

Biosensors offer the opportunity to sense biological material providing valuable information for medical diagnostics and monitoring of pathogens in the environment. Thus the development of high sensitivity, cost effective, real-time and portable biosensors is of primary importance.

This thesis presents the development of a $ZnO/SiO_2/Si$ based CMOS compatible biosensor, for the real-time detection of interleukin-6 (IL-6). In this work, high quality ZnO films were grown on SiO_2/Si substrates by pulsed laser deposition. A protein immobilization procedure for binding the IL-6 protein to the ZnO active area was developed and the morphology of the bio-molecules was studied using SEM and AFM techniques for the first time. A modified solid-phase Enzyme linked Immunosorbent assay (ELISA) technique was developed to measure the mass of protein bound onto the oxide surface. The study resulted in a mass of 0.364 pg/ml of IL-6 bound onto ZnO for an applied mass of 0.5 ng/ml.

A guided shear mode surface acoustic wave (SAW) device in the $ZnO/SiO_2/Si$ system, with ZnO as the guiding layer on a SiO_2/Si substrate, was modeled and fabricated. Two devices, operating at 708 MHz (device A) and 1.5 GHz (device B) were

developed. The mass sensitivities of these devices were calibrated by applying a known copolymer mass in a window area opened in the SAW devices and by measuring the frequency shift due the application of the mass. The maximum mass sensitivity of devices A and B was 4.162 μm^2/pg and 8.687 (μm^2/pg) for ZnO guiding layer thickness of 340 nm and 160 nm respectively.

A technique to apply IL-6 directly onto the SAW sensor surface was developed. For an applied IL-6 mass ranging from 20ng/ml – 2 μg/ml, applied in a 20x20 μm^2 sensing area, the device measures IL-6 masses in the range of 1.2 fg-76.45 fg. A proof-of-concept experiment for the biosensor was setup with normal human serum to detect the presence of IL-6 in trace amounts. The device predicts three times as much IL-6 mass for normal human serum derived from pooled donors under the age of 55 as compared to that from a donor over the age of 55. This is understood to be the result of age related increased IL-6 levels and was independently confirmed through ELISA measurements. The ZnO/SiO_2/Si sensor system therefore enables highly sensitive mass detection of the IL-6 protein to be realized.

DEVELOPMENT OF A $ZnO/SiO_2/Si$ HIGH SENSITIVITY INTERLEUKIN-6 BIOSENSOR

by

Soumya Krishnamoorthy

Dissertation submitted to the Faculty of the Graduate School of the
University of Maryland, College Park in partial fulfillment
of the requirements of the degree of
Doctor of Philosophy
2007

Advisory Committee:

Professor Agis A. Iliadis, Advisor/Chair
Professor John Melngailis
Professor Martin Peckerar
Professor Robert Newcomb
Professor Lourdes Salamanca-Riba
Dr Thaleia Bei

DEDICATION

In memory of my mother, *Narmada Krishnamoorthy*

You are my inspiration

ACKNOWLEDGEMENTS

I am deeply indebted to my advisor, Agis Iliadis for introducing me to the field of bio-engineering and thank him for his academic and professional assistance through the years. I have learned much from his insights into science and the philosophy of research. Dr Thaleia Bei mentored me in aspects of bio-chemistry that were essential to my research and I thank her for her assistance in developing the protein immobilization technique as well as the ELISA measurements. I also appreciate the support of Dr George Chrousos of the National Institutes of Health (NIH) for assistance with the IL-6 functionalization techniques.

I would also like to thank my committee member, Dr Martin Peckerar for his generous guidance and encouragement throughout the course of my graduate career. Dr John Melngailis spared his time for several instructive discussions about SAW devices and characterization, which proved very valuable in my research and I am grateful to him. I would also like to thank Dr Newcomb and Dr Salamanca-Riba for taking their time to serve on my dissertation committee.

I also appreciate the support of Dr Emmanouil Zoumakis of the National Institutes of Health (NIH) for the ELISA measurements. I am thankful for the help of Dr Michael Fuhrer and Dan Lenski from the Department of Physics, with the AFM and SEM measurements. Thanks are due to Dr. George Metze, and Dr Junghwan Kim, of the Laboratory of Physical Sciences, for providing access to facilities and help with the SAW device characterization. I am grateful to the National Science Foundation (NSF) for funding my research.

I've often felt that without the assistance of Tom Loughran, the ECE (and now nanolab) clean room manager, I would have taken twice the amount of time to complete my work. From helping fix the SEM and PLD, to making sure we had everything we needed in the clean room, he has always been helpful and prompt.

My colleagues at the Semiconductor Research lab and the Department of ECE have given me tremendous amount of support over the years. In particular, I would like to thank Hasina Ali and Kyechong Kim for being a valuable sounding board for my research ideas, Thanos Chryssis for training me on the PLD and mentoring me when I first started my research and Kuldeep Amarnath for his many little nuggets of wisdom regarding PL measurements, lithography mask set designs, and semiconductor device physics.

On a personal note: Graduate school brought me into contact with some wonderful people and I would like to thank them for their help: Nicole Nelson, Hunghao Jiang, Somasekhar Prakash from the IBIS lab and my friends Kaveri Pant, Christopher Komareddy, Jothsna Rao, Ranjani Varadan, Deepa Poduval and Divya Muralidhar for many years of valued friendship.

My parents, Narmada and TS Krishnamoorthy have been my greatest source of inspiration and I am grateful to them for a lifetime of love, sacrifice and support. I would also like to thank my sisters Raji and Vijaya their constant encouragement and support through the years. And finally, a word about my wonderful husband, Vijesh, who coaxed, encouraged, tolerated, understood, and endured every up and down of graduate school. He makes it all worth it.

TABLE OF CONTENTS

List of Tables ……...viii

List of Figures ……ix

CHAPTER 1: INTRODUCTION 1

1.1 Biosensors: An Introduction 1

1.1.2. Gravimetric biosensors 2

1.2 ZnO Thin Film Gravimetric Sensors 5

1.2.1 Material Properties of ZnO 6

1.2.2 ZnO Gravimetric Sensors 7

1.3. Interleukin-6 7

1.4 Contributions 8

1.5 Organization of this Dissertation 10

CHAPTER 2 : PULSED LASER DEPOSITION OF ZnO THIN FILMS 12

2.1 Advantage of the Pulsed Laser Deposition Technique over other thin film deposition techniques 12

2.2 Pulsed Laser Deposition System 14

2.3 Growth Mechanism 16

2.4 Thin film Characterization techniques 18

2.4.1.1 X-ray Photoelectron Spectroscopy (XPS) 18

2.4.2 X-ray Diffraction Spectroscopy 19

2.4.3 Photoluminescence (PL) spectroscopy 21

2.4.4 Hall Effect Measurements 23

2.5 Growth and Characterization of Thin ZnO films on p-type (100)Si Substrates 25

2.6 Structural and Optical Characterization of ZnO/(100)Si films 27

2.7 Growth and Characterization of ZnO on SiO_2/Si substrates 36

2.8 Development of p-ZnO on (100)Si substrates 39

2.7.1 Growth of p-ZnO films and Hall Effect measurements 40

2.7.2 Electrical Conduction Model 45

2.9 Summary 47

CHAPTER 3 : DEVELOPMENT OF PROTEIN IMMOBILIZATION ON ZnO THIN FILMS 49
3.1 Protein functionalization techniques: Physical Adsorption Vs Covalent Binding 49
3.2 Choice of Substrate and Antigen 50
3.3 Human IL-6 Immunoassay- ELISA 52
3.3 Protein immobilization on ZnO/Si and SiO_2/Si substrates 53
3.3.1 Immobilization procedure 53
3.3.2 Modified Human IL-6 Immunoassay- ELISA set up 54
3.3.3 Morphology Evaluation During Protein Immobilization 55
3.3.4 Biochemical Analysis : Results from ELISA 63
3.4 Summary 66
CHAPTER 4 : DEVELOPMENT OF A GUIDED SHEAR HORIZONTAL SURFACE ACOUSTIC WAVE DEVICE 68
4.2 Development of a ZnO/SiO_2/Si Love Mode Surface Acoustic Wave Device 70
4.3 Frequency Response and SAW Parameter Evaluation 75
4.4. Study of SiO_2 Thickness on SAW Device Performance 78
4.5 Dispersion Relationship of a ZnO/SiO_2/Si Love-Mode-SAW system 81
4.5.1 Theoretical Modeling and Numerical Simulation 81
4.5.2 Experimental Verification of the Dispersion Relationship 85
4.6 Summary 87
CHAPTER 5 : DEVELOPMENT OF LOVE MODE SURFACE ACOUSTIC WAVE MASS TRANSDUCERS 89
5.1 Background 89
5.2 Mass Sensitivity of Acoustic Devices: An Introduction 89
5.3 Theoretical Formulation and Modeling of Perturbation Theory of Love Wave Devices 92
5.4 Experimental Verification of ZnO based LM-SAW mass sensitivity 98
5.5 Summary 102
CHAPTER 6 : A ZnO/SiO_2/Si IL-6 BIOSENSOR PROTOTYPE 105
6.1 Introduction 105

6.2 Protein immobilization procedure on the ZnO sensor surface..... 105
6. 3. Morphological Studies of IL-6 Binding..... 108
6.3.1 IL-6 attachment through antibody adsorption 109
6.3.2 IL-6 immobilization through covalent attachment of IL-6 antibody.. 109
6.4 Frequency Response and Mass measurements 113
6.4.1 IL-6 attachment through the antibody adsorption..... 113
6.4.2 IL-6 immobilization through BSA..... 115
6.4.3 IL-6 Immobilization through the IL-6 antibody 115
6.5 IL-6 Detection in Human Serum..... 119
6.6 Summary..... 120
CHAPTER 7 : CONCLUSIONS 122
7.1 Summary..... 122
7.2 Future Work..... 124
Bibliography 126

LIST OF TABLES

Table 2.1: Comparison of Thin film growth techniques 14
Table 3.1: Particle maximum height and lateral size distribution at each intermediary step of protein immobilization on ZnO and SiO_2 surfaces. 63
Table 3.2: Modified ELISA measurement of IL-6 specific binding on the ZnO and SiO_2 surfaces 64
Table 4.1: Geometric parameters for the two port LM-SAW resonator 74

LIST OF FIGURES

Figure 1.1: Optical detection mechanism 2
Figure 2.1: Schematic Diagram of a Pulsed Laser Deposition System 15
Figure 2.2: Schematic representation of the photoelectric process..... 18
Figure 2.3: Schematic illustration of the θ-2θ scan 20
Figure 2.4: Schematic of the Hall effect in a long, thin bar of semiconductor with four ohmic contacts. 23
Figure 2.5: Sticking Coefficient of ZnO on (100)Si 28
Figure 2.6: Room temperature PL spectrum of ZnO films grown on (100)Si substrates with an excitation wavelength of 280 nm. 29
Figure 2.7: Room temperature PL spectrum of ZnO films grown on (100)Si substrates with an excitation wavelength of 335 nm. 29
Figure 2.8: XPS spectrum of ZnO grown on (100) Si (a) low resolution spectrum (b) high resolution spectrum of the Zn($2p_{3/2}$) peak (c) high resolution spectrum of the O(1s) high resolution spectrum..... 30
Figure 2.9: . θ -2θ scan of ZnO grown on (100) Si. The (0002) ZnO.peak at 34.4^0 is visible at all temperatures. 32
Figure 2.10: Grain size variation vs deposition temperature of ZnO thin films on Si substrates at O_2 partial pressure of 10^{-4} Torr and laser fluence of 1.8 J/cm^2 32
Figure 2.11: XRD patterns of undoped ZnO thin films deposited on Si substrates at three different O_2 partial pressure values at 200^{o}C and laser fluence of 0.8 J/cm^2..... 33
Figure 2.12: θ -2θ scan of ZnO grown on (100) Si. Peaks from left to right are (100) ZnO and (002) ZnO. 34
Figure 2.13: XRD 2θ scan of ZnO/ITO grown on (100) silicon by PLD. 35
Figure 2.14: X-ray diffraction θ-2θ scan of a (100)Si substrate. 36
Figure 2.15: X-ray diffraction θ-2θ scan of (a) ZnO/SiO_2/(100)Si with SiO_2 thickness of 2000Å. The (0002) ZnO peak is at 35.2^0, indicating a highly strained film with a strain of 2.3%, ... 37

Figure 2.16: X-ray diffraction θ-2θ scan of (a) ZnO/SiO_2/(100)Si with SiO_2 thickness of 500Å. The (0002) ZnO peak is at 35.2^0, indicating a highly strained film with a strain of 0.56%. 39
Figure 2.17: Hall coefficient vs. O_2 partial pressure in ZnO films grown at various temperatures and laser fluencies. 41
Figure 2.18: Free carrier mobility and concentration curves as related to deposition temperature for undoped ZnO thin films grown on Si substrates at laser fluence of 1.8 J/cm^2 and O_2 partial pressure of 10^{-4} (⊖ and ●) and 10^{-5} Torr (⊟ and ■) respectively 42
Figure 2.19: Electrical resistivity results vs temperature for three ZnO films grown in O_2 pressures: $8x10^{-7}$ Torr (○), $1.5x10^{-6}$ Torr (Δ) and $1x10^{-4}$ Torr (■). 43
Figure 2.20:Hall coefficient vs temperature for ZnO films grown in O_2 pressures: $8x10^{-7}$ Torr (○), $1.5x10^{-6}$ Torr (Δ) and $1x10^{-4}$ Torr (■). The turning-points for R_H to switch sign are at 232, 231 and 242K, respectively..... 44
Figure 2.21: Temperature dependence of the carrier concentration (net values) plotted as ln(n or p $\cdot T^{-3/2}$) vs T^{-1} for ZnO films grown in O_2 partial pressures: $8x10^{-7}$ Torr (○), $1.5x10^{-6}$ Torr (Δ) and $1x10^{-4}$ Torr (■). The net values of the concentration (n or p) varied between $5x10^{20}$ and $1x10^{21}$ cm^{-3}. 45
Figure 2.22:Temperature dependence of the electrical conductivity plotted as lnσ vs T^{-1} for ZnO films grown in O_2 pressures: $8x10^{-7}$ Torr (○), $1.5x10^{-6}$ Torr (Δ) and $1x10^{-4}$ Torr (■). 47
Figure 3.1. A multi-well plate such as the one shown above might be used for ELISA. Positive and negative controls are included in the plate and give an indication of the luminescence required for the detection of the protein. Patient C tests positive for the protein while patient A tests negative 52
Figure 3.2: Schematic protocol for immobilization of interleukin-6 on ZnO and SiO_2. The hydroxylized surface of the oxides is silanized using ATES. The amino group generated by this process subsequently binds with the aldehyde (–CH=O) group from gluteraldehyde. This aldehyde group is used to make a covalent bond with the BSA and IL-6 binds electrostatically onto BSA. 57

Figure 3.3: SEM and AFM images of ATES bound onto ZnO/Si and SiO_2/Si samples. (a) SEM image of an 80x60μm^2 area on ZnO/Si indicating ATES particles. (b) The 2-D AFM image of a magnified portion (1.6x1.6μm^2 area) of the same ZnO surface (c) The 3-D AFM image of the same area as in (b) (d) The SEM image of an 80x60μm^2 area of ATES particles on SiO_2 (e) The 2-D AFM image of a magnified portion (5x5μm^2 area) of the SiO_2 surface. (f) The 3-D AFM image corresponding to the same portion as in (e) 58

Figure 3.4: SEM and AFM images of gluteraldehyde particles bound onto ATES. (a) The SEM image of a 20x15μm^2 area on ZnO indicating coagulated particles of gluteraldehyde and ATES. (b) The 2-D AFM image of a magnified portion (8.5x8.5μm^2 area) of gluteraldehyde on ATES on ZnO (c) The 3-D AFM image corresponding to the same area as seen in (b). (d) The SEM image of a 20x15μm^2 area on SiO_2 (e) The 2-D AFM image of a magnified portion (6x6μm^2 area) of the SiO_2 surface. (f) The 3-D AFM image of the same portion as seen in (e)..... 59

Figure 3.5: SEM and AFM images of BSA bound onto gluteraldehyde (a) SEM image of a 10x5μm^2 area on ZnO after the application of BSA. (b) 2-D AFM image of a 10x10μm^2 area of ZnO. (c) The 3-D AFM image corresponding to the same area as in (b) gives a maximum particle height of 1.53μm. (d) The SEM image of a 25x15μm^2 area on SiO_2 shows the BSA bound onto gluteraldehyde. (e) The 2-D image of a 10x10μm^2 portion of the SiO_2 surface with BSA bound to gluteraldehyde. (f) The 3-D AFM image of the same portion as seen in (e)..... 61

Figure 3.6: SEM and AFM images on application of IL-6. (a) SEM image of a 75x50μm^2 area on ZnO/Si indicating a large circular cluster with a diameter around 26μm. (b) The 2-D AFM image of magnified portion (20x20μm^2 area) of the ZnO surface. (c) The 3-D AFM image of this portion indicates a maximum height of 1.78μm for the particles. (d) The SEM image of a 75x50μm^2 area on SiO_2/Si, shows a large circular cluster similar but not as dense as that on ZnO, with typical sub-cluster size distribution of 2 to 5μm. (e) The 2-D AFM image of a magnified portion (3.2x3.2μm^2 area) of the SiO_2 surface. (f) The 3-D AFM image of the same portion indicating a maximum height of the particles of 748nm..... 62

Figure 4.1: Surface acoustic wave resonator with input and output inter-digitated (IDT) fingers. The mass loading causes a shift in the acoustic velocity and hence frequency of the resonator. 69
Figure 4.2: Schematic diagram of particle displacement for surface longitudinal and shear surface horizontal waves 70
Figure 4.3: Schematic diagram of the ZnO/SiO_2/Si LM-SAW device with axis orientations 71
Figure 4.4: The schematic top view of the SAW resonator with wavelength λ and aperture *W*. 73
Figure 4.5: Optical Image of LM-SAW resonator 74
Figure 4.6: SEM images of (a) device A with finger width of 1 μm and spacing of 2.4 μm (b) Device width and spacing of 0.8 μm. 75
Figure 4.7: Frequency response of LM-SAW ZnO/SiO_2/Si device A with finger width 1μm and finger spacing 2.4μm, generated a fundamental frequency of 708MHz with a harmonic at 1.41 GHz 76
Figure 4.8: Frequency response of device B with finger width and spacing of 0.8μm, generated a fundamental frequency of 1.50 GHz. 77
Figure 4.9: Effect of annealing on LM-SAW device performance. (a) device A fabricated on a 2000Å SiO_2. layer. Annealing causes a strain reduction to 2%, and a downward shift in the peak frequencies by 20 MHz. (b) device B fabricated on a 2000Å SiO_2 layer, indicating a similar downward frequency shift. 79
Figure 4.10: Definition of axes and propagation direction for shear horizontally polarized waves is a three-layered system, the displacement is in the x_2 direction. 81
Figure 4.11: The theoretical phase velocity curves as a function of normalized guiding layer thickness ($d/\lambda_l=df/v_l$) is shown. The first two modes of love waves are indicated for a device operating at a center frequency of 700 MHz. The Love mode waves propagate with a velocity varying between 5100 m/s (SiO_2) and 4814 m/s (ZnO). 84
Figure 4.12: Dependence of LM-SAW device frequency on ZnO guiding layer thickness. 86

Figure 4.13: Solid lines are the theoretical phase velocity curves as a function of normalized guiding layer thickness ($d/\lambda_l=df/v_l$). The dotted line represents the experimentally verified phase velocities of device A for the first Love wave mode..... 86
Figure 5.1: Theoretically determined mass Sensitivity, $|S_m|$, in 1/(pg /μm^2) for the first two Love modes shown in Fig 3 (a). The dotted line represents the mass sensitivity of a device operating at 1.5 GHz..... 95
Figure 5.2: The ratio of group to phase velocities evaluated for devices A and B given the mass sensitivities in Fig 5.1 97
Figure 5.3: Standard lithography was used to open windows between the IDTs for copolymer mass deposition..... 98
Figure 5.4: Copolymer thickness as a function of the spin casting speed 99
Figure 5.5: Mass Sensitivity measurements for devices A and B in 1/(pg/μm^2) for an applied polymer mass of 53.85fg and 0.861pg. (a) Device A achieves a maximum sensitivity of 4.283 while (b) device B achieves a maximum sensitivity of 8.89. 101
Figure 5.6: Frequency change for device A and B as a function of applied mass on a 5x5 $\mu^2 m$ area for a constant guiding layer thickness. The thickness of ZnO guiding layer is 340 nm for device A and 160nm for device B. 102
Figure 6.1: Optical Image of the window opening between the input and output IDTs of the SAW device. The ZnO surface in this region is exposed, while the remaining area is coated with 1813 Shipley positive resist. Protein immobilization is performed in this window. 108
Figure 6.2: SEM images taken during protein immobilization (a) SEM image upon application of the IL-6 antibody indicates a spherical particles of the antibody (b) The SEM image upon application of IL-6 onto the antibody indicates further clustering of IL-6 close to the antibody 110
Figure 6.3: SEM images taken during protein immobilization(a) SEM image upon application of ATES+ gluteraldehyde indicates coagulated particles of ATES and gluteraldehyde. (b) SEM image upon application of the IL-6 antibody indicates a cluster of the antibody that is attached to gluteraldehyde (c) The SEM image upon

application of IL-6 onto the antibody indicates further clustering of IL-6 close to the antibody 111
Figure 6.4: (a) Frequency shift vs adsorbed (antibody + IL-6) mass on the ZnO/SiO_2/Si guided shear acoustic wave sensor for devices A and B in a 5x5 μm^2 window (b) Measured vs adsorbed IL-6 mass on the sensor for devices A and B in a 5x5 μm^2 window..... 114

CHAPTER 1: INTRODUCTION

1.1 Biosensors: An Introduction

Biosensors are powerful tools aimed at providing selective identification of biological systems for biomedical diagnosis. Combining the specificity of biological recognition probes and the excellent sensitivity of various detection mechanisms, biosensors are capable of detecting and differentiating constituents of complex systems. They can thus provide unambiguous identification and accurate quantification of these constituents.

Biosensor development is based on combining the properties of biologically active materials with those of inorganic crystalline materials that translate the biological properties into electronic signals. These signals can then be processed to identify the biological elements. Some biological elements of interest are in trace concentrations (e.g. certain proteins in the blood, or airborne pathogens and toxins), thus requiring a highly sensitive and highly specific biosensor that can detect their presence directly and in real time in the field. Some of the important defining parameters of such an advanced biosensor are its high sensitivity and specificity to the targeted biological element(s) over an extended detection range, in a compact portable form of a card or a tag.

Past research in biosensors has largely concentrated in optical detection mechanisms [1-3], and a number of optical transduction techniques can be used for biosensor development [4-7]. Irrespective of the choice, all optical methods require an optically activated label for detection, which increases the complexity and cost of the method.

In optical biosensors, detection is performed through optically labeled probes. As see in figure 1.1, the antigen to be detected is bound to a label that luminesces at a

signature wavelength. The intensity of this luminescence is measured by a photo detector and the photocurrent generated is a measure of the amount of antigen present.

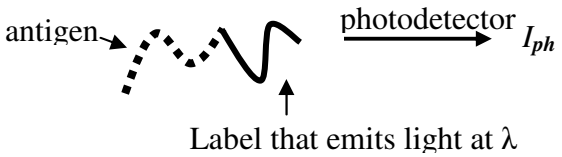

Figure 0.1: Optical detection mechanism

The photocurrent generated is very small and requires amplification, which is achieved through the use of photomultiplier tubes (PMT). These typically have high losses and introduce greater complexity into the system and thus increase cost [2,3]. To overcome this, active CMOS biosensor substrates for fluorescence-based assays that enable time-resolved fluorescence spectroscopy, without the need for an external reader have been developed [8,9]. However, all optical detection mechanisms necessitate the application of a fluorescent label, which makes the cost of detection prohibitive.

1.1.2. Gravimetric biosensors

Gravimetric biosensors are piezoelectric mass transducers, which achieve label-free detection of bio-molecules and are therefore an attractive alternative to optical biosensors. The fundamental concept of these piezoelectric devices is that upon application of the mass, the phase velocity of the acoustic wave decreases. This can be measured as a decrease in the resonant frequency of the piezoelectric resonator.

In 1959, Sauerbrey showed that the shift in resonance frequency of thickness-shear-mode (TSM) resonators is proportional to the deposited mass [10]. This was the starting point for the development of a new generation of piezoelectric mass-sensitive

devices. TSM resonators generate bulk acoustic waves and are typically low frequency (5-15 MHz), require simple instrumentation and exhibit a good signal to noise ratio [11-13]. Quartz TSM devices were used extensively for detecting bio-molecules such as living cells [14], bacteria [15] and proteins [16]. From Sauerbrey's theory, mass sensitivity of the TSM device is directly proportional to its resonant frequency. Since the TSM resonant frequency is a function of its plate thickness, increasing the mass sensitivity meant that this plate thickness had to be reduced. Extremely thin crystals would be required which makes the device fragile and hard to support.

Surface acoustic wave (SAW) devices also obey Sauerbrey's relationship, but typically operate at higher frequencies (30 -300 MHz). In addition, they concentrate the acoustic energy near the sensing surface, thus offering the opportunity for higher mass sensitivities. SAW devices based on the generation of Rayleigh waves and can be used for vapor phase detection. A 250 MHz, quartz SAW resonator was developed to sense urine vapor flow [17]. While quartz is the traditional substrate of choice, AlN [18] and Lithium Tantalate [19] have been used as biosensors in the vapor phase. However, when sensing in liquids. Rayleigh waves excite compressional waves in the adjacent liquid due to their particle displacement normal to the sensing surface, which leads to considerable acoustic losses, which makes them unsuitable for liquid sensing applications. Lamb wave devices are known to give very high mass sensitivities [20, 21]. Lamb waves do not excite compressional waves in the liquid they are trying to sense, only if their phase velocity is low enough. They are therefore also preferred for bio-sensing in gaseous environments

It was the development of devices that were capable of operating in fluids that enabled the technique of gravimetric sensing to be introduced into bio-analytic applications in a big way. In order to build such a device, the waves applied are shear horizontal waves or guided shear horizontal waves (also called Love waves) [22]. A shear horizontal (SH) wave generates particle motion in the plane of the device and therefore does not introduce any compressional stresses in the liquid under stress. A guided SH wave device introduces a guiding layer within which the acoustic energy of the acoustic waves (Love waves) is concentrated and thus increases the mass sensitivity of the SH system. The property of Love waves for applications in sensors was discussed in detail by Jakoby and Vellekop [23]. Gizeli dealt with the design considerations of Love-wave devices when applied specifically to biosensing applications [24]. The use of different substrates and guiding over layers in Love mode devices, to maximize mass sensitivities is an area of active research.

Quartz and $LiTaO_3$ have been the traditional choices for the substrate in Love wave devices. Gizeli used silica as the guiding layer on ST-quartz, to detect the binding of the atrazine protein [24]. The device generated a maximum mass sensitivity of 430 g/cm^2 in air. Harding and Wu introduced a polymer layer as a guiding layer for the first time and used a hybrid PMMA film/SiO_2/quartz device to generate higher mass sensitivities [25]. However, PMMA shows high acoustic losses as well as poor chemical and temperature resistance [26]. But the SH-SAW mode on quartz suffers from low electromechanical coupling coefficients, high penetration depth, and low dielectric permittivity with respect to the liquid media**.** Love mode wave biosensors on $LiTaO_3$ substrates using cross-linked polymer waveguides were developed and used to detect

goat immunoglobulin with a mass sensitivity of 1420Hz/(ng/mm^2)[27]. A $LiTaO_3$ substrate based Love mode device was also used in the detection of pathogenic spores in aqueous conditions [28], where the detection limit was as low as, at 1-2 ng/cm^2. However, the shear SAW mode of $LiTaO_3$ suffers from the attenuation of the acoustic wave due to the excitation of the bulk acoustic wave (BAW) mode into the bulk of the crystal**.**

In this thesis, we target the development of a smart-card biosensor for real-time cost-effective accurate detection of airborne pathogens, and liquid (human serum) environments, on Si substrates as it offers the advantage of integration with the well-established CMOS technology.

1.2 ZnO Thin Film Gravimetric Sensors

ZnO is known to have a highly reactive surface due to a high concentration of unsaturated bonds on its surface and our research targets the investigation of ZnO for efficient protein binding. Since ZnO is highly piezoelectric and has a large electromechanical coupling coefficient, it is a suitable material for SAW operation. While ZnO based SAW delay lines and resonators have been widely used in RF communication devices [29-31], it is only recently that interest has been generated in its application as a biosensor. In this thesis, we investigate the development of a ZnO guiding layer based Love mode device on SiO_2/Si substrates for the detection of proteins. This section discusses the material properties of ZnO and its use in SAW device based gravimetric sensing applications.

1.2.1 Material Properties of ZnO

In the past decade, considerable attention has been paid to ZnO as a wide-gap oxide semiconductor. It has important pressure sensing [32,33] and optoelectronic (UV) properties [34,35], suitable for applications in transducers, sensors and UV light emitting/detecting technology [36].

ZnO is a tetrahedrally coordinated wide band gap semiconductor that crystallizes in the wurtzite crystal structure with lattice constants given by: $a = b = 3.249\,\text{Å}$ and $c = 5.206\,\text{Å}$. The lack of symmetry, combined with large electromechanical coupling coefficient, result in strong piezoelectric properties and the consequent use of ZnO in mechanical actuators and piezoelectric sensors.

Energy band gap (RT)	~3.3 eV
Thermal coefficient of expansion	6.51×10^{-6} /K
Thermal conductivity	0.6 mW/cmK
Excitonic energy[37]	60 meV
Electron density [38,39,40]	5×10^{14} cm^{-3}
Piezoelectric coefficient (e_{31}) [41]	0.43 C/m^2
Electromechanical coupling coefficient[42] On Sapphire substrates On Diamond substrates	 5 % 1.2 %

Table 1.1: Material properties of ZnO

1.2.2 ZnO Gravimetric Sensors

ZnO SAW devices have been used as gravimetric gas sensors. ZnO/Si based Rayleigh wave SAW delay lines were used to detect gases such as CO and H_2 [43], NO_2 [44] and O_2 [45]. Love wave devices with ZnO as the guiding layer on different substrates have been developed. The gas sensing behavior of layered SAW structures such as ZnO/$LiNbO_3$ [46] and ZnO/$LiTaO_3$ [47] was studied and their mass sensitivities determined. ZnO/$LiNbO_3$ structure is also being used for the development of Love wave biosensors in the liquid environment [48].

The most popular structure with ZnO as the guiding layer has been on ST-quartz substrates. ZnO on ST-quartz substrates were designed to sense Immunoglobulin g (IgG) with a mass sensitivity of 800 cm^2/g [49]. Sensor sensitivity in the ZnO/ST-quartz system was found to increase in air with by doping the ZnO film with Ca or Sr [50,51]. It was also found that the high sensitivity of the Love wave sensor was due to increased roughness of the ZnO film surface, when doped.

A Love mode sensor with ZnO as the guiding layer on SiO_2/Si substrates is developed in this thesis for the first time [52].

1.3. Interleukin-6

Cytokines are a group of proteinaceous signaling compounds that are used extensively for inter-cell communication. Interleukin-6 (IL-6) is a pro-inflammatory cytokine used to stimulate immune response to trauma, especially burns or other tissue damage leading to inflammation. Under normal conditions IL-6 is present in trace concentrations in the blood, and it increases under conditions of stress and certain illnesses. Hence, accurate, real-time, detection of IL-6 can be a critical indicator of such

conditions and provide a vehicle to understanding the processes of immune system response.

Overproduction of IL-6 is associated with a spectrum of age-related conditions including cardiovascular disease, osteoporosis, arthritis, type 2 diabetes, certain cancers, periodontal disease, frailty, and functional decline [53]. IL-6 is also one of the most important mediators of fever and of the acute phase response (i.e. in response to certain disease states). IL-6 stimulates the acute-phase reaction, which enhances the innate immune system and protects against tissue damage [54]. It results in the release of certain proteins, called acute-phase proteins, into the blood plasma by liver cells. IL-6 can also be secreted in response to specific pathogen associated molecular patterns (PAMPs). These PAMPs bind to highly important detection molecules of the human immune system, that are present on the cell surface and which induce intracellular signaling cascades that give rise to inflammatory cytokine production. IL-6 is produced in the muscle tissue, and is elevated in response to muscle contraction [55]. In the muscle and fatty tissue, IL-6 stimulation leads to increased body temperature.

Hence, effective detection of IL-6 provides an opportunity to develop a better understanding of these conditions, and allows for continuous detection with real-time patient evaluation, thus making it our protein of choice for the biosensor development.

1.4 Contributions

The specific contributions of this dissertation are as follows:

- **High quality thin film growth of ZnO on SiO_2/(100)p-Si substrates:** The growth of high quality ZnO on SiO_2/Si substrates was a challenging task. Through the development of pulsed laser deposition (PLD) growth, high quality (c-axis oriented, minimal strain,

narrow FWHM x-ray diffraction) ZnO thin films on SiO_2/Si substrates was achieved and the grown films lead to the development of high quality surface acoustic wave devices. The SiO_2 layer thickness was optimized experimentally for the first time to achieve optimum and consistent SAW operation. Achieving the growth on Si substrates provides the advantage of monolithically integrating it with CMOS peripheral circuitry.

- **Protein immobilization and morphological evaluation of the proteins on ZnO thin films:** We have developed the technique for covalent binding of IL-6 onto ZnO for the first time and achieve stable, controllable and specific binding. The morphology of the bound proteins was studied at each step for the first time, and a modified solid-phase ELISA technique was developed to bio-chemically determine the protein mass bound onto the ZnO surface.

- **Developed high frequency guided Love mode surface acoustic wave resonators with enhanced mass sensitivity:** SAW resonators operating at frequencies as high as 1.5 GHz were fabricated and characterized. The acoustic wave propagation in the films was shown to be guided shear mode waves or Love mode waves. The study of the effect of SiO_2 thickness on SAW performance was carried out. The dispersion relationship was theoretically and experimentally evaluated and the mass sensitivity was maximized.

- **Integration of protein immobilization on the SAW devices:** A technique to immobilize the protein directly onto the SAW resonators was developed and a prototype of the biosensor was fabricated. Changes in the resonant frequency of the resonator reflect the mass of the protein applied.

- **IL-6 in human serum was successfully measured**: The presence of proteins in normal human serum from donors both under and over the age of fifty was successfully detected.

1.5 Organization of this Dissertation

This chapter has given an introduction to the goals of this research. The current trends in the development of guided shear horizontal SAW devices for gravimetric biosensors have been discussed. The material properties of ZnO have been highlighted and the advantages of a ZnO based SAW device for biosensing has been outlined.

Chapter 2 discusses the growth conditions for ZnO thin films using pulsed laser deposition on Si and SiO_2/Si substrates. The purity of the grown films is studied through x-ray photoelectron spectroscopy and they are structurally characterized using room-temperature photoluminescence and x-ray diffraction (XRD). The effect of the thickness of SiO_2 layer on the ZnO film is determined through the XRD studies. Hall effect measurements are used to study the doping characteristics of the film.

Chapter 3 studies the morphological and binding properties of IL-6 to ZnO using scanning electron microscopy (SEM) and atomic force microscopy (AFM) . The binding of the IL-6 is carried out through a five step process through Bovine serum albumin (BSA). We have developed a modified solid-phase ELISA technique (Enzyme linked Immunosorbent Assay) for quantitative evaluation of the bound protein. A comparison between the amount of IL-6 bound onto SiO_2 and ZnO is carried out.

Chapter 4 focuses on the design and fabrication of a ZnO/SiO_2/Si surface acoustic wave devices. GHz frequency surface acoustic wave devices have been developed and the effect of SiO_2 thickness on SAW propagation is studied. The experimental

verification of the dispersion relationship of the SAW waves is carried out, which shows that ZnO when combined with a SiO_2/Si substrate can be an excellent material of choice for Love mode propagation.

In chapter 5, the theoretical framework for the mass sensitivity of the Love mode devices is discussed. The mass sensitivity of the ZnO/SiO_2/Si based Love mode device is numerically evaluated. The fabrication of a mass sensor, based on this system is detailed and the mass sensitivities are experimentally evaluated for a known copolymer mass, to calibrate the sensor.

In chapter 6, the technique of immobilizing IL-6 directly onto the ZnO/SiO_2/Si Love mode SAW sensor is discussed. The specificity of the IL-6 binding is ensured through the IL-6 antibody. SEM and AFM studies are carried out to study the morphology of the bound proteins. The chapter discusses the frequency measurements performed upon application of IL-6 to determine its mass. In order to develop a prototype of the biosensor, the presence of IL-6 in human serum is detected.

Chapter 7 summarizes the results of this thesis and presents some future avenues of work.

CHAPTER 2：PULSED LASER DEPOSITION OF ZnO THIN FILMS

2.1 Advantage of the Pulsed Laser Deposition Technique over other thin film deposition techniques

A number of thin film deposition techniques are currently used to grow ZnO thin films for research and in the industry. Selection of the deposition technique depends on the material to be grown and the application it is required for. The most important criteria in thin film growth is the ability to grow highly epitaxial films with minimal defects. Other important criteria include thickness uniformity, deposition rate, economy and stoichiometric congruence. Some of the thin film deposition techniques include molecular beam epitaxy (MBE) [56,67], metal organic chemical vapor deposition (MOCVD) [58-60], DC/RF plasma sputtering [61,62] and pulsed laser deposition [63-67]. Non vacuum methods such as sol-gel methods [68-70] are used for larger scale growth.

MBE is a sophisticated and costly film deposition technique developed primarily to grow quantum-wells and super lattices because to its capability of sub-monolayer thickness control. For ceramic oxides such as ZnO with a relatively low melting point of 2242 K [71], such thermal deposition techniques impose restrictions. Owing to their high throughput, CVD and MOCVD techniques are the most popular thin film deposition techniques in the industry. However, it would involve the preparation of a Zn precursor and also has problems with stoichiometry consistency. Low temperature depositions are generally not possible since a threshold temperature is required to initiate the chemical reactions. DC or RF sputtering is typically performed under high working-gas pressures

(10^{-2} torr) and non-selective erosion of both target material and target holder may contaminate the films. Sol gel techniques, while widely used for large scale growth typically generate a larger defect density along with having a low throughput.

PLD has proven to be a good technique for the growth of highly epitaxial ZnO thin films on a variety of substrates [17, 72-74]. The major advantage of PLD over other techniques is its inherent non-thermal equilibrium nature. This makes it possible to remove a small portion of the target, without disturbing the rest. The ablation process creates an effective temperature of 10^3~10^4 K in the ablated region, while the rest of the substrate is at room temperature. In addition, high kinetic energies (10^0~10^2 eV) [75] and resulting high surface mobility of impinging particles enables film re-crystallization at lower substrate temperatures and thus promotes minimal diffusion in multi-layer films with sharp interfaces.

The biggest disadvantages of the PLD growth technique is the small thickness uniformity and pressure dependant generation of macroscopic particulates. However state of the art PLD techniques [76,77] use techniques such as off-axis geometry, multi-beam ablation and femto-second laser pulses to effectively overcome these problems. In ultra short laser pulse systems, the ablation threshold is lowered and helps eliminates the thermal process that generates particulates. As a result, the transfer of bulk materials into thin films becomes more congruent.

A comparison of various thin film growth techniques has been summarized by Wei Yang [78] and is reproduced below:

	MBE	CVD/MOCVD	Sputtering	Sol-Gel	PLD
Thermal Equilibrium	Yes	Yes	No	Yes	No
Kinetic Energy	Low	Low	High	Low	High
Stoichiometry	Poor		Fair	Good	Good
Energy (eV)	<0.1	<0.1	1-100	<0.1	1-100
Precursor	No	Yes	No	Yes	No
Throughput	Low	High	Moderate	High	Low
Crystalline Quality	High	High	High	Moderate	High
Contamination	Low	Low	Moderate	High	Low
Cost	High	Moderate	Low	Low	Moderate

Table 2.1: Comparison of Thin film growth techniques

2.2 Pulsed Laser Deposition System

Figure 2.1 represents the ZnO PLD system used in this dissertation. It consists of four sub-systems. Laser and optics, vacuum chamber, target holder and substrate heater and computer control interface.

A Krypton fluoride (KrF, λ=248 nm) excimer gas laser (Lambda Physik, LX200) is used to ablate the ZnO target. Through repetitive charge and discharge of a high power electronic circuits, Kr and F_2 gases mix inside the laser cavity to form Kr^+-F^- excimers. These are metastable molecules that can exist only for tens of nanoseconds. Compared with the repulsive ground state, the bound excimer state has a longer lifetime that provides the population inversion necessary for lasing. The de-excitation of the KrF excimer leads to energy release in the form of 248 nm photon emissions, which lasts ~25ns for each pulse [64]. Other lasers such as the xenon fluoride (XeF, λ=351 nm) or

argon fluoride (ArF, λ= 193 nm) may also be used in the laser system. The repetition rate of the PLD is same as the discharging frequency of the electrical circuit and varies between 1 to 20 Hz. Typically, we operate the laser at a frequency of 10Hz. The total energy in each laser pulse is adjustable and varies according to the applied voltage in the discharging circuits. We have varied this between 200-450mJ/pulse for our purpose.

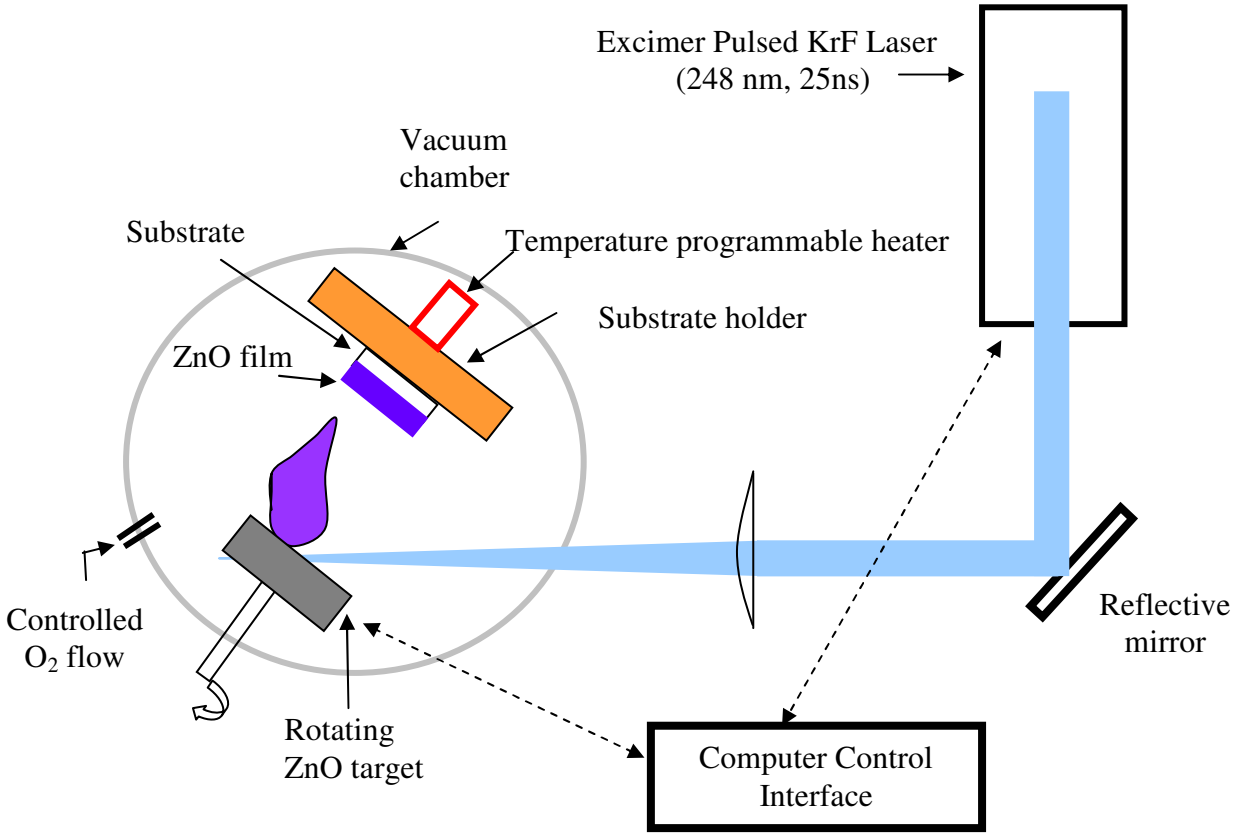

Figure 2.1: Schematic Diagram of a Pulsed Laser Deposition System

Through a simple optical collimation and focusing set up, the laser beam is incident on the sample at an angle of 45^0. The reflection mirror has a high reflection coating at 248 nm wavelength and the planar-convex lens used for focusing the beam onto the sample is designed to minimize UV absorption. The beam size is about 5x2 mm^2.

Material targets are mounted on a target carousel inside the vacuum chamber (maintained at ~ $1X10^{-7}$ torr). An inlet is provided for O_2 gas, which is pumped in to maintain the chamber at a specific working pressure during ablation. Multiple target holders are present on the carousel and the system provides the ability to switch between them. The target holder faces the substrate holder at a distance of 6.2 cm from it. The substrate holder can be heated upto 950^0C in a programmable mode. Upon increasing the substrate temperature, typically the chamber experiences out gassing and we wait for the pressure to stabilize within the chamber before beginning ablation.

A computer system is used to synchronize the switching of targets, dwell time on target as well as trigger the laser pulsing. The former is of more significance in multi-material or multi-layer deposition.

2.3 Growth Mechanism

Pulsed UV beam at high energy with a short wavelength in a low pressure of gas (usually oxygen) is incident on a target of the material to be deposited. The instant laser power density is as high as $5x10^8$ W/cm^2 [79]. Laser-material interactions involve coupling of optical energy into a solid, resulting in vaporization; ejection of atoms, ions, molecular species, and fragments; shock waves; plasma initiation and expansion; and a hybrid of these and other processes. The target surface temperature is instantaneously heated past its vaporization temperature through linear one-photon absorption, multi-photon absorption and dielectric breakdown. The vaporization temperature of the surface is exceeded within a fraction of the laser pulse duration and energy dissipation through vaporization from the surface is slow relative to the laser pulse width. Temperature and pressure of the underlying material are raised beyond their critical values, causing the

surface to explode. This process is referred to as ablation. The electric field strength for the KrF excimer laser on ZnO is 3.9x105 V/cm [77], which is well above the threshold of ZnO dielectric breakdown and results in removal of the target material before it can melt.

Plasma like plume of energetic material is visible between the target and the substrate and this could be attributed to the ionization of the materials by oxygen during flight. The spectral emission occurs as a result of the subsequent relaxation of the constituent excited species. This plume has been observed using various techniques like optical absorption and emission spectroscopy as well as fast photography and it is found that they consist of many elemental oxides. The shape of the plume is strongly affected by ambient gas pressure and at a working pressure of 10^{-4} torr, it takes a conical form [77].

Upon reaching the substrate, the ablated species stick onto the substrate as long as they don't escape back into the vacuum. Surface migration occurs to find dynamically stable sites and to construct randomly distributed particles into an epitaxial film [80]. The substrate is chosen for the best crystallographic, material properties and intended application. Our choice of substrate has been Si, so that the devices developed on the films can be easily integrated with established CMOS technology.

The primary parameters which govern film quality are: Laser power and wavelength, substrate temperature, deposition pressure and atmosphere, target/substrate distance and substrate properties. The laser ablation and material transport phenomenon is a complex process and the description provided above is simplified picture of the PLD. It remains an active research subject for investigation.

2.4 Thin film Characterization techniques

The thin films grown by PLD have been structurally characterized by X-ray photoelectron Spectroscopy and X-ray diffraction spectroscopy and optically characterized by photoluminescence spectroscopy. The charge density of the grown films was determined by Hall effect measurement. These techniques have been briefly described below.

2.4.1.1 X-ray Photoelectron Spectroscopy (XPS)

X-ray photoelectron spectroscopy (XPS) also known as electron spectroscopy for chemical analysis (ESCA) is a widely used technique to investigate the chemical composition of surfaces. The technique employs the determination of binding energy of the atomic elements composing the material. Soft x-rays (<1.5 keV) ionize atoms in a solid producing photoelectrons from core shells (the photoelectric effect).

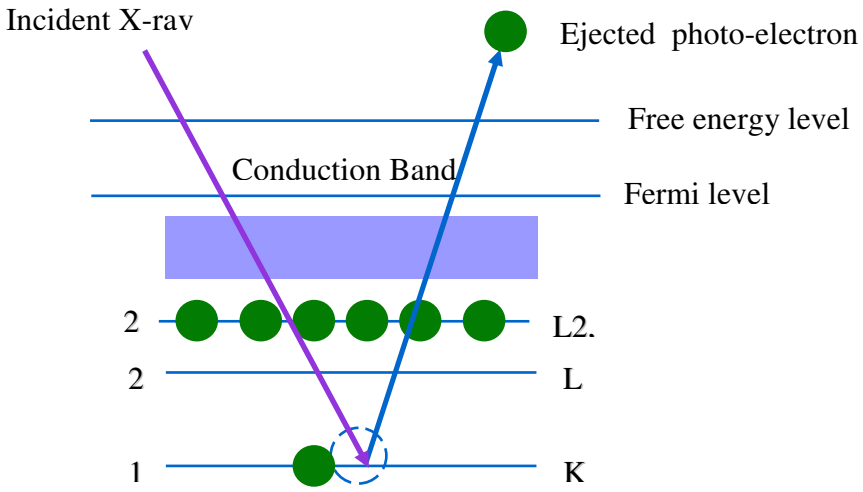

Figure 2.2: Schematic representation of the photoelectric process

As seen in Fig. 2.2, the incident x-ray ejects a core electron from a specific orbital and the XPS spectral lines are identified by the shell from which the electron was ejected (1s, 2s,

2p, etc.). The kinetic energy (K.E) of the emitted electron is equal to the x-ray energy minus the energy with which the electron is bound to the atom [81].

$$K.E = h\upsilon - B.E \tag{2.1}$$

where *B.E* is the binding energy of the photoelectron and *hv* is the energy of the incident x-ray. The low kinetic energy (by definition < 1.5 keV) makes the technique inherently surface sensitive with the majority of the photoelectrons in a given sample originating from the outer 10 nm of the film surface. The number of electrons detected is proportional to the concentration in the sample. Perhaps most importantly, the exact binding energy is a function of the local environment of the atom yielding a chemical state sensitive tool. Any shift in this binding energy due to change in the composition of the compound can be determined by the point charge model as follows [82]:

$$E_i = E_o + kq_i + \sum_{i,j} \frac{q_i}{r_{ij}} \tag{2.2}$$

where E_i is the binding energy of the electron in the reference state *i*, kq_i refers to the weighted charge of *i* and the final term refers to the potential at charge *i* due to surrounding charges. The area under peaks in the spectrum is a measure of the relative amount of each element present, and the shape and position of the peaks reflect the chemical state for each element.

2.4.2 X-ray Diffraction Spectroscopy

X-ray diffraction (XRD) is one of the most powerful tools that help reveal the crystal structure and crystalline perfection of thin films. Taking advantage of x-ray's short wavelengths, which is comparable with the lattice constants of single crystals, the

XRD technique detects the direction and intensity of diffracted x-ray beams, from which crystalline related information is derived.

The direction of the first order maximum diffraction is determined by the Bragg equation:

$$2d.\sin\theta = \lambda \tag{2.2}$$

where d is the inter-plane distance of the crystal lattice, θ is the refraction angle and λ is the wavelength of the x-ray (λ=1.54 Å and for a Cu-$K_{\alpha 1}$ target). The incident energy was 8.8 keV.

The intensity of the diffraction is described by [83, 84]:

$$I_{crys} = I_e.f(\vec{s}).L(\vec{s}) \tag{2.3}$$

where

$$I_e = I_0\left(\frac{e^2}{mc^2 r}\right)\frac{1+\cos 2\vartheta}{2} \tag{2.4}$$

is the intensity of non-polarized single electron x-ray scattering

$$F(\vec{s}) = \sum_i^n f_i \cdot e^{i2\pi\cdot\vec{s}\cdot\vec{r}_i} \tag{2.5}$$

is the structural factor of the crystal that counts the diffraction from each atom inside the unit cell and $L(\vec{s})$ is the Laue function counting for the N until cells in a sample volume on which the x-ray is incident.

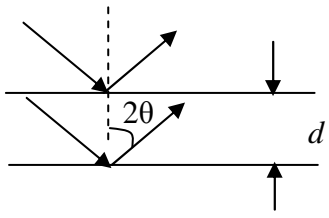

Figure 2.3: Schematic illustration of the θ-2θ scan

Fig. 2.3 schematically shows the θ-2θ scan, which gives an indication of the film orientation with respect to the substrate normal. Lattice constants and structural phases of the thin films can also be derived. The off-plane alignment of the film with respect to the substrate is judged by the line width of the ω-scan and the φ-scan verifies the film in-plane registry as well as the film's crystal structures.

2.4.3 Photoluminescence (PL) spectroscopy

PL spectroscopy is a contact-less, nondestructive method of probing the electronic structure of materials. A photon whose energy equals or exceeds the energy band gap can excite a valence electron across the energy gap. Absorption occurs when the photon raises an electron from a neutral donor to the conduction band or from the valence band to a neutral acceptor. It is also possible to induce absorptive transitions from the valence band to an ionized donor, or from an ionized acceptor to the conduction band. They also lead to the more sensitive probe of photoluminescence, which occurs when the excited electron returns to its initial state. If the return process is radiative, it emits a photon whose energy gives the difference between the excited and initial state energies. The emission spectrum shows a fingerprint peak related to the energy of each excited level.

The absorption process depends on whether the semiconductor has a direct or an indirect band gap. The energy is conserved during this process according to

$$\eta\nu = E_f - E_i, \qquad \text{for direct band gap transition} \qquad (2.6)$$

$$\eta\nu = E_f - E_i \pm \eta\omega, \quad \text{for indirect band gap transition}$$

where E_i and E_f are the initial and final state energies respectively and $\eta\nu$ is the photon energy. In indirect band gap transitions, the excited electron requires additional

momentum to reach the conduction band minimum that is at non-zero wave vector and it gains this energy from a phonon interaction [85].

An electron-hole pair can recombine non-radiatively [86] and the experimental study of these processes is then very difficult because the mechanism manifests itself only by the absence of a photon. Some non-radiative emission processes include phonon emission, surface recombination and Auger effect. In Auger effect, the energy released by a recombining electron is immediately absorbed by another electron, which then dissipates this energy by emitting photons. This is thus a three body collision process and one that depends on carrier-carrier interaction and becomes more intense as carrier concentration increases. Therefore as temperature increases, the carrier concentration (N_D) increases proportionately as $(-\left(E_g/kT\right)^{2/3} \exp\left(-E_g/kT\right)$ [32]. Thus at lower temperatures, the Auger effect reduces. Surface recombination refers to the presence of dangling bonds, which can absorb the recombining electrons. Also a cascade of phonon emissions could occur during recombination. At lower temperatures, lattice vibrations reduce significantly, thus lowering phonon emissions. Thus non-radiative recombination decreases at lower temperatures, increasing the efficiency of the PL measurements.

PL measurements at room temperatures can still be obtained, though with larger thermal broadening of the excited energy carriers. At room temperature, T the thermal broadening is roughly $k_B T$, where k_B is Boltzmann's constant. This gives rise to a broadening of 25meV at room temperature [87]. All our PL measurements were performed at room temperature.

2.4.4 Hall Effect Measurements

The basic physical principle underlying the Hall effect is the Lorentz force. When an electron moves along a direction perpendicular to an applied magnetic field, it experiences a force acting normal to the magnetic field and the current.

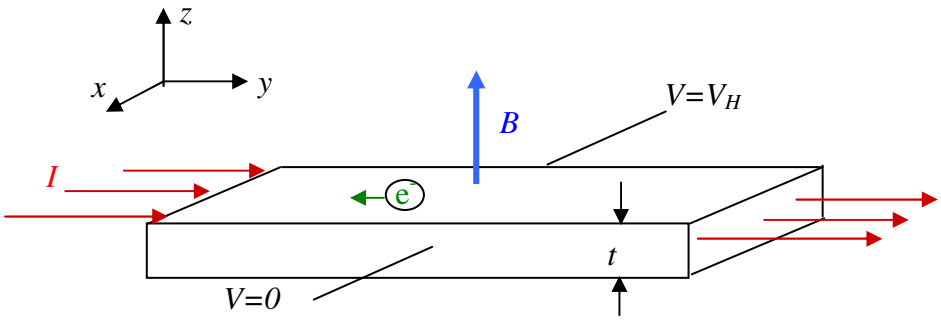

Figure 2.4: Schematic of the Hall effect in a long, thin bar of semiconductor with four ohmic contacts.

As shown in fig. 1, for an *n*-type, bar-shaped semiconductor, the carriers are predominately electrons of bulk density *n*. We assume that a constant current *I* flows along the x-axis from left to right in the presence of magnetic field along the z-axis. This force can be expressed as

$$F = q(\vec{E} + \vec{v} \mathrm{X} \vec{B}) \tag{2.7}$$

where, q is the charge, $\vec{E}$ is the electric field, $\vec{v}$ is the velocity, and $\vec{B}$ is the magnetic field. Note that the second term is transverse to velocity and to the magnetic field. Therefore, if sensing electrodes are placed across the transverse dimension of the plate, a voltage, called the Hall voltage, will appear. Ignoring scattering, and for an ideal plate geometry, the Hall voltage can be written in terms of the current as

$$V_H = \frac{IB}{qnt} = R_H \frac{IB}{t} \tag{2.8}$$

where I is the current, B is the magnitude of the magnetic field component transverse to the current, the carriers have charge q, n is the number density of charge carriers t is the thickness of the plate, and $R_H\left(=\frac{1}{qn}\right)$ is the Hall coefficient. We may also write an expression for the Hall voltage in terms of the impressed potential V (in volts) that drives the current,

$$V_H = \frac{\mu_H VBw}{l} \tag{2.9}$$

where is μ_H is the mobility of the carriers, and the plate has width w and length l. To a rough approximation, $R_H \sim \mu\rho$, where ρ is the resistivity of the plate. Thus the Hall mobility (μ_H) and net carrier concentration (n_H or p_H) values can be expressed as

$$\mu_H = \frac{R_H}{\rho} \qquad \text{and} \qquad n_H = \frac{1}{eR_H} \tag{2.10}$$

In the case of simultaneous existence of electrons and holes in the same region, the "two carrier" model [88] can be considered in order to describe the net Hall coefficient and mobility behaviour. According to this model the Hall coefficient is given by the following relationship:

$$R_H = \frac{p\mu_p^2 - n\mu_n^2}{e(p\mu_p + n\mu_n)^2} \tag{2.11}$$

where n, μ_n and p, μ_p are the carrier density and mobility in the n and p-type regions, respectively. From the above relationship, it follows that R_H can be negative (n-type) or positive (p-type) depending upon the value of $p\mu_p^2 - n\mu_n^2$.

2.5 Growth and Characterization of Thin ZnO films on p-type (100)Si Substrates

The growth of a metal oxide on the Si surface presents several challenges. Si is an elemental semiconductor and the growth of a binary system such as ZnO on its surface is difficult, due to the lack of two distinct attachment sites. In a substrate such as GaAs, which has two distinct sites for attachment, Zn^{2+} and O^{2-} are known to exhibit preferential site attachment. In the case of Si, it is likely that O^{2-} attaches itself first before the attachment of Zn^{2+}, but there has not been proven in literature. This attachment chemistry to some extent determines film quality in terms of strain, crystallinity, purity and intentional doping.

Although PLD has been proven to be a suitable technique to deposit high melting point ceramic materials, film qualities depend strongly on growth conditions, substrate type and quality, and complexity of PLD process [64]. Therefore optimization of PLD parameters is a necessary stop to obtain ZnO films with high degree of crystalline perfection. Key parameters include: deposition temperature, type of working gas and its pressure, laser parameters (wavelength, pulse duration, repetition rate, and energy fluence), target material and target conditions.

Some of the ZnO-related PLD optimization on sapphire substrates were addressed in early publications [17,89]. They obtained highly epitaxial ZnO thin films oriented along the c-axis when grown at 750 °C with a oxygen pressure of 10^{-5} Torr. The full-width at half maximum (FWHM) of the ZnO(0002) XRD peak was 0.17° indicating highly crystalline growth. The effect of energy fluence in thin film growth was studied in [77,90] and found a negative effect of higher energy fluence on ZnO film quality resulting in a rough film morphology. [77] also reported poor film quality at high oxygen

partial pressures (>10^{-2} torr) and optimal growth at $1.5x10^{-4}$ torr. C-axis oriented ZnO thin films have also been reported to grow on glass and polymer (both amorphous) under optimized PLD conditions (temperature between 400-500^{0}C and laser fluence of 1.8J/cm^2) [77,91].

Growth of ZnO thin films on (100)Si and (111)Si has been reported by the pulsed laser deposition (PLD) method [92-96]. XRD measurements indicate that the substrate temperatures of 200-500°C, and 200-500°C are the optimized conditions of crystalline for the (100)Si and (111)Si substrates, respectively [36]. On (111)Si substrates, XRD analysis indicated that the crystallinity of the films was improved with increase in temperature, while 250-500^{0}C temperature range shows equally intense diffraction peaks on (100)Si [92]. It has been reported however that the films grown on (100)Si reveal better structural, electrical and optical properties than on (111)Si due to the lower lattice mismatch between the (100)Si substrate and the ZnO film [93]**.** Our choice of substrate is therefore (100)Si.

Preliminary studies of the effect of oxygen partial pressure on ZnO film quality indicates completely c-axis oriented ZnO films on(100)Si at lower O_2 pressure regimes (1×10^{-4}-5×10^{-2} Torr). However a polycrystalline film with a much lower crystallinity and a rougher grained-surface was obtained at an O_2 pressure of $5x10^{-1}$ Torr [94,95]. This deterioration in film quality may be associated with the kinetics of atomic arrangements during deposition. However, detailed studies of ZnO films at pressures lower than $1x10^{-4}$ have not been reported.

We have investigated the influence of O_2 pressure as well as the growth temperature on the structural and electrical properties of undoped ZnO thin films grown

by Pulsed Laser Deposition (PLD) on p-type (100) Si substrates. When low O_2 pressures ($P<10^{-3}$ Torr) at low substrate temperatures (about 200 ^oC) are used, the PLD technique offers the possibility of controlling the conduction type and the electrical properties of high quality ZnO thin films. The base pressure in the vacuum chamber was at $2x10^{-7}$ Torr. The Si substrates have a resistivity of about 20 Ωcm. The laser fluencies were 0.8 and 1.8 J/cm^2. The ZnO films were grown under an O_2 partial pressure ranging from 10^{-3} to $8x10^{-7}$ Torr, and deposition temperatures between 150^{o}C and 450^{o}C.

2.6 Structural and Optical Characterization of ZnO/(100)Si films

A study was performed to determine the sticking coefficient of ZnO onto (100)Si substrates as a function of temperature, but with the oxygen partial pressure maintained at $1x10^{-4}$ torr. The ratio of the rate of adsorption to the rate at which the adsorptive strikes the total surface (0.5Å per pulse) is called sticking coefficient. It is usually a function of surface coverage, of temperature and of the details of the surface structure of the adsorbent. Because sticking coefficients are expected to increase toward unity at cryogenic temperatures, we anticipate that differences in the sticking coefficients of depositing species would be more prevalent at higher temperatures than at lower ones. However, since we are dealing with energetic species, these differences may still appear at room temperature. Fig 2.5 shows the measured sticking coefficient of ZnO on (100)Si. As expected, it is seen to reduce with increasing temperature and is above 0.8 at temperatures below 350^0C.

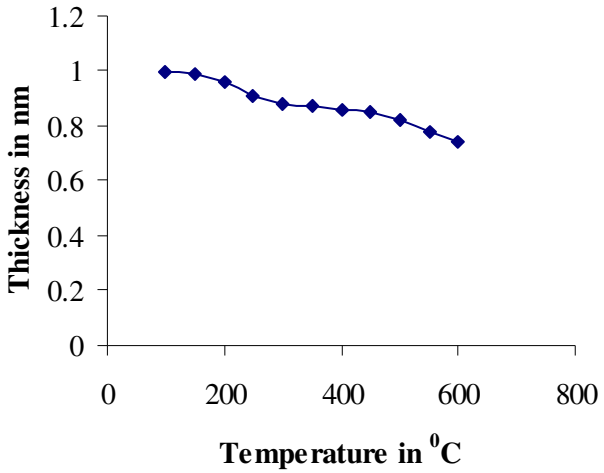

Figure 2.5: Sticking Coefficient of ZnO on (100)Si

Fig 2.6 shows the room temperature photoluminescence measurement of the ZnO/(100)Si sample (grown at 250^0C and with an oxygen partial pressure of $1x10^{-4}$ torr). This was performed in the Varian Eclipse PL system with a Xe lamp as the excitation source. The excitation wavelength set at 280nm by introducing appropriate filters. The PL peak is observed at 380.1 nm corresponding to intrinsic band to band emission of ZnO across an energy band-gap of 3.26 eV. The measured full width at half maximum (FWHM) is 20 nm (corresponding to 62 meV) at room temperature. The thermal broadening of the excited carriers at room temperature is thus visible as expected. Similar values of FWHM have been measured in previous studies when measured at room temperature [97].

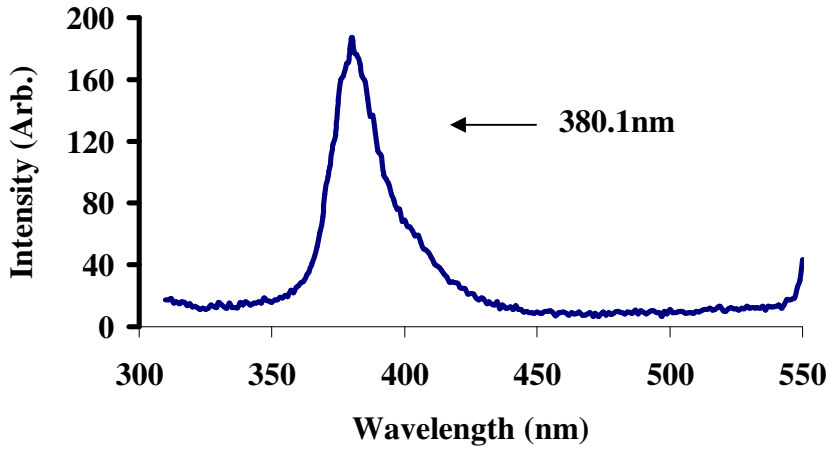

Figure 2.6: Room temperature PL spectrum of ZnO films grown on (100)Si substrates with an excitation wavelength of 280 nm.

With the excitation wavelength at 335nm, a broad spectrum, centered around 500 nm is visible indicating blue- green luminescence (Fig 2.7). Many researchers have attributed this to different intrinsic defects such as oxygen vacancies and zinc interstitials [98-100]. The ZnO peak at 380.1 nm is also visible with a FWHM of 20 nm, as in Fig 2.7.

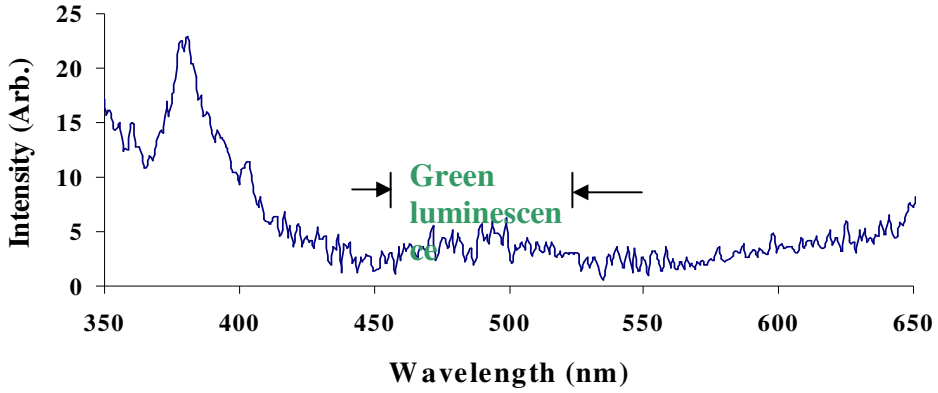

Figure 2.7: Room temperature PL spectrum of ZnO films grown on (100)Si substrates with an excitation wavelength of 335 nm.

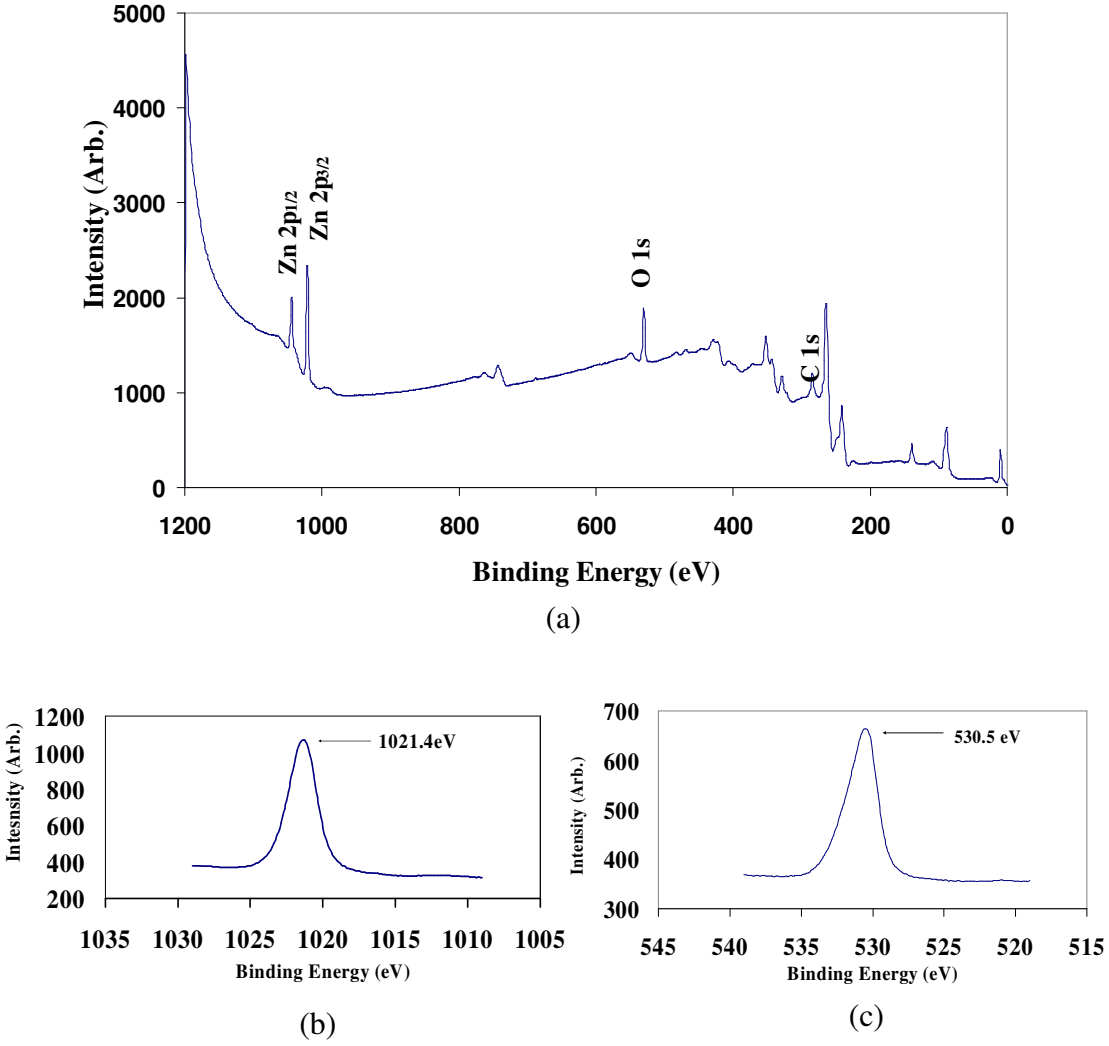

Figure 2.8: XPS spectrum of ZnO grown on (100) Si (a) low resolution spectrum (b) high resolution spectrum of the Zn($2p_{3/2}$) peak (c) high resolution spectrum of the O(1s) high resolution spectrum.

In order to determine the composition of the films, XPS analysis was performed. The films were grown at 250^0C at an oxygen partial pressure of $1x10^{-4}$ torr. The low resolution spectrum is seen in Fig 2.8(a). Distinct peaks are seen representing the Zn($2p_{1/2}$), Zn($2p_{3/2}$) and O(1s) orbitals. The high resolution spectra in Fig 2.8(b) and (c)

show that the binding energies of Zn($2p_{3/2}$) is 1021.4 eV and that of O(1s) is 530.5 eV corresponding to the energies in ZnO. This indicates that the ZnO grown is impurity-free.

The crystalline structure of the grown ZnO thin films was evaluated by X-ray diffraction (XRD) using CuKa radiation[1]. Fig.2.9 shows the X-ray patterns of ZnO thin films grown on (100) Si substrates for deposition temperatures ranging from 150 to 450^{o}C at an O_2 partial pressure of $1x10^{-4}$ Torr and laser fluence of 1.8 J/cm^2. The polycrystalline hexagonal wurtzite structure is revealed, and dominant peak positioned at 34.4^{o} corresponding to the (002) direction is observed. When the substrate temperature increases, an enhancement of crystallinity is indicated by the increase of the (002) peak intensity and decrease of full-width at half maximum (FWHM) values. It could be explained by the increase in the diffusion of oxygen atoms on the substrate surface as well as the reduction of Zn vacancies caused by the increase of the substrate temperature. This process results in the reduction of defect densities and in the growth of highly crystalline films.

Fig. 2.10 shows the mean crystallite size D, extracted from the XRD study of the (002) peaks, in ZnO films grown at temperatures between 150 and 450^{o}C in O_2 partial pressure of $1x10^{-4}$ Torr. The grain size values were calculated using the Scherrer formula [64] and the full-width at half maximum (FWHM·$\Delta\Theta$) of the rocking curves. The crystalline size increases with increasing temperature from 9 to 30 nm to result in the higher crystallinity of the ZnO thin films at higher growth temperatures.

[1] *The following study was a collaborative effort with C Padnis, D Brilis and Dr Tsamakis at the University of Aegean, Greece..*

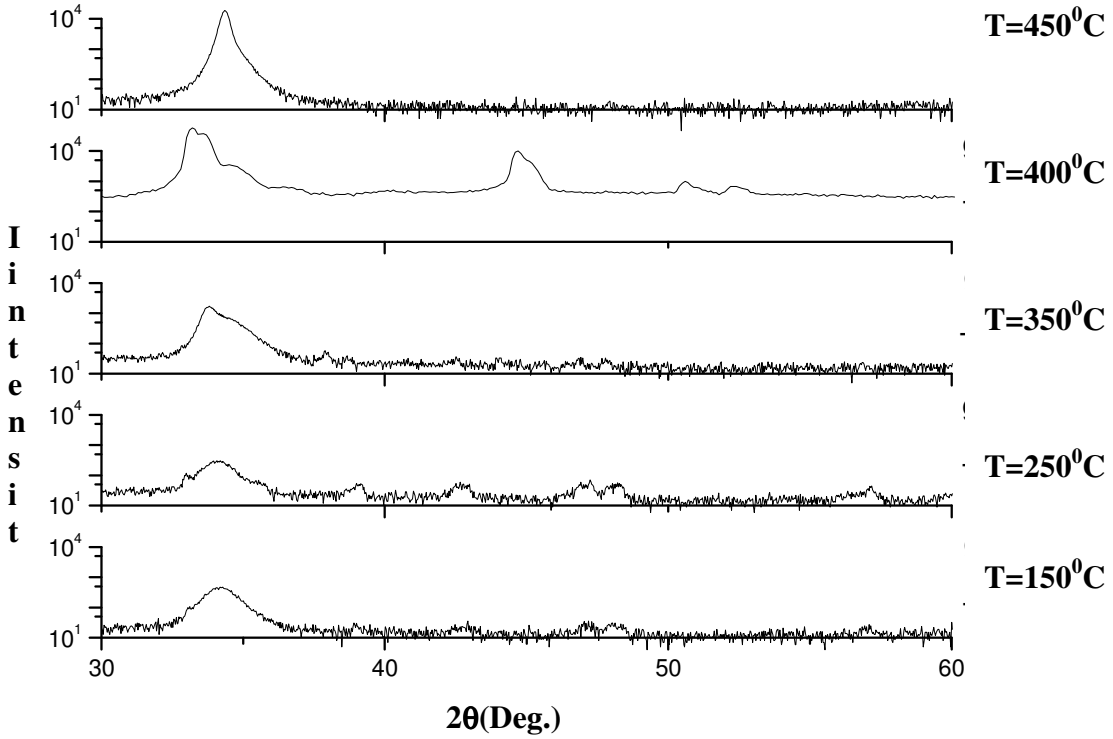

Figure 2.9: . θ -2θ scan of ZnO grown on (100) Si. The (0002) ZnO.peak at 34.4^0 is visible at all temperatures.

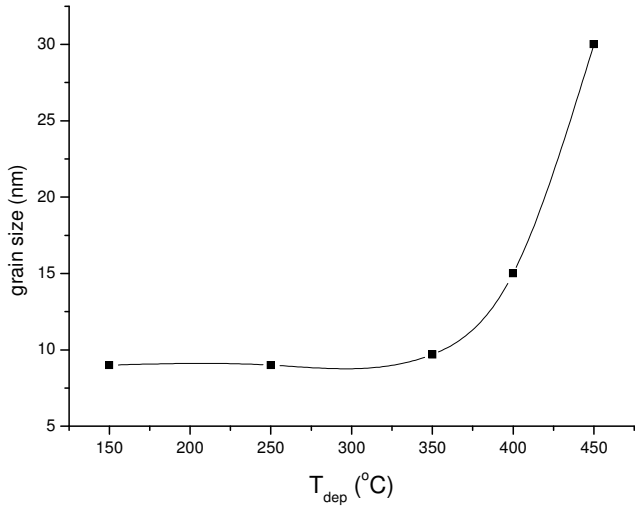

Figure 2.10: Grain size variation vs deposition temperature of ZnO thin films on Si substrates at O_2 partial pressure of 10^{-4} Torr and laser fluence of 1.8 J/cm^2

Previous studies of ZnO growth indicated that good crystalline growth on(100)Si was achieved at lower laser fluence of 0.7-1 J/cm^2[92,95]. The laser fluence for our experiments was then held at 0.8 J/cm^2. Since crystallinity of the ZnO thin films is also dependent on the O_2 partial pressure during growth, the following analysis was performed. Three ZnO thin films were grown under O_2 pressures of $1x10^{-4}$, $1.5x10^{-6}$ and $8x10^{-7}$ Torr, at the same growth temperature of 200^{o}C. If the temperature is increased beyond 200^{0}C, out-gassing causes a pressure increase within the vacuum chamber, making it very difficult to go to pressures lower than 10^{-5} torr. The observed preferential alignment at $2\theta=34.4^o$ (Fig 2.11) corresponds to the (002) direction. As the oxygen pressure increases, the intensity of the (002) peak decreases while the orientations (100) and (101) begin to appear. The crystalline quality of the films degrades as the average grain size increases from 3.5 to 9 nm with increasing pressure.

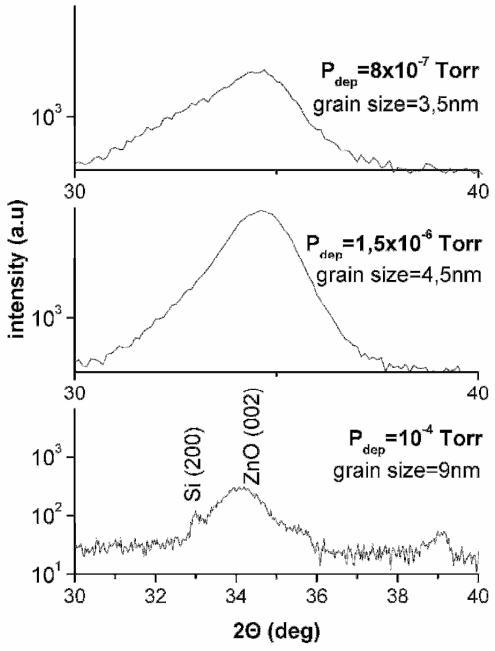

Figure 2.11: XRD patterns of undoped ZnO thin films deposited on Si substrates at three different O_2 partial pressure values at 200^{o}C and laser fluence of 0.8 J/cm^2

For the purpose of developing surface acoustic wave devices, the grain sizes obtained at moderate pressures and temperatures and lower energy fluences (250^0C, 10^{-4} torr and 0.7 J/cm^2) are acceptable [101]. These are the conditions of growth maintained for films used to develop all our surface acoustic wave devices. Fig 2.12 shows the θ -2θ scan of ZnO grown on (100)Si for these growth parameters. ZnO, being piezoelectric, generates an intrinsic electric field due to the strain introduced in addition to the applied field. This additional field might affect the frequency spectrum of the surface acoustic wave device in adverse ways. Hence, the strain introduced in the film ZnO films needs to be analyzed. The peak at 34.4^0 in Fig 2.12 indicates the (002) peak of ZnO. Thus the film has a predominant orientation of (002), though a second peak at (100) orientation is also visible. The film is epitaxial in nature with a predominant (002) orientation. The % strain introduced along the crystallographic axis was calculated as [102,103]

$$\%strain = \frac{c - c_0}{c} \tag{2.12}$$

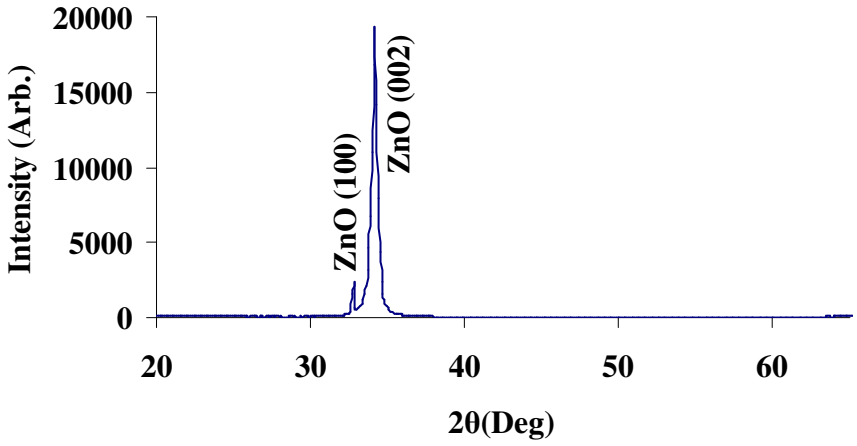

Figure 2.12: θ -2θ scan of ZnO grown on (100) Si. Peaks from left to right are (100) ZnO and (002) ZnO.

where c is the measured lattice parameter and c_0 is the bulk lattice constant. The % strain for ZnO grown on Si substrate was calculated to be 0.31% for a 300nm thick ZnO film.

The (002)ZnO peak in Fig 2.12 has a full width at half maximum of 0.4^0, which is considerably higher than the FWHM of 0.17 when ZnO is grown on sapphire [99]. This is because, when the wurtzite ZnO structure grows on the hexagonal sapphire substrate, it generates a lower inherent lattice mismatch than when ZnO grows on the cubic silicon substrate.

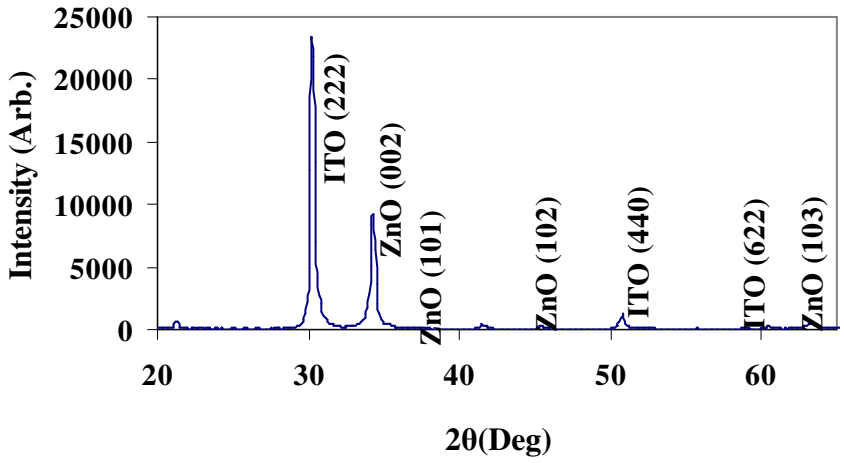

Figure 2.13: XRD 2θ scan of ZnO/ITO grown on (100) silicon by PLD.

The ZnO/ITO/sapphire system has been shown to be epitaxial with a full width at half maximum of 0.25^0[66]. A ZnO/ITO/(100)Si system was developed to determine if ITO in this case would improve the quality of the ZnO growth on Si. XRD on the ZnO/ITO/Si system indicated no change in the full widths at half maximum from a simple ZnO/Si sample, which remains at 0.4^0(Fig 2.13). The predominant orientation is still (002). However several orientations of ZnO are now clearly visible in the spectrum due to the strain introduced by the ITO layer. Thus the presence of the ITO layer does not aid in reducing the lattice mismatch between (100) Si and ZnO

2.7 Growth and Characterization of ZnO on SiO_2/Si substrates

A Love wave is an acoustic mode, which propagates in a layered structure consisting of a substrate and a guiding layer on top of it. It has a pure shear polarization and the particle movement is perpendicular to the saggital plane. A Love wave can only exist if the shear velocity in the guiding layer is smaller than the shear velocity in the substrate. In this case the layer slows down the acoustic shear mode in the substrate, thus decreasing the penetration depth and confining the acoustic energy to the surface. We will discuss this at greater length in chapter 4. In this thesis, we investigate a ZnO thin film grown on SiO_2/Si substrates for love mode propagation and therefore need to determine the crystalline quality of ZnO films on SiO_2/Si substrates.

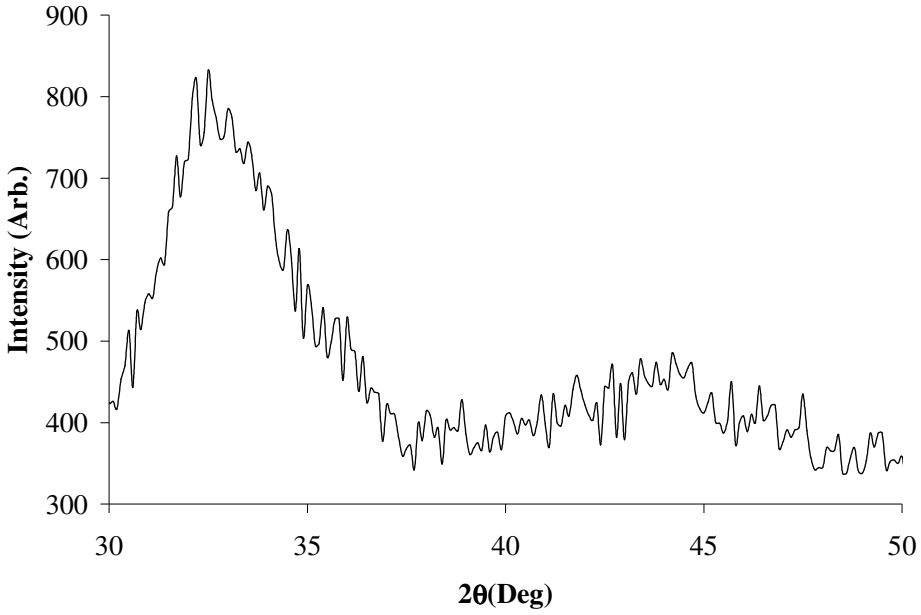

Figure 2.14: X-ray diffraction θ-2θ scan of a (100)Si substrate.

An XRD analysis was first performed on a (100) Si substrate and Fig. 2.14 shows the corresponding θ -2θ scan. The peak at 32.9^0 is assigned to the (200) Si peak.

Previous studies of ZnO growth on SiO_2/Si substrates by PLD have indicated that the grown ZnO film has a predominant c-axis orientation [104]. For our studies, a 2000^0A thick wet SiO_2 layer was a grown on (100)Si substrates by chemical vapor deposition. The ZnO thin films were grown on SiO_2/Si substrates at 250^0C, and an oxygen partial pressure of $1x10^{-4}$ torr. The laser fluence was maintained at $0.7J/cm^2$ with a repetition rate of 10Hz. The crystalline quality of the ZnO films grown on SiO_2/Si substrates was characterized with x-ray diffraction.

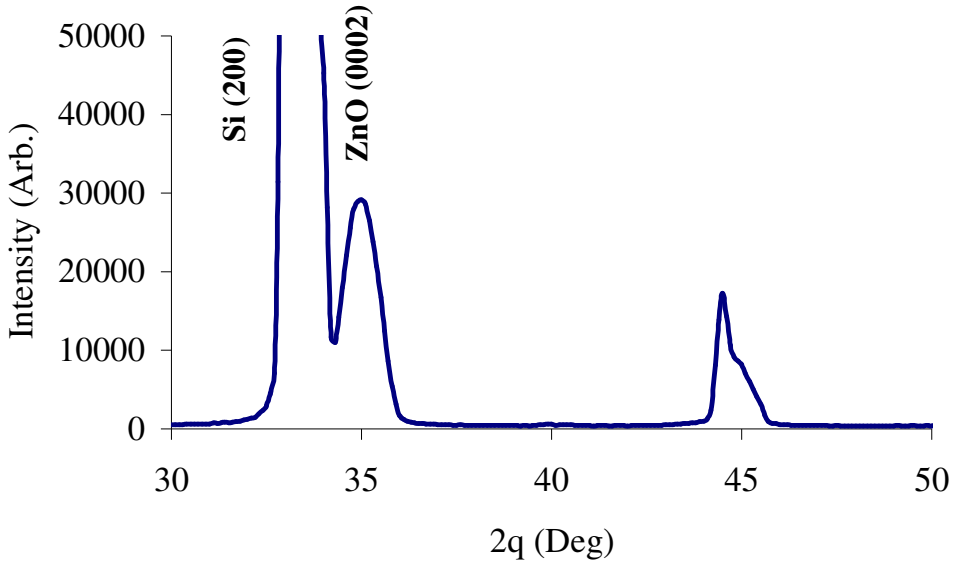

Figure 2.15: X-ray diffraction θ-2θ scan of (a) ZnO/SiO_2/(100)Si with SiO_2 thickness of 2000Å. The (0002) ZnO peak is at 35.2^0, indicating a highly strained film with a strain of 2.3%,

Fig. 2.15 shows the θ -2θ scan of a 1μm thick ZnO film grown on a 2000Å SiO_2 layer on (001)Si. The peak at 35.2^0 indicates a predominant orientation along (0002) with a full width at half maximum (FWHM) of 2^0. As seen previously, ZnO films grown directly on (100)Si by PLD generated predominant orientation of (0002) . This XRD study indicates that for the given thickness of SiO_2, the grown ZnO layer also maintains the same orientation as if grown directly on (100)Si, but introduces an additional strain in

the films. The measured strain of the ZnO film grown on 2000Å SiO_2 layer on (100)Si is as high as 2.3%. The peak at 32.9^0 is the (200)Si peak as seen in Fig. 2.14.

Annealing has been shown to improve film quality of ZnO on SiO_2 substrates [105]. XRD analysis was used to show that the strength of the (002) ZnO peak increases and FWHM value decreases as the annealing temperatures increases from 200 to 600°C. It was also found that the optical properties of ZnO thin films could be greatly improved by a post-growth annealing process [106].

The thin film strain is an important parameter in acoustic devices as it may introduce an electric field in addition to the applied field, thus affecting device frequency performance. This has been addressed in detail in Chapter 4. It is therefore important to determine substrates and growth parameters required to minimize this strain. However an analysis on the effect of strain reduction as a function of annealing temperature has not been reported in literature. For this analysis, the ZnO films were annealed in air at temperatures ranging between 450^0C and 750^0C for 45 minutes. The maximum reduction in strain was achieved at 500^0C with the (0002) ZnO peak at 35.1^0. This decrease in strain however, was only marginal, with the measured strain still being 2%.

One technique to decrease the strain is to reduce the thickness of the underlying amorphous SiO_2 layer. For our studies the SiO_2 layer thickness was reduced to 500^0A. The θ-2θ scan of the grown ZnO layer on the reduced SiO_2 thickness is shown in Fig 2.16. The (0002) ZnO peak is seen at 34.5^0, with the corresponding strain being reduced to 0.56%.

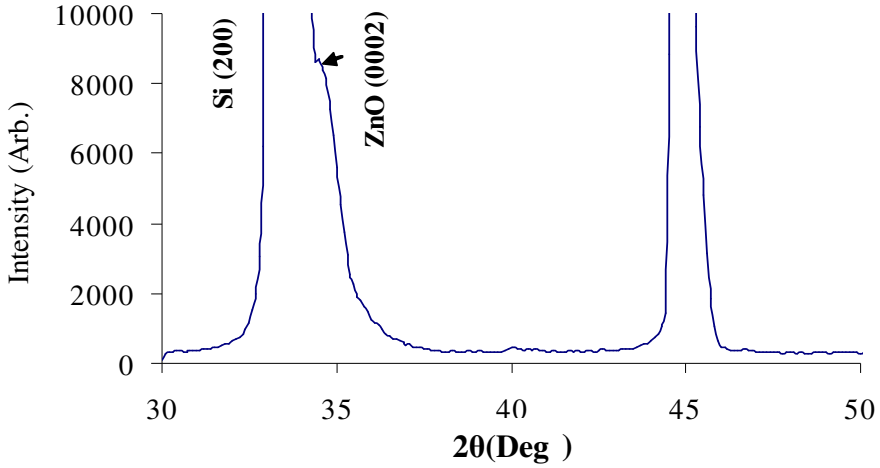

Figure 2.16: X-ray diffraction θ-2θ scan of (a) ZnO/SiO_2/(100)Si with SiO_2 thickness of 500Å. The (0002) ZnO peak is at 35.2^0, indicating a highly strained film with a strain of 0.56%.

2.8 Development of p-ZnO on (100)Si substrates

ZnO is also an attractive wide band semiconductor material for optoelectronic applications as short-wavelength LEDs [107-109], lasers [52-54,110], and UV detectors [111]. Such applications are a consequence of the direct energy band gap of ZnO films (~ 3.37eV at RT), and a high excitonic binding energy of 60 meV. However for the development of optical and electronic devices based on ZnO, the growth of both p- and n-type ZnO films of high quality is necessary. Several articles have reported on n-type doped or undoped ZnO films exhibiting n-type behavior due to the native donor defects [61]. Lately some authors have reported p-type undoped ZnO based on native shallow acceptor defects dependent on the growth parameters [57,113,114]. In this thesis we have investigated the conductivity type of the ZnO films grown on (100)Si by PLD.

2.7.1 Growth of p-ZnO films and Hall Effect measurements

The conductivity type of ZnO thin films was determined by Hall coefficient (R_H) measurements at room temperature[2]. The electrical resistivity of the samples was measured using the Van der Pauw technique, while the type of conductivity and the carrier concentration were obtained by Hall voltage (V_H) measurements at a magnetic field of 0.4 Tesla. Ohmic contacts for electrical measurements were made by using silver paint at the four corners of the square-shaped samples.

The carrier concentration (n_H or p_H) and the Hall mobility (μ_H) were obtained from equation (2.10). Fig.2.16 shows the Hall coefficient of ZnO/Si thin films, grown at temperatures between 150 and 450^{o}C at O_2 partial pressure range of $9.2x10^{-7}$ to $1x10^{-3}$ Torr. As shown in Fig. 2.16, the films grown in O_2 partial pressures between $8x10^{-7}$ and $1x10^{-4}$ torr exhibit p-type conduction. A general trend emerges from the R_H results, where the p-character of ZnO thin films is reduced with increasing O_2 partial pressure during the PLD growth process. The influence of the growth temperature on the conduction type of the ZnO thin films is also shown in Fig. 2.17. In particular, with a laser fluence of 1.8 J/cm^2, the Hall coefficient (R_H) decreases from positive to negative values when the substrate temperature increases from 150 to 450^{o}C. The change in conduction sign takes place at deposition temperatures around 350^{o}C. For films grown with laser fluencies of 0.8 J/cm^2, the change in conduction sign occurs between 200 and 250^{0}C.

[2] The following study was a collaborative effort with C Padnis, D Brilis and Dr Tsamakis at the University of Aegean, Greece.. The Hall measurements were performed at the University of the Aegean.

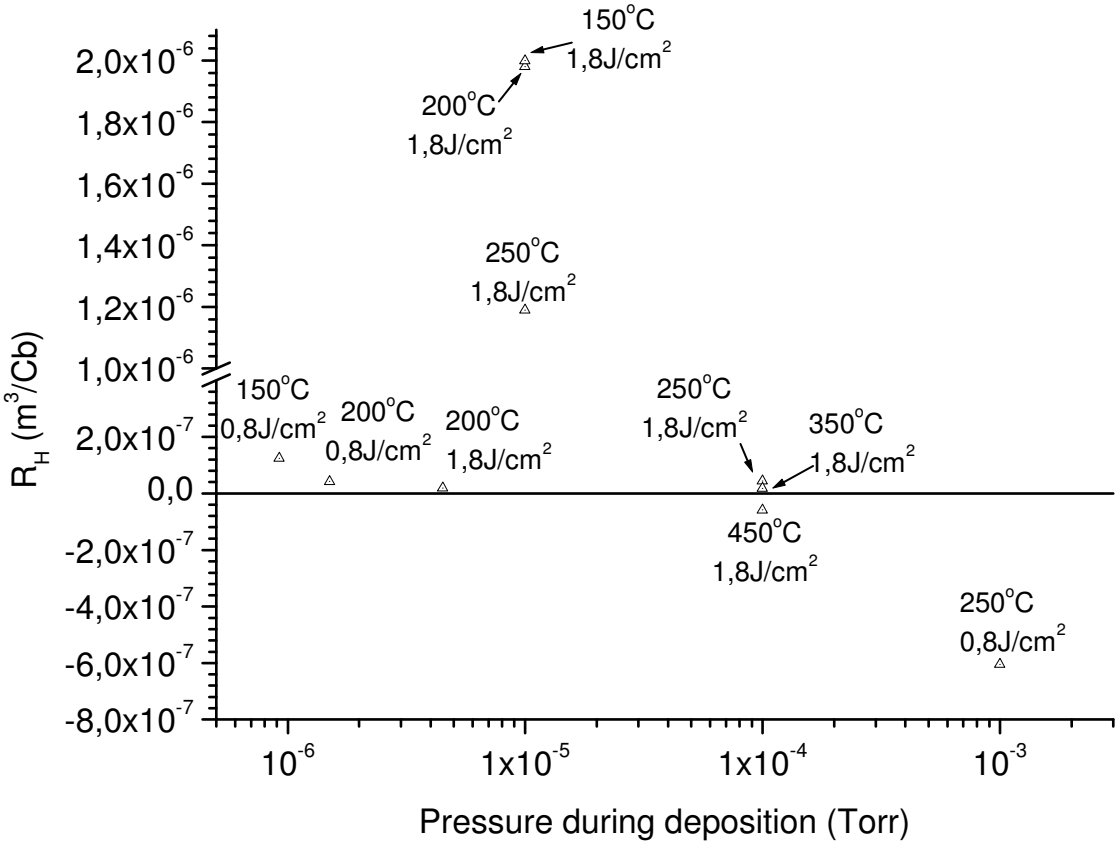

Figure 2.17: Hall coefficient vs. O_2 partial pressure in ZnO films grown at various temperatures and laser fluencies.

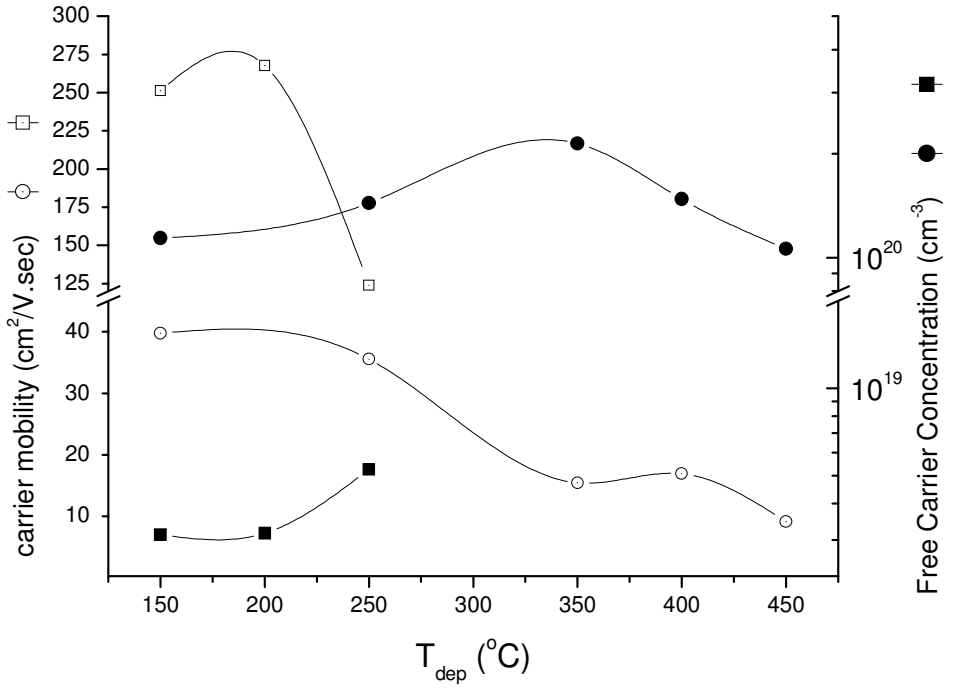

Figure 2.18: Free carrier mobility and concentration curves as related to deposition temperature for undoped ZnO thin films grown on Si substrates at laser fluence of 1.8 J/cm^2 and O_2 partial pressure of 10^{-4} (⊖ and ●) and 10^{-5} Torr (⊟ and ■) respectively

The carrier concentrations decrease, for growth temperatures higher than 350^{o}C due to the reduction of the acceptor states (Fig 2.18). Hall mobility in our case is limited by the ionized scattering centers as well as the grain boundary scattering. The increase of the grain size with lower carrier concentrations results in higher boundary barriers between the grains and thus in the reduction of the carrier mobility. For carrier concentrations of 10^{20} cm^{-3}, grain barriers are narrow enough so that the electrons are able to tunnel through the barriers. As such carrier scattering is no longer limited by the grain barriers but is determined by ionized impurity scattering. For samples grown at

lower temperatures (<350^{o}C) the high mobility values of polycrystalline thin films can be compared with the heavily doped single crystal results [115].

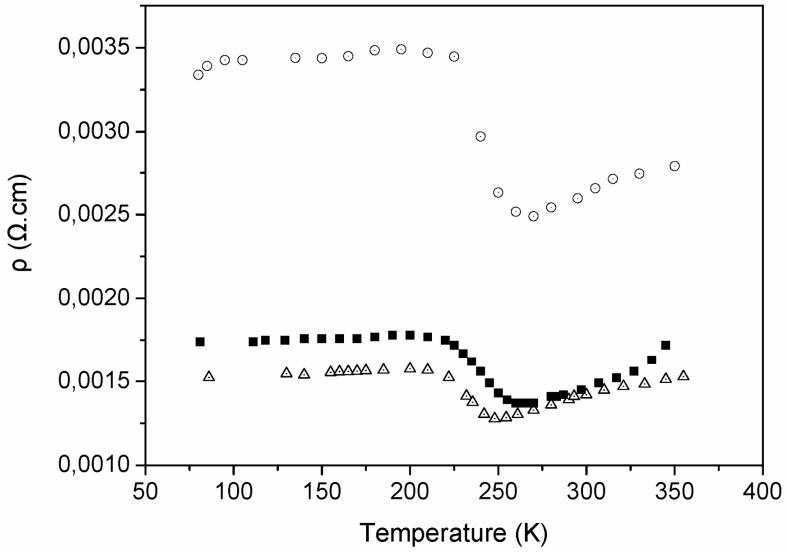

Figure 2.19: Electrical resistivity results vs temperature for three ZnO films grown in O_2 pressures: 8x10^{-7} Torr (○), 1.5x10^{-6} Torr (Δ) and 1x10^{-4} Torr (■).

It was also found that the electrical resistivity (ρ) and the Hall coefficient (R_H) measurements depend on the temperature at which the measurements are performed. Three films grown at 8x10^{-7} Torr, 1.5x10^{-6} Torr and 1x10^{-4} Torr with a laser fluence of 1.8 J/cm^2 and 200^{0}C were analyzed. The Hall measurement temperature was varied between 80 and 350K. ρ is almost a constant at temperatures between 80 and 225K (Fig. 2.19) At temperatures between 225 and 250K a fast reduction of about 30% is observed while for temperatures higher than 250K the resistivity increases again indicating a change in the conduction mechanisms.

As shown in Fig. 2.20, the Hall coefficient R_H exhibits negative values at temperatures between 80 and 225K in all three films, indicating n-type conduction.

However, the R_H values tend to change from negative to positive at temperatures above 232, 231 and 242K in films grown in O_2 pressure of $8x10^{-7}$, $1.5x10^{-6}$ and $1x10^{-4}$ Torr, respectively, thereby signifying conversion of the conduction character of the films from n to p-type. The p-type character of the films continues up to room temperature, remaining stable with time and exhibiting good reproducibility.

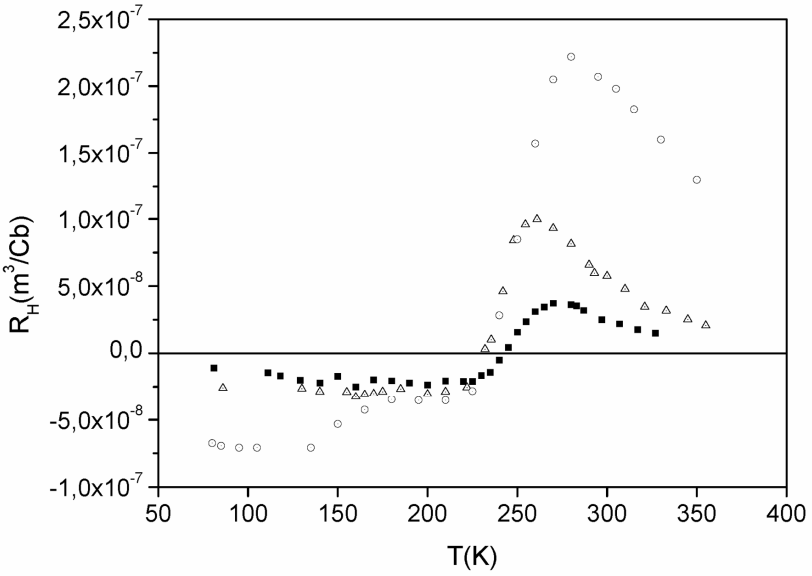

Figure 2.20:Hall coefficient vs temperature for ZnO films grown in O_2 pressures: $8x10^{-7}$ Torr (○), $1.5x10^{-6}$ Torr (Δ) and $1x10^{-4}$ Torr (■). The turning-points for R_H to switch sign are at 232, 231 and 242K, respectively.

2.7.2 Electrical Conduction Model

The R_H behaviour as seen in Fig. 2.20 reveals the existence of two at least native states contributing to the electrical conduction of the films in the entire temperature range of 80 to 350K of the measurement. This behaviour can be explained by assuming a competition between electrons coming from activated native donor states, and holes coming from native acceptor defects in the ZnO films. As seen in Fig. 2.21 the n-type character dominates over the p-type character at temperatures between 80 and 230K where the slow change of R_H indicates the existence of a shallow donor state completely ionized at the lower temperature regime. The transformation from n-type to p-type occurs between 230-270K. Between 270-350K, a process of thermal activation originating from deeper acceptor states to the valence band, results in the observed domination of p-type conduction.

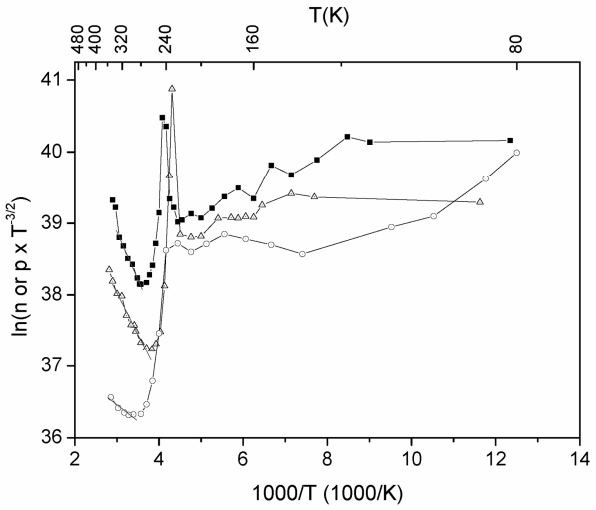

Figure 2.21: Temperature dependence of the carrier concentration (net values) plotted as $\ln(n \text{ or } p \cdot T^{-3/2})$ vs T^{-1} for ZnO films grown in O_2 partial pressures: $8x10^{-7}$ Torr (○), $1.5x10^{-6}$ Torr (Δ) and $1x10^{-4}$ Torr (■). The net values of the concentration (n or p) varied between $5x10^{20}$ and $1x10^{21}$ cm^{-3}.

The carrier densities (n or p) obtained from equation (2.11), are plotted as in Fig. 2.22. It can be seen that the results are fitted by straight lines only over the temperature range of 270 to 350K indicating a thermally activated behaviour in this temperature range. This behavior, as predicted above, arises from the carriers being excited from acceptor defect states to the valence band of the ZnO films. This is supported by the R_H results indicating p-type behavior for temperatures higher than the observed three temperature turning points (232, 231 and 242K) in Fig. 2.21.

It is also evident (Fig, 2.21) that a typical Arrhenius dependence in p(T) cannot be obtained at the low temperature range (80 – 270K) and hence, a different non-activated conduction mechanism needs to be considered. This has been previously described in detail in [116]. In particular, it was suggested that the electrical conductivity decreases slowly with temperature, in the range 80-220K, due to the existence of a hopping conduction mechanism. In this temperature range, variable range hopping conduction (VRH) mechanism occurs at in the localized states of the compensated acceptor band. When donors and acceptors coexist, as it is in our case, the conductivity values may be high even for concentrations of donors (N_d) and acceptors (N_a) lower than 10^{18} cm^{-3}. In this case the semiconductor is compensated and if $N_a > N_d$ then it assumes the p-type character. N_d ionized donors correspond to N_a-N_d unionized acceptors and the free holes would be transported by a hopping (tunneling) process from filled to vacant sites.

Over the temperature range of 220 to 270K, the Arrhenius plot of $\ln\sigma$ vs T^{-1} (Fig. 2.22), represents a hopping conduction, as first predicted by Mott [117], and called the nearest-neighbor hopping (NNH) conduction mechanism. Such hopping will produce very small or vanishing Hall coefficient values [118], in agreement with our results over

the temperature range where the transition from n to p-type is taking place. For temperatures lower than 80K, residual conductivity arising from the shallow donor states completely ionized dominates.

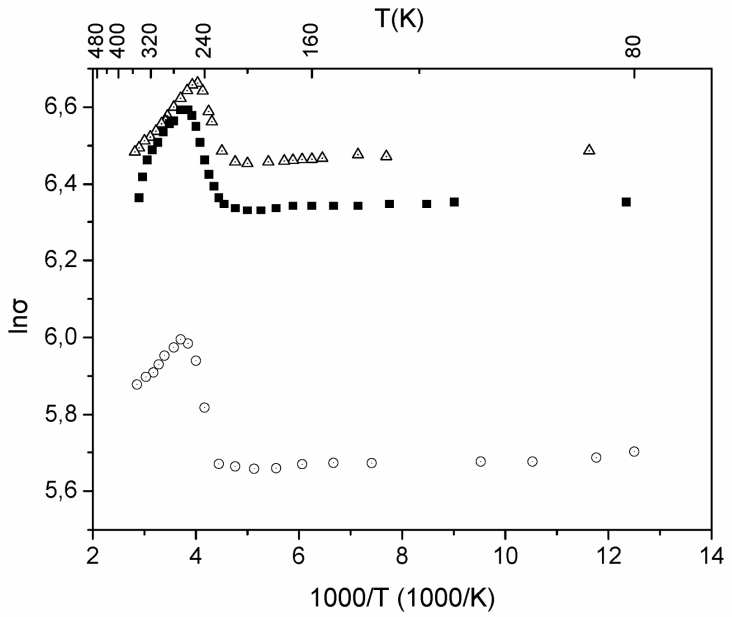

Figure 2.22:Temperature dependence of the electrical conductivity plotted as lnσ vs T^{-1} for ZnO films grown in O_2 pressures: $8x10^{-7}$ Torr (○), $1.5x10^{-6}$ Torr (Δ) and $1x10^{-4}$ Torr (■).

2.9 Summary

The growth of c-axis oriented ZnO thin films on (100) Si and SiO_2/Si substrates by pulsed laser deposition has been developed. The purity of the films was determined with XPS studies, and they were structurally characterized by XRD studies.

The effect of the growth temperature and pressure on crystallinity was studied. As the oxygen pressure increases, the intensity of the (002) peak decreases while the orientations (100) and (101) begin to appear. The crystalline quality of the films degrades as the average grain size increases with increasing pressure. Increasing the

temperature of the substrate upto 450^0C also increases crystallinity. This is because, as substrate temperature increases, there is an increase in the diffusion of oxygen atoms on the substrate surface as well as the reduction of Zn vacancies. For the purpose of developing surface acoustic wave devices, the grain sizes obtained at moderate pressures and temperatures and lower energy fluences (250^0C, 10^{-4} torr and 0.7 J/cm^2) were found acceptable.

The effect of the SiO_2 layer thickness on the strain produced in the grown ZnO film was studied. It was determined that reducing the thickness of the SiO_2 layer from 2000 Å to 500 Å reduced the strain introduced in the ZnO film significantly from 2.3% to 0.56%. Annealing the film lead to a marginal decrease in the strain produced.

The conductivity type of ZnO thin films was determined by Hall coefficient (R_H) measurements at room temperature. The electrical resistivity of the samples was measured using the Van der Pauw technique, while the type of conductivity and the carrier concentration were obtained by Hall voltage (V_H) measurements. It was found that the p-character of ZnO thin films is reduced with increasing O_2 partial pressure during the PLD growth process. Also the films start to become more n-type with increasing substrate temperatures - from 150 to 450^oC for a laser fluence of 1.8 J/cm^2. The free carrier mobility and concentration curves as related to deposition temperature for undoped ZnO thin films were developed.

The electrical resistivity of the film depends on the temperature at which the measurements are made and an electrical conduction model for the films for the temperature range between 80K and 350K has been developed.

CHAPTER 3 : DEVELOPMENT OF PROTEIN IMMOBILIZATION ON ZnO THIN FILMS

3.1 Protein functionalization techniques: Physical Adsorption Vs Covalent Binding

One of the critical points in the development of high quality biosensors in ZnO is the effective and controlled immobilization of the appropriate proteins onto the surface of the ZnO film. Traditionally, proteins have been physically adsorbed onto the inorganic material or substrate of interest [119-125]. The proteins are charged particles that functionalize themselves by electrostatic attraction onto the substrate surface.

The fundamental drawback with protein adsorption is that the attachment of the protein to the substrate is not specific or controllable. Application of ultrasonic shaking on the sample for example can rid the substrate almost entirely of the adsorbed protein. Thus any disturbance during the course of a real measurement on the field can drastically change the quantity of protein adsorbed. Also, in an uncontrolled environment, material other than the protein could get adsorbed onto the substrate. In order to avoid this, binding the protein covalently (and thus specifically) to the substrate surface becomes important. Covalent binding of a protein to an inorganic surface, when controllable, produces a strong interface, with an almost irreversible immobilization of the protein on the sensor surface [126]. Kodera et al [127] reported the detection of protein-protein interaction on SiO_2/Si surfaces, by spectroscopic ellipsometry, where the proteins were covalently bound onto the surface of a SiO_2/Si substrate. In our work, we have developed a immobilization technique to bind proteins (specifically Interleukin-6 or IL-6) onto ZnO thin films for the first time.

The covalent binding technique typically consists of a series of binding steps, each generating a self-assembled monolayer (SAM) [128]. The first step in this sequence is critical as it is the bridge between an inorganic substrate and the organic protein. The cross-linker used in this first step can be of various types depending on the substrate. e.g. organosilicon on hydroxylated surfaces, alkanethiols, dialkyl sulphides and di-sulphides on gold and other noble metals, and carboxylic acids on aluminum oxide.

Au has been widely used as the electrode of choice in quartz crystal microbalance and cantilever systems, where dithiobis succinimidyl propionate (DSP) and a dextran modified thiol monolayer were used as the binding material in the first step[129,130] Quartz, a piezoelectric crystal with an inert surface, was effectively for the immobilization of proteins for biodetection, where the hydroxlyated surface of quartz was prepared with silanes [131]. We have used a 3 – amino propyl triethoxy silane (or ATES) as the cross linker to the ZnO film as described in section 3.3.

3.2 Choice of Substrate and Antigen

Inorganic crystalline materials important to sensor development are those with specific properties, such as piezoelectricity, that allow the development of transducers to measure shift in frequency of operation due to the added mass on their surface. (e.g. bulk acoustic wave devices (BAW) or surface acoustic wave devices (SAW)). Zinc oxide (ZnO), is a material system with a high piezoelectric coefficient (0.43 C/cm^2), and has a highly reactive surface. The higher piezoelectricity can enhance the sensitivity of the system, and the reactive ZnO surface offers the opportunity for effective bio-ZnO interfaces.

ZnO bulk acoustic wave (BAW) resonators with high resonance frequencies (2GHz) for sensor applications have been reported [132]. The development of sensors directly on Si substrates provides the opportunity for full integration with read-out and signal processing circuitry in the mature Si technology [133]. This can be extended to multifunctional arrays, for rapid, real-time sensing and analysis at substantially reduced cost. Protein expression profiling chips with distinct spots of immobilized protein capture agents, will allow the simultaneous measurement of hundreds or thousands of proteins from one sample [134]. This work details the use of ZnO films for developing surface acoustic wave based biosensors on Si substrates.

Overproduction of IL-6 is associated with a spectrum of age-related conditions including cardiovascular disease, osteoporosis, arthritis, type 2 diabetes, certain cancers, periodontal disease, frailty, and functional decline [135]. Vgontzas et al [136] also showed that sleep deprivation leads to sleepiness and daytime hyper secretion of IL-6. Hence, effective detection of IL-6 provides an opportunity to develop a better understanding of these conditions, and allows for continuous detection with real-time patient evaluation, thus making it our protein of choice for the immobilization studies.

As discussed in chapter 1, the gravimetric detection principle offers the advantage of being label-free. The surface of the sensor is coated with an antibody to which the antigen of interest is adsorbed. The formation of this complex on the sensor results in changes in its resonance frequency due to the added mass, which can be easily determined. In order to build such sensors on ZnO, it is critical that the attachment mechanism of the protein onto the ZnO surface, and the interaction between the surface and the biomaterials, be explored. In the present work, we have employed a procedure of

protein immobilization onto ZnO and SiO_2 films grown on (100) Si, with the SiO_2 films serving as reference. We have studied the morphological and binding properties of the proteins at each stage, using scanning electron microscopy (SEM) [137], atomic force microscopy (AFM) [138], and have developed a modified solid-phase ELISA technique (Enzyme linked Immuno sorbent Assay) for quantitative evaluation.

3.3 Human IL-6 Immunoassay- ELISA

The Enzyme-Linked Immunosorbant Assay, or ELISA, is a biochemical technique used to detect the presence of a protein (antibody or antigen) in a sample. A fluorescing enzyme is linked to the antibody or antigen to be detected and the fluorescence level generated by the enzyme upon binding to the protein is used to quantify the amount of protein present.

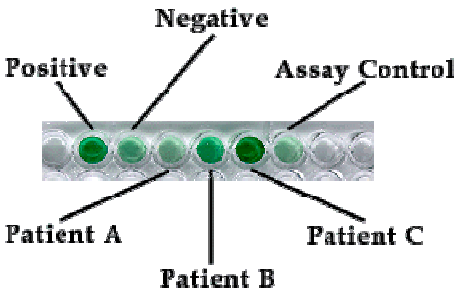

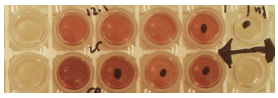

The actual modified ELISA test kit with IL-6

Figure 3.1. A multi-well plate such as the one shown above might be used for ELISA. Positive and negative controls are included in the plate and give an indication of the luminescence required for the detection of the protein. Patient C tests positive for the protein while patient A tests negative Also shown is the actual modified ELISA test kit.

Because the ELISA can be performed to evaluate the presence of both antigens as well as antibodies in a sample, it is a useful tool both for determining serum antibody

concentrations (such as with the Human Immunodeficiency Virus, HIV test or West Nile Virus) and also for detecting the presence of antigen. Fig. 3.1 indicates a multi-well plate typically used for ELISA testing.

3.3 Protein immobilization on ZnO/Si and SiO_2/Si substrates

3.3.1 Immobilization procedure

Typical protein immobilization procedure on SiO_2 requires first a hydroxylation step. The hydroxylized surface is then silanized, using 3-Aminopropyltriethoxysilane (ATES). ATES is used as the bridge to which gluteraldehyde is bound. This surface modification allows the bovine serum albumin (BSA) to covalently bond to gluteraldehyde, and the IL-6 to bond to BSA.

The hydroxylation surface modification process on SiO_2 surface was achieved by sonication in (NH_4OH: H_2O_2: H_2O =1:1:10) at 80^oC for 5 min, thorough rinsing in ultra pure deionized water, and drying in N_2 gas. Our investigation of the ZnO thin films showed that the hydroxylation step was not required. The ZnO surface unlike that of SiO_2, has a high density of unsaturated bonds, which, upon contact with ultra pure water hydroxylizes readily without the need of the NH_4OH treatment.

The silanization process of the ZnO/Si and SiO_2/Si samples was done with 3-Aminopropyltriethoxysilane (ATES 99%, Aldrich) solution: (95% aqueous solution of ethanol= 4:100 by volume) at room temperature for 4 to 5 hours. The alkylamininosilane-derivatized surface was formed and rinsed by sonication in ethanol for 1 to 2 minutes, washed in ultra pure water and baked at 110 ^oC for 10 to15 min, before inserting the sample in the SEM for visualization. The silanized ZnO/Si and SiO_2/Si samples were treated with a 2ml of 2% gluteraldehyde solution (Grade I, 70% Sigma) in 10 mM

sodium phosphate-buffered saline (PBS) at pH 7.4, shaking for 12 hours at 4°C. The sample was washed thoroughly in ultra pure water to remove the excess gluteraldehyde, and then dried in N_2 gas, before inserting in the SEM for visualization.

The aldehyde activated surfaces were used for covalent attachment of the bovine serum albumin (BSA-Sigma Aldrich). The BSA concentration was adjusted to 0.1mg/ml with 10 mM PBS, and 1 to 2ml of BSA in PBS solution was incubated for 12 to 18h at 4°C in a shaker. The samples were rinsed three times in 10mM of PBS, rinsed in ultra pure water, and dried in N_2 gas. IL-6 [rhL-6 recombinant human-*E. coli* derived-10µg, R&D System, Minneapolis MN, 55413] proteins were bound electrostatically to BSA. Different concentrations of IL-6 (100pg/ml to 2µg/ml) were diluted in a 0.1mg/ml BSA solution in 10 mM PBS, and 10 to 15µl were spotted on the samples and kept for 12 to 18h at 4°C.

3.3.2 Modified Human IL-6 Immunoassay-ELISA

For the quantitative determination of the human IL-6 protein on the samples, a Quantikine High Sensitivity Human IL-6 Immunoassay kit [139] suitable for serum, plasma, and urine, was used. The Quantikine HS Human IL-6 Immunoassay is a 6 hour solid-phase ELISA where the fluorescence is generated by the enzyme linked to the protein in the assay (in solution form). However, in order to be able to measure our protein on the ZnO and SiO_2 surfaces, we developed an alternative method with the kit suitable for the oxide surfaces, which we designated as the modified ELISA.

Different concentrations of IL-6, namely 2µg/ml, 1µg/ml, 500ng/ml, 200ng/ml, 50ng/ml, 25ng/ml, 12.5ng/ml, 6.25ng/ml, 1ng/ml, 500pg/ml, 100pg/ml, 20pg/ml and 5pg/ml in 0.1mg/ml BSA solution, was immobilized on the ZnO and SiO_2 samples was

prepared. To measure the amount of IL-6 bound on the oxide surfaces, we inserted 0.5x0.5mm^2 ZnO and SiO_2 samples (in duplicate) into each well of the kit and added 200µl of calibrator RD6-F solution [141]. In order to determine the specificity of the method for the oxide surfaces, and exclude cross-reactivity of the kit, an untreated control sample of the substrates was also measured. Also, duplicate samples without any treatment, but with just the 0.1mg/ml BSA, were included in the measurement. Furthermore, in order to determine accurately the quantitative amount of protein binding, 100µl of the supernatants (residue floating on the surface) from the third wash of the samples were measured in duplicate.

To determine the IL-6 concentration on each sample, a standard curve (amount of IL-6 deposited Vs that applied) was generated for each set of samples. For this 200µl of different concentrations (0pg/ml, 0.156pg/ml, 0.312pg/ml, 0.625pg/ml, 1.25pg/ml, 2.5pg/ml, 5pg/ml, and 10pg/ml) of IL-6 in an assay form was prepared in duplicate. With the control duplicate samples, and with the measurement of supernatants from the third wash, the method is developed here to be applicable to the ZnO and SiO_2 surfaces for the first time, providing a high degree of accuracy in the measurements.

ZnO/Si and SiO_2/Si samples without any treatment, but with different concentrations of IL-6 (50ng/ml, 25ng/ml, 12.5ng/ml, 1ng/ml) in 0.1mg/ml BSA solution, were also incubated overnight (16-24 h), and the physical adsorption (non-specific) of the bound protein onto both oxide surfaces, was measured.

3.3.3 Morphology Evaluation During Protein Immobilization

The evaluation of the morphology of ATES, gluteraldehyde, BSA, and IL-6, was performed using a scanning electron microscope (SEM) (JEOL JSM-T330). Using

atomic force microscopy (AFM) a magnified portion of the same area seen in the SEM, was examined. The AFM demonstrates the 2- and 3-dimensional (2D, 3D) distribution, the morphological features, and the size and density of the biomaterials bound onto the substrates, as well as any imperfections on the surface of the substrate itself.

All ZnO and SiO_2 samples were inspected in the SEM prior to any immobilization treatment and the surfaces were found to be morphologically featureless and clean. A schematic diagram of the immobilization steps and the chemical reactions on ZnO and SiO_2 surfaces is shown in fig. 3.2.

Our studies indicated that due to a large concentration of unsaturated bonds, the ZnO surface hydroxylizes readily in water without any special procedure, unlike SiO_2, which requires treatment with $NH_4OH:H_2O_2:H_2O$ for hydroxylation. In Fig.2, the first stage indicates the silanization process of the substrates, where ATES binds with two hydroxylated bonds of ZnO, while one bond is left dangling. In SiO_2 however, there are no dangling bonds present. In the second stage, ATES acts as a bridge to which gluteraldehyde is bound. This allows the chemical attachment of the terminal aldehyde group in gluteraldehyde to the amine group of the protein or antibody (BSA, or BSA+IL-6) as seen in the third stage. This method avoids non-specific attachment of the protein directly to the solid phase [140].

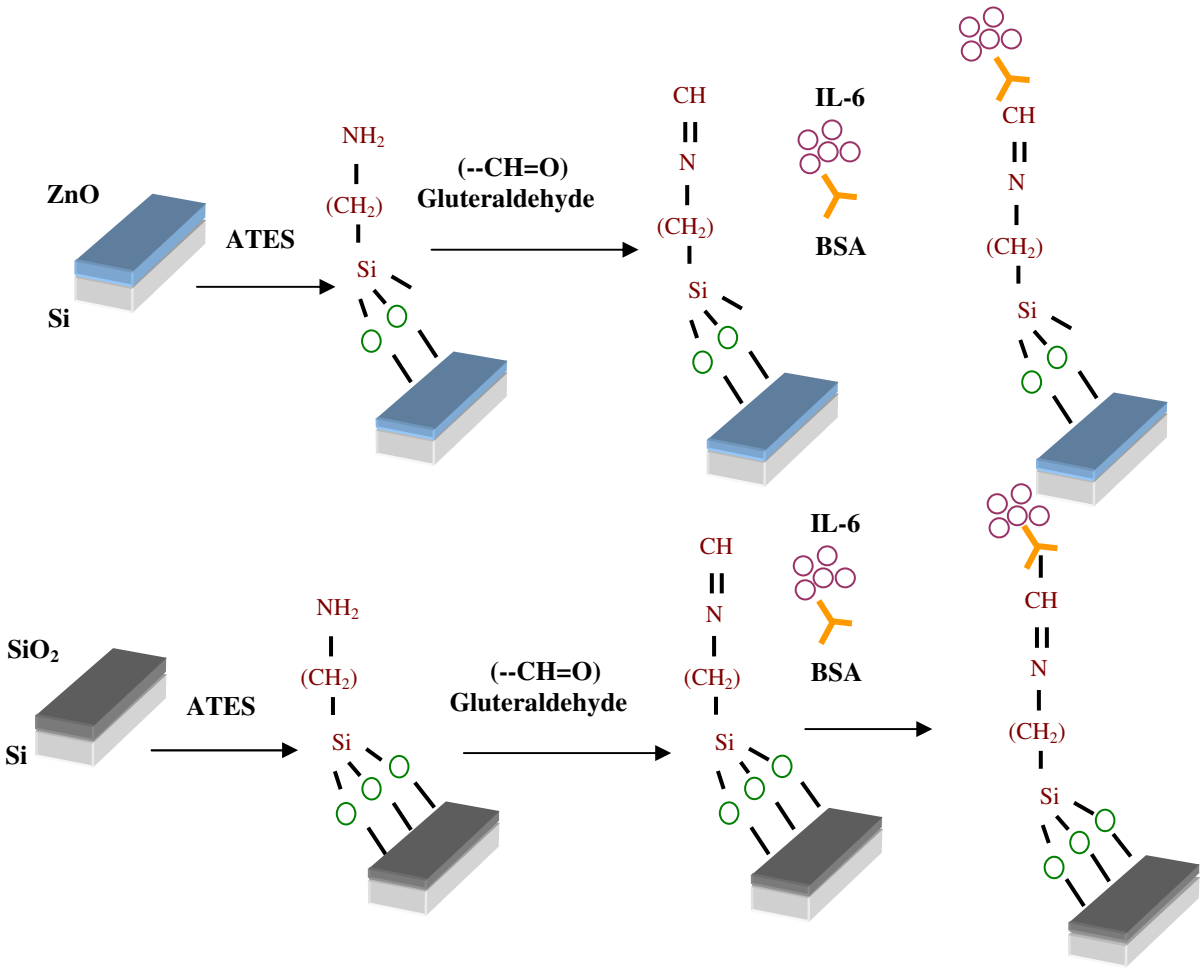

Figure 3.2: Schematic protocol for immobilization of interleukin-6 on ZnO and SiO_2. The hydroxylized surface of the oxides is silanized using ATES. The amino group generated by this process subsequently binds with the aldehyde (–CH=O) group from gluteraldehyde. This aldehyde group is used to make a covalent bond with the BSA and IL-6 binds electrostatically onto BSA.

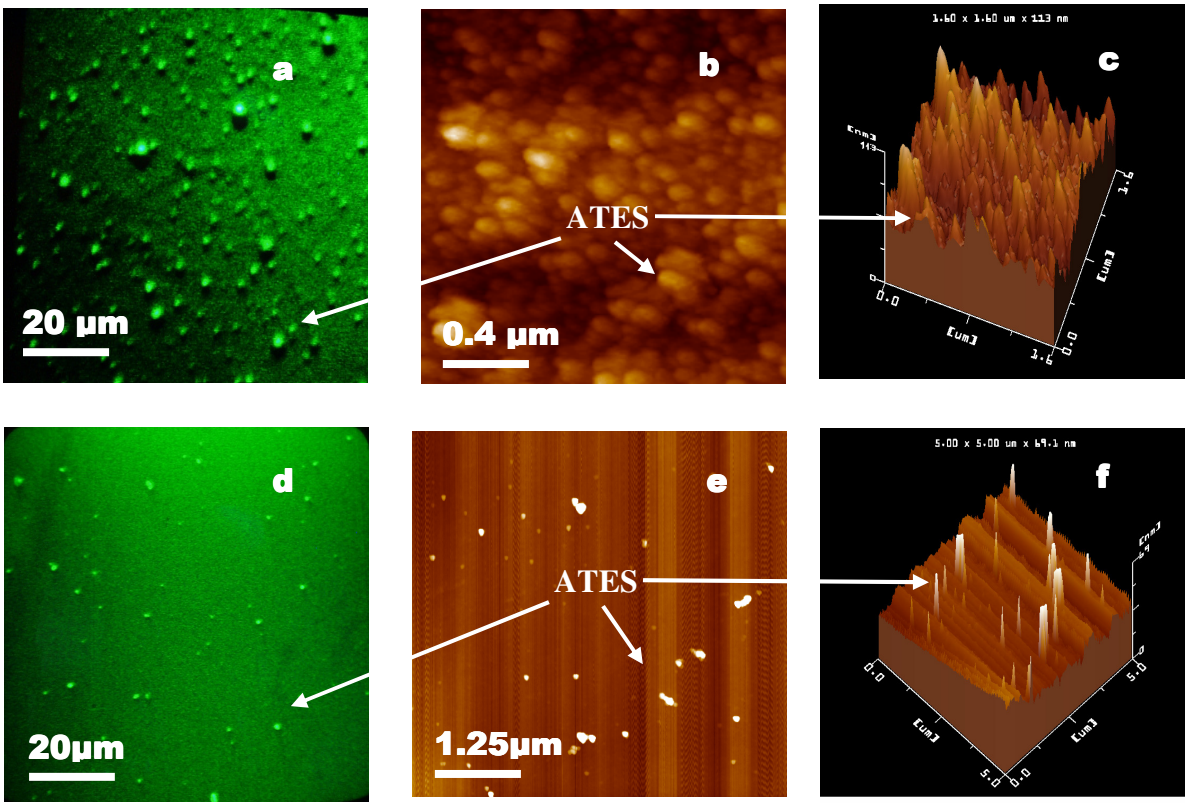

Figure 3.3: SEM and AFM images of ATES bound onto ZnO/Si and SiO_2/Si samples. (a) SEM image of an 80x60µm^2 area on ZnO/Si indicating ATES particles. (b) The 2-D AFM image of a magnified portion (1.6x1.6µm^2 area) of the same ZnO surface (c) The 3-D AFM image of the same area as in (b) (d) The SEM image of an 80x60µm^2 area of ATES particles on SiO_2 (e) The 2-D AFM image of a magnified portion (5x5µm^2 area) of the SiO_2 surface. (f) The 3-D AFM image corresponding to the same portion as in (e)

Fig. 3.3 shows the SEM and AFM images of the ZnO/Si (Fig. 3.3 a-c) and SiO_2/Si (Fig. 3.3 d-f) samples after 4 hours of treatment with ATES. On the ZnO surface, the ATES treatment produces an average of 70-110 coagulated ATES particles in an area of 60x80µm^2 (Fig. 3.3a) a size distribution ranging from 0.5 to 4µm. Fig. 3.3b is the 2D AFM image of a magnified portion (1.6x1.6µm^2) of the area seen in the SEM (Fig. 3.3a), where the coagulated morphology of the ATES particles is evident. These coagulated particles consist of smaller particles with a size distribution of 0.1-0.2 µm. In Fig. 3.3c

the 3D AFM image provides a measure of the height of the particles. In this case a height of 113nm is noted. In contrast, the ATES treatment of the SiO_2 surface produces significantly less particles per unit area on the surface. The SEM image in Fig. 3.3d shows an average of 40-80 coagulated ATES particles in a 60x80µm^2 area, which represents 25-40% less ATES particles on SiO_2 than on ZnO. The size distribution is smaller (0.5-2µm) than that on ZnO. The height of the particles is also significantly lower at 69nm as the 3D AFM image in Fig. 3f shows.

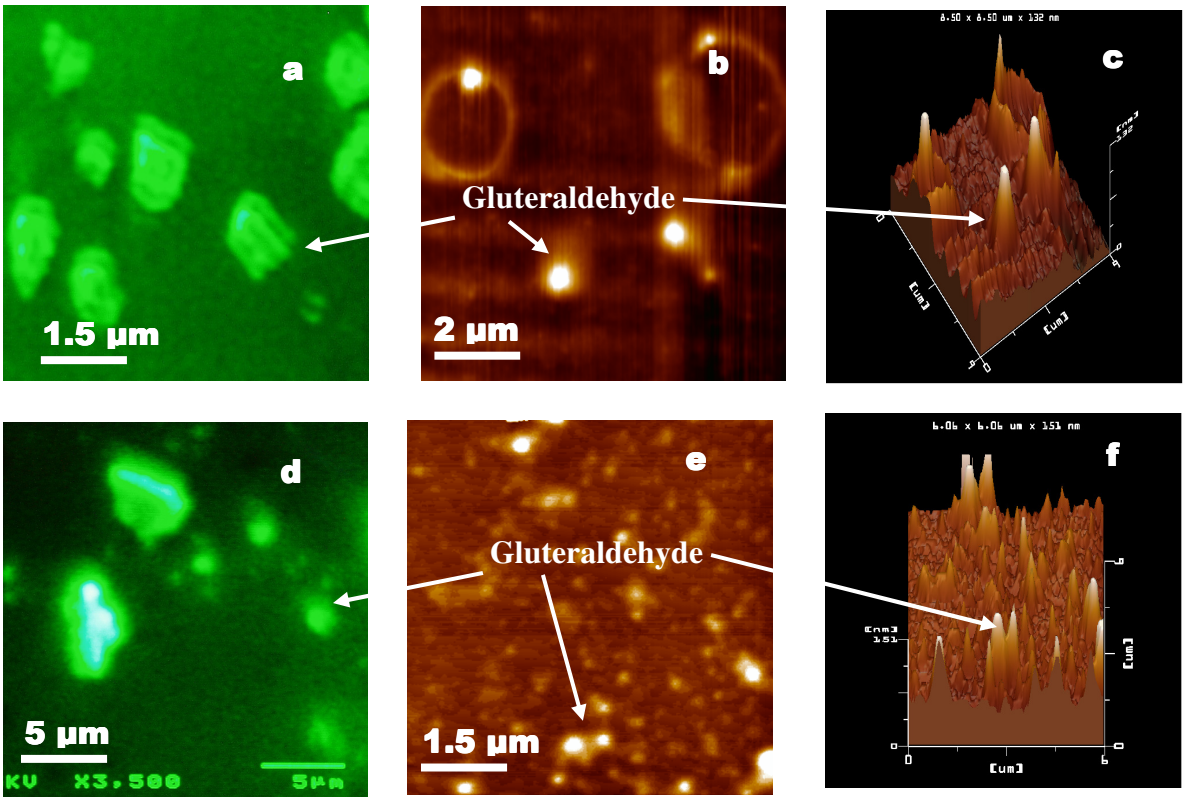

Figure 3.4: SEM and AFM images of gluteraldehyde particles bound onto ATES. (a) The SEM image of a 20x15µm^2 area on ZnO indicating coagulated particles of gluteraldehyde and ATES. (b) The 2-D AFM image of a magnified portion (8.5x8.5µm^2 area) of gluteraldehyde on ATES on ZnO (c) The 3-D AFM image corresponding to the same area as seen in (b). (d) The SEM image of a 20x15µm^2 area on SiO_2 (e) The 2-D AFM image of a magnified portion (6x6µm^2 area) of the SiO_2 surface. (f) The 3-D AFM image of the same portion as seen in (e).

Fig. 3.4 shows the SEM and AFM images of the silanized ZnO/Si (Fig. 3.4 a-c) and SiO_2/Si (Fig. 3.4 d-f) samples after 4 hours of treatment in 2% gluteraldehyde. Gluteraldehyde has a higher brightness making it more easily visible than the ATES. The SEM image in Fig. 3.4a shows the gluteraldehyde particles bound onto ATES on a 15x20μm^2 area of ZnO surface. Typical size distribution is 1 to 2µm as shown in the image, although larger area surveys showed a limited number of particles with sizes around 4µm. The number of ATES+gluteraldehyde particles as seen in AFM is 24-40% more on the ZnO surface as compared to that of SiO_2. In the 2D AFM image of a magnified portion (8.5x8.5μm^2) of the 15x20μm^2 area of Fig. 4b, a morphology of circular crowns and distinct spherical particles due to the gluteraldehyde, is evident. The 3D AFM profile of this portion (Fig. 3.4c) indicates the corresponding heights of the crowns and the particles produced by the binding of gluteraldehyde onto ATES. The maximum height of these particles is 132nm on ZnO and 151nm on SiO_2 (Fig 3.4f). The SEM image in Fig. 3.3d shows gluteraldehyde particles bound onto ATES in a 20x15μm^2 area of the SiO_2 surface. The size distribution varies between 1 to 4 µm. The 2-D AFM image of a magnified portion (6x6μm^2 area) of the SiO_2 surface in Fig 3.4d indicates no circular morphology, but the particles are mostly rounded.

Fig. 5 shows the SEM and AFM images of the ZnO (Fig. 3.5 a-c) and SiO_2 (Fig. 3.5 d-f) surfaces with BSA bound covalently onto the gluteraldehyde particles. As seen in the SEM image of a 10x5μm^2 area on ZnO in Fig. 3.5a, the protein tends to arrange itself around the gluteraldehyde particles. The arrangement of BSA around the gluteraldehyde is shown also in the 3D AFM image in Fig. 3.5c for ZnO, where the maximum height of the particles is 1.53µm with a lateral size distribution of 4 to10µm. The SEM image of a

25x15µm^2 area on SiO_2 in Fig 3.5c, shows the BSA bound onto gluteraldehyde with a lateral size distribution is typically between 2 and 5µm, consistently smaller than that seen on ZnO. The AFM images of BSA bound to gluteraldehyde onto the SiO_2 surface, are shown in Fig. 3.5e and 3.5f. In this case the height is significantly lower at 691nm, demonstrating that ZnO binds more of the protein than the SiO_2 surface.

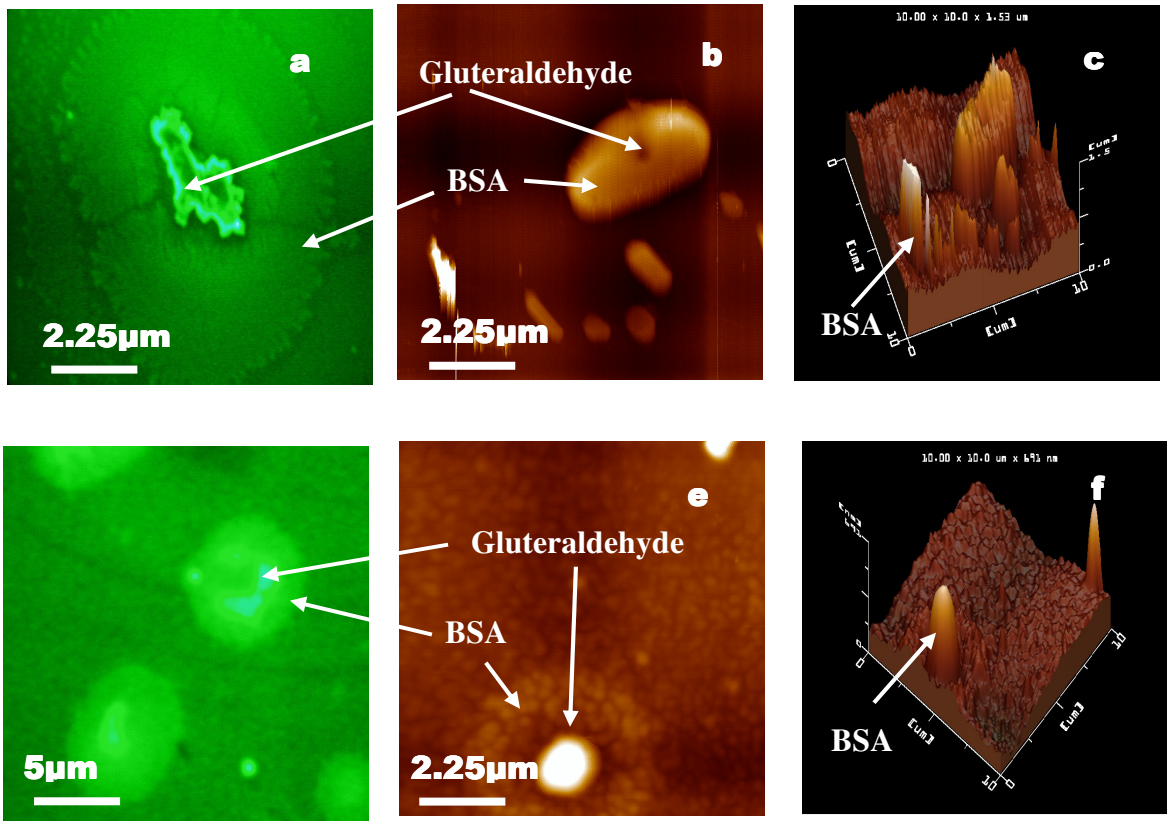

Figure 3.5: SEM and AFM images of BSA bound onto gluteraldehyde (a) SEM image of a 10x5µm^2 area on ZnO after the application of BSA. (b) 2-D AFM image of a 10x10µm^2 area of ZnO. (c) The 3-D AFM image corresponding to the same area as in (b) gives a maximum particle height of 1.53µm. (d) The SEM image of a 25x15µm^2 area on SiO_2 shows the BSA bound onto gluteraldehyde. (e) The 2-D image of a 10x10µm^2 portion of the SiO_2 surface with BSA bound to gluteraldehyde. (f) The 3-D AFM image of the same portion as seen in (e).

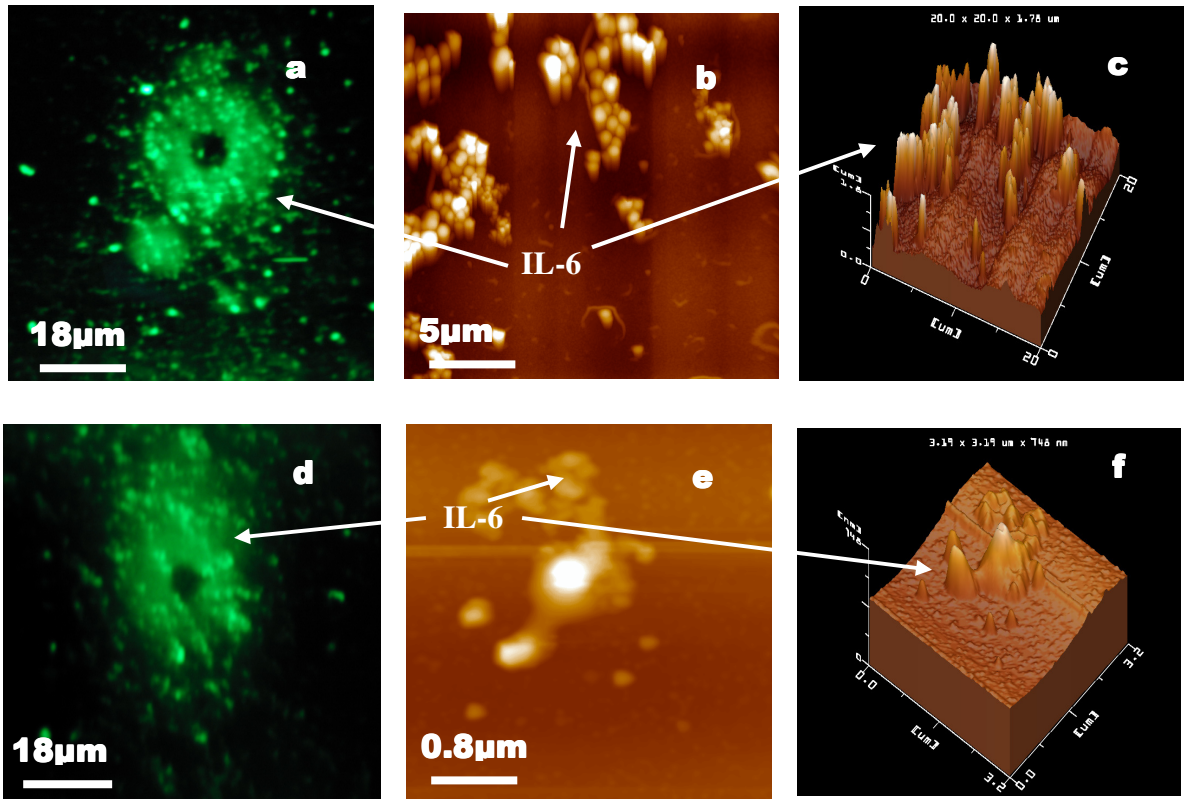

Figure 3.6: SEM and AFM images on application of IL-6. (a) SEM image of a 75x50µm^2 area on ZnO/Si indicating a large circular cluster with a diameter around 26µm. (b) The 2-D AFM image of magnified portion (20x20µm^2 area) of the ZnO surface. (c) The 3-D AFM image of this portion indicates a maximum height of 1.78µm for the particles. (d) The SEM image of a 75x50µm^2 area on SiO_2/Si, shows a large circular cluster similar but not as dense as that on ZnO, with typical sub-cluster size distribution of 2 to 5µm. (e) The 2-D AFM image of a magnified portion (3.2x3.2µm^2 area) of the SiO_2 surface. (f) The 3-D AFM image of the same portion indicating a maximum height of the particles of 748nm.

Fig. 3.6 shows the SEM and AFM images of the ZnO (Fig. 6 a-c) and SiO_2 (Fig.3.6 d-f) surfaces of BSA bound to gluteraldehyde and IL-6 bound to BSA. IL-6 binds electrostatically onto BSA in larger clusters. As seen in the SEM image of a 75x50µm^2 area on ZnO/Si in Fig 3.6a, the protein tends to form large circular clusters with diameters around 26µm. A closer look through the 2-D AFM image (Fig 3.6b) of magnified portion (20x20µm^2 area) of the ZnO surface, reveals sub-cluster formation

with lateral size distribution of 4 to 10µm, consisting of individual particles with a size distribution of 1 to 1.5µm. The 3D AFM image of the IL-6 on BSA/gluteraldehyde on ZnO seen in Fig. 3.6c, provides a maximum particle height of 1.78µm. In comparison, the maximum height on the SiO_2 surfaces, measured at 748 nm (from Fig 3.6f), is significantly lower at than that on ZnO. The cluster formation is similar to that on ZnO, but not as dense with the particle lateral cluster-size distribution on SiO_2 (Fig 3.6d), measured at 2 and 5µm consisting of individual particles with a size distribution of 0.4-0.6µm.

Table3.1 shows the increase in the size of the biomaterials in each intermediary step on both substrates, and provides an indication of the progression of the immobilization process. The results here also indicate that the binding of the proteins is more efficient on the ZnO than the SiO_2 surface, as indicated from the higher density, size and height distribution of the proteins immobilized on the ZnO surface.

	ZnO/Si Height	SiO_2/Si Height	ZnO/Si Lateral size	SiO_2/Si Lateral size
ATES	113 nm	69 nm	0.5-4 µm	0.5-2 µm
ATES+gluteraldehyde	132 nm	151 nm	1-2 µm	1-5 µm
ATES + glut + BSA	1.53 µm	691 nm	4-10 µm	2-5 µm
ATES + glut + BSA+IL-6	1.78 µm	748 nm	4-10 µm	2-5 µm

Table 3.1: Particle maximum height and lateral size distribution at each intermediary step of protein immobilization on ZnO and SiO_2 surfaces.

3.3.4 Biochemical Analysis : Results from ELISA

In order to determine biochemically that the IL-6 protein is not denatured and remains active while bound onto the oxide surface and determine its concentration, the modified ELISA (Enzyme Linked Immunosorbant Assays) technique developed in this

work, was performed on both ZnO/Si and SiO_2/Si samples incubated with different amounts of protein. Table II shows the results of modified ELISA for the quantitative determination of IL-6 on ZnO/Si and SiO_2/Si substrates. A wide range of different concentrations of IL-6 (2μg/ml, 1μg/ml, 500ng/ml, 200ng/ml, 50ng/ml, 25ng/ml, 12.5ng/ml, 6.25ng/ml, 1ng/ml, 500pg/ml, 100pg/ml, 20pg/ml and 5pg/ml) in 0.1mg/ml BSA solution, was applied on the surfaces of ZnO and SiO_2, in order to determine the amount of incubated protein that falls within the measurable range of the standard curve of the kit (i.e. between 0.156pg/ml and 10pg/ml). The results in Table II show the amount of protein bound on both surfaces, which was between 500pg/ml-12.5ng/ml.

Amount of IL-6 protein applied to each substrate (ng/ml)	Amount of IL-6 protein measured on ZnO/Si (pg/ml)	Amount of IL-6 protein measured on SiO_2/Si (pg/ml)
12.5	10.150	1.159
6.25	4.500	0.707
1.00	0.642	0.368
0.50	0.364	0.276

Table 3.2: Modified ELISA measurement of IL-6 specific binding on the ZnO and SiO_2 surfaces

Also the results for all the control samples with bare surfaces showed a small cross reactivity ranging between 0.06pg/ml and 0.2pg/ml for both substrates, which gives the base line of the measurement. Table II also indicates that protein binding on the ZnO surface is 2 to 8 times more than that seen on the SiO_2 surface. This increased binding capability on ZnO, is probably due to the high density of unsaturated bonds of the ZnO surface. Covalent binding of proteins through the gluteraldehyde process ensures that the

proteins are in the correct conformation and remain functional. This is significant for the development of biosensors where the proteins must retain their biological reactivity by maintaining the correct conformation. There is, however, evidence that physical adsorption of the protein (BSA+IL-6) directly onto the surface of both substrates, is also possible. We found that protein immobilization through physical adsorption on ZnO/Si thin films can be achieved from aqueous solutions at 4 ^{0}C, and, as measured by the modified-ELISA. Protein binding is mainly electrostatic and controlled by the pH, the protein charge and the solution ionic strength [141]. Incubation of BSA and IL-6 overnight between 1ng/ml and 50ng/ml on untreated ZnO/Si substrates, indicates significant physical adsorption of the protein directly onto the surface of the substrates. Also, the amount of protein that physically adsorbs onto ZnO surface is larger than that adsorbed onto SiO_2. The experiments have been carried out in a buffer solution of PBS with a pH of 7.4. The isoelectric points (IEP) of BSA and IL-6 are approximately 4.7 and 4.0-5.3 respectively. This suggests that the amino acid chains in BSA and IL-6 contain a greater amount of acidic functional groups. The BSA and IL-6 carry a negative charge in the PBS solution since the isoelectric points of the proteins are lower than the pH of the solution. Thus, they are attracted to ZnO, which has an IEP ≅ 9.5 and carries a positive charge in the PBS buffer solution, resulting in higher physical adsorption on the surface. SiO_2 on the other hand, has an IEP ≅ 2.0 and therefore carries a greater negative charge in the PBS solution than the proteins and consequently there is less electrostatic attraction between the two, and hence, lower physical adsorption. However, since this is not a specific chemical binding, it is neither fully controllable, nor stable. This means that repeated experiments yield different quantities of protein adsorption on the untreated

samples and also that the adsorbed proteins are removable and washable. Also, there is evidence in the literature, that physical adsorption tends to denature many proteins or disrupt their quaternary structure [142,143]. Previous findings indicate that proteins can bind to layers of polyions regardless of their charge [144,145]. Our results indicate that direct binding of BSA and IL-6 by physical adsorption, is realizable on ZnO surfaces, which is supported also by the findings of Zhang et al [146] for the immobilization of uricase on ZnO nanorods.

3.4 Summary

This chapter describes the development of the immobilization technique to achieve specific protein binding of BSA and BSA and IL-6 on ZnO and SiO_2. The process was validated both qualitatively by visualization through AFM and SEM, and quantitatively by a modified ELISA Quantikine HS IL-6 Immunoassay for the first time. The comparative study between ZnO and SiO_2 showed that the ZnO surface has significantly better binding properties than SiO_2. Furthermore, we found that non specific direct binding of BSA and IL-6 on ZnO without any chemical treatment, can also be effectively achieved by physical adsorption due to the high isoelectric point (IEP~9.5) of the ZnO as compared with the SiO_2 isoelectric point (IEP~2.0) which falls below the IEP of the proteins.

The direct visualization of the protein immobilization through AFM and SEM in each intermediary step, showed increase in the height and size of the bioparticles. The modified ELISA measurements of the chemically treated samples had a protein detection range between 500pg/ml-12.5ng/ml. Modified ELISA also indicated 2-8 times more IL-6 binding on ZnO/Si substrates than SiO_2/Si substrate. It is concluded that the important

properties of the surface of ZnO make it a highly promising material for novel biosensor development.

CHAPTER 4 : DEVELOPMENT OF A GUIDED SHEAR HORIZONTAL SURFACE ACOUSTIC WAVE DEVICE

4.1 Acoustic Wave Devices in sensor applications

Interest in surface acoustic wave (SAW) devices for sensing applications in gaseous and liquid media has been growing. Interaction of a targeted biomaterial in gaseous or liquid environment with the sensor surface alters acoustic wave propagation allowing their detection through change in the velocity of the acoustic wave. Specifically, mass loading caused by the biomaterial results in a decrease in the acoustic wave velocity and in the case of a resonator, the frequency of the device.

The sensitivity to mass loading depends on the acoustic energy density within the active layer of the device. Bulk acoustic wave (BAW) devices are resonant structures where the wave travels form the top excitation surface to the opposite detection surface and thus the energy is confined in the bulk of the piezoelectric crystal. In practice, sensitivity of the device depends largely on the thickness of the piezoelectric crystal [147-149]. In order to maximize the acoustic energy present in the active layer, and hence the sensitivity, the thickness needs to be minimized, which will then affect the durability of the device, making the extremely thin crystals brittle. This necessitates the development of device structures utilizing surface acoustic waves for detection, to increase sensitivity. The basic structure of a SAW device consists of metal inter-digitated (IDT) fingers fabricated on a piezoelectric substrate that act as electrical input and output ports as seen in Fig. 4.1. The metal electrodes on either side serve to reflect the propagating wave and create a standing wave in the device, thus forming a resonator. Application of a ac signal to the input transducer generates a surface acoustic wave that

propagates to the output transducer, which converts it back to an ac signal at the resonant frequency. Mass loading on the device causes a shift in the acoustic velocity of the waves and hence a reduction in the resonant frequency of the device. This decrease in frequency is used as a measure of the mass applied.

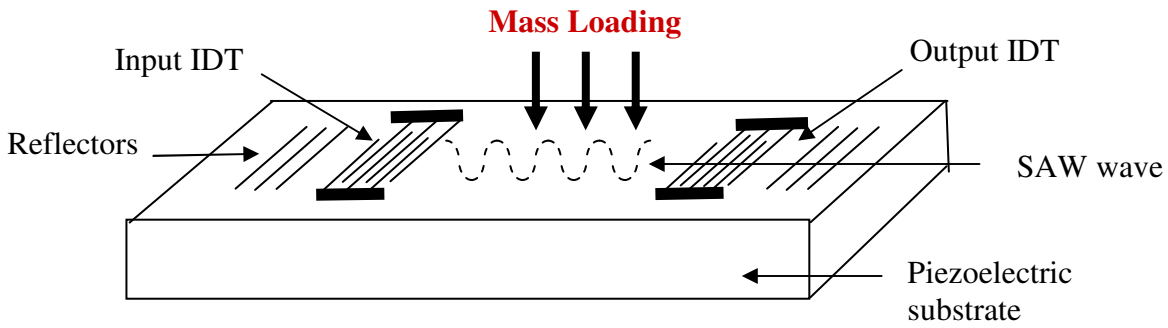

Figure 4.1: Surface acoustic wave resonator with input and output inter-digitated (IDT) fingers. The mass loading causes a shift in the acoustic velocity and hence frequency of the resonator.

For sensing in liquid environments, longitudinal bulk modes, Rayleigh surface waves, and most Lamb-wave devices present a significant loss of energy into the liquid under test [150,151]. In these devices, the direction of particle motion is perpendicular to the plane of the traveling wave and results in compressional stresses in the liquid under test. As seen in Fig. 4.2, for surface waves propagating along the x-axis, the particle displacement in longitudinal waves is along the z-axis making it susceptible to attenuation in liquid environments. Thus the acoustic wave suffers large attenuation before it is captured by the output IDT. When the mass being sensed is deposited from the liquid phase, the choice of acoustic wave devices is one with a shear horizontal polarization of the displacement, such that the displacement of particles is in the plane of the resonator, and energy is not transferred to the liquid. These types of surface acoustic waves are shear horizontal (SH) plate mode waves [152], surface transverse waves [153],

and guided shear horizontal waves or Love mode waves [154,155]. Love mode wave devices offer the advantage of concentrating the acoustic energy in a guiding layer grown on an appropriate substrate. This is done by optimizing the guiding layer thickness to achieve higher mass sensitivities.

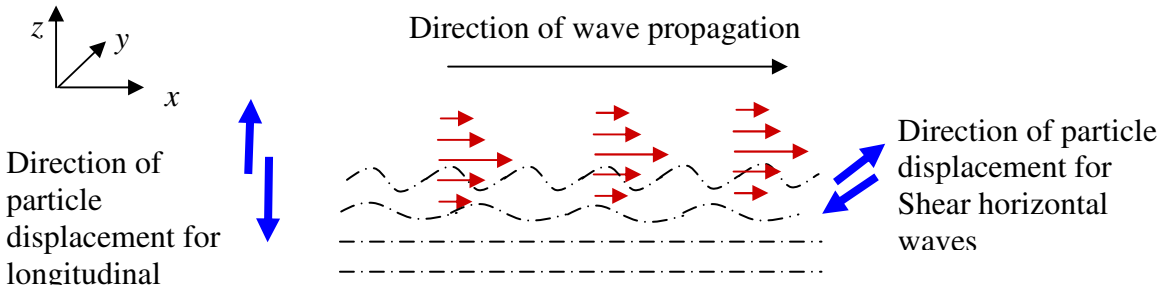

Figure 4.2: Schematic diagram of particle displacement for surface longitudinal and shear surface horizontal waves

The use of Love mode SAW (LM-SAW) devices for biochemical sensing with SiO_2 as the guiding layer has been previously reported [156,157]. Development of ZnO guiding layer based Love mode devices is currently under research with recent reports of ZnO Love mode devices on diamond and quartz substrates [158,159]. The development however, of a Love mode device on Si substrates, has not yet been reported. This thesis deals with the development of such Love mode SAW device having ZnO as the guiding layer grown by PLD on SiO_2/Si substrates, to take advantage of integration with established CMOS technology.

4.2 Development of a ZnO/SiO_2/Si Love Mode Surface Acoustic Wave Device

A Love wave is a shear horizontally polarized acoustic wave that is localized to be guided by a layer which has a shear acoustic speed less than that of the half-space

material [160,161]. The phase velocity of the Love wave is intermediate between that of the substrate and the layer and is determined by the layer thickness.

The figure below shows schematic diagram of the $ZnO/SiO_2/Si$ Love mode surface acoustic wave (LM-SAW) device.

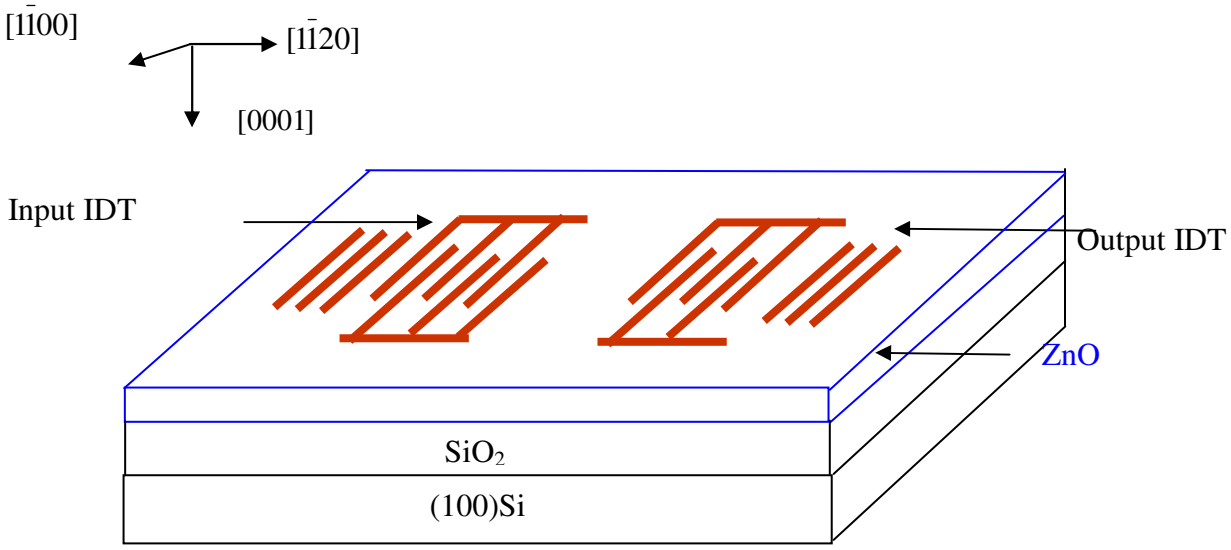

Figure 4.3: Schematic diagram of the $ZnO/SiO_2/Si$ LM-SAW device with axis orientations

A 500Å thick wet SiO_2 layer was grown on the (100)Si substrate in an atmospheric pressure furnace at 1025^0C. High quality crystalline ZnO films were grown on SiO_2/(100)Si substrates by pulsed laser deposition (PLD). The laser ablation system consisted of a KrF laser at 248 nm, operating with an energy density of 0.7 J/cm^2 and a frequency of 10Hz. The growth temperature and oxygen partial pressure were maintained at 250 ^{0}C and $1x10^{-4}$ torr respectively. The structural properties of the grown ZnO films have been treated at length in chapter 2 and generate c-axis oriented films.

The SAW devices were of the inter-digitated transducer (IDT) design fabricated by standard optical photolithography and lift-off techniques. Both micron and submicron

feature sizes were achieved. For Love mode waves in ZnO, the effective electromechanical coupling coefficient is maximum perpendicular to the c-axis in the $[1\bar{1}00]$ orientation, while for Raleigh waves it is maximum along the c-axis in the [0001] orientation [162]. If the IDTs are aligned perpendicular to the c-axis, Love mode propagation is predicted to be the dominant mode. The input and output IDT fingers consist of a 500Å aluminum layer deposited by e-beam evaporation. Increasing this thickness further can lead to unintentional mass loading of the SAW device by the fingers. Reflectors were placed on either side of the IDTs to form the SAW resonator.

The acoustic wavelength in the SAW devices is determined by the wave velocity achievable in the material and the IDT feature sizes. In theory, the acoustic wavelength is determined by

$$\lambda_0 = 2(L+S) = 2p \quad \ldots (4.1)$$

for IDTs of finger width L and finger spacing S and p is referred to as the pitch of the SAW device as seen in Fig. 4.4.

For reflection coefficient magnitudes close to unity, the quality factor for the resonant cavity is approximated by [163,164],

$$Q = \frac{d_e}{\lambda_0} \quad \ldots (4.2)$$

where d_e is the effective cavity length and accounts for the distance into the reflector at which the SAW has decayed to 1/e of its value in the cavity. This penetration distance is dependent on a number of factors including the piezoelectric substrate employed, operating frequency and metallization material and thickness used for the reflectors. The

quality factor of the resonator can be increased by decreasing the wavelength of the device and increasing the effective cavity length.

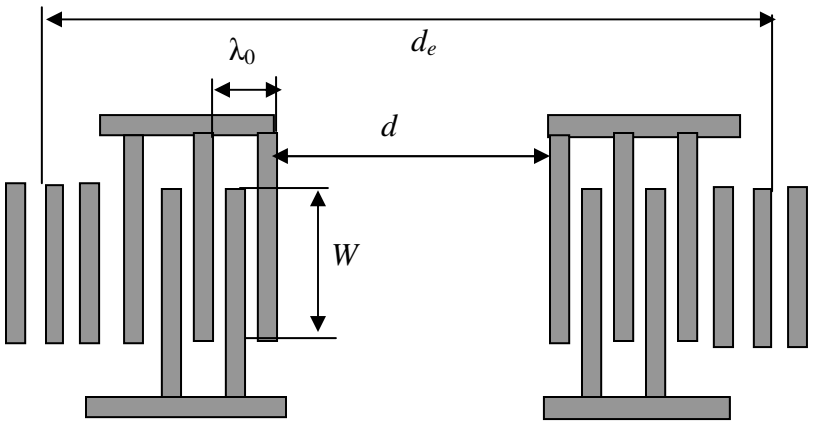

Figure 4.4: The schematic top view of the SAW resonator with wavelength λ and aperture *W*.

The leakage of shear-horizontal waves in a 2-port SAW resonator shows that the SAW energy leaks in the transverse direction of the IDTs. SAW resonator having narrow electrode fingers suppresses this transverse leakage around the resonant frequency of the device [165]. Thus, the loss can be reduced by minimizing the metallization ratio in the resonator ($\frac{L}{L+S}$).

Two sets of devices were developed. Device A was designed to operate in the sub-GHz range (λ=6.8μm) and achieve reduced insertion losses by reducing the metallization ratio from the typical value of 0.5. The device finger width and spacing of 1μm and 2.4μm respectively, yielding a metallization ratio of 0.3. Device B was designed to achieve a fundamental frequency of operation in the GHz range (λ=3.2 μm). Both the finger width and spacing were maintained at 0.8μm, thus yielding a metallization ratio of 0.5. The number of fingers in each IDT for both devices is 15. The length of the IDTs is

maintained at 45µm with an aperture of 40µm. The number of electrodes in the reflectors was 3. The geometric parameters of the SAW devices A and B are listed in the table below. Three 100µm X 100µm pads are brought out at the input and output IDTs and are used to probe the device as seen in Fig. 4.5. Fig. 4.6 shows the SEM image of devices A and B respectively. Standard photolithography has been used to obtain sub micron feature size devices with high accuracy.

Parameter	**Device A**	**Device B**
Pitch, *p*	3.4µm	1.6µm
Metallization ratio	0.3	0.5
Aperture, *W*	40µm	40µm
Length of IDT	45µm	45µm
Number of fingers	15	15
Distance between input and output IDTs, *d*	$8\lambda_0$	$15\lambda_0$

Table 4.1**:** Geometric parameters for the two port LM-SAW resonator

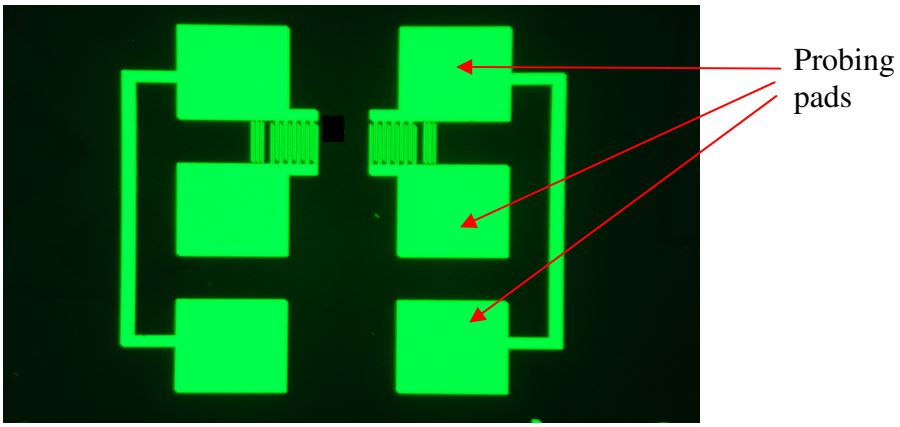

Figure 4.5: Optical Image of LM-SAW resonator

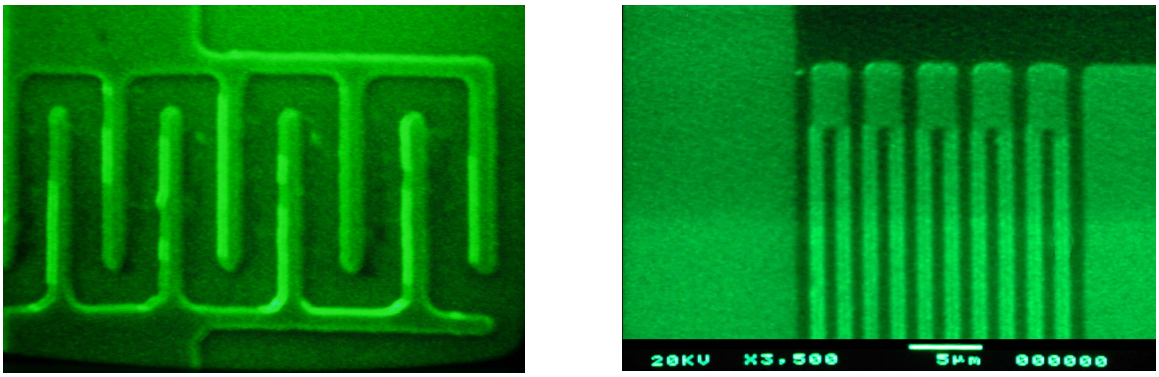

Figure 4.6: SEM images of (a) device A with finger width of 1 µm and spacing of 2.4 µm (b) Device width and spacing of 0.8 µm.

The high frequency s-parameters of the SAW devices were evaluated using a HP8510C parametric network analyzer in the frequency range of 300 kHz and 3GHz. In order to achieve impedance matching to the load line of 50Ω impedance, the length of the transmission lines leading to the measuring pads of the SAW device and the thickness of the deposited Al needed to be optimized.

4.3 Frequency Response and SAW Parameter Evaluation

The frequency response (s_{21}) of devices A fabricated on the 500Å SiO_2 layer, is shown in Fig.4.7. A narrow band-pass centered at 708 MHz (f_0) and its first harmonic at 1.41 GHz, is evident in the spectrum. The fundamental band-pass peak at 708 MHz shows minimal insertion loss at 3.42 dB and a very high side-lobe suppression of 33 dB measured from the top to the base of the peak. Insertion loss is generated due to possible bulk wave interference, acoustic attenuation through crystal imperfections, multiple SAW reflections between the bidirectional input and output IDTs and reradiation of some of the power received by the output IDTs back into the piezoelectric ZnO film.

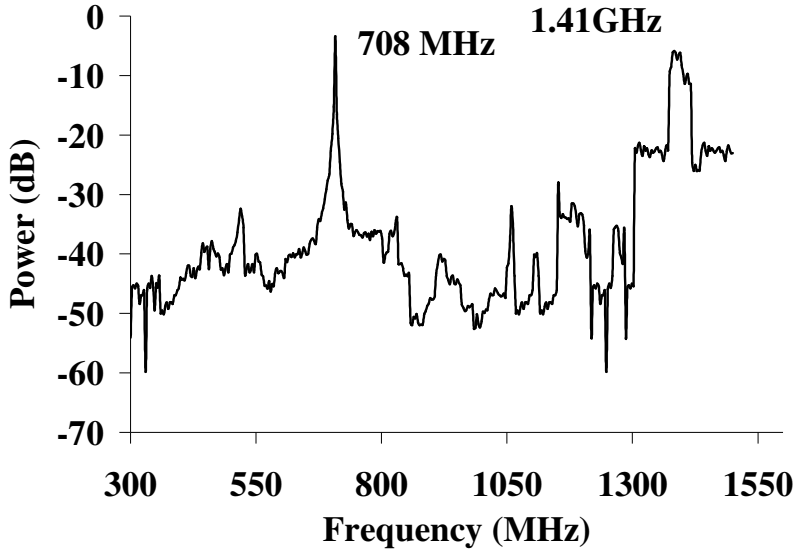

Figure 4.7: Frequency response of LM-SAW ZnO/SiO_2/Si device A with finger width 1μm and finger spacing 2.4μm, generated a fundamental frequency of 708MHz with a harmonic at 1.41 GHz

The second harmonic band-pass peak at 1.41 GHz is also seen in the figure. Theoretically the design of the SAW resonator does not support the appearance of the second harmonic. However, nonlinear elastic deformations in the ZnO layer may be responsible for such harmonics**.** From the frequency spectrum the acoustic velocity can be extracted as ($v=f_0\lambda$), and it is found to be 4814.4 m/s. The 3dB bandwidth Δf, extracted from the spectrum, is 6.1 MHz, resulting in a quality factor of 116. From equation 4.3, increasing Q would require increasing the total length of the cavity. One way to do this is to increase the number of IDT fingers and electrodes in the reflectors. Also, substituting this value of Q in Eq. 4.2 yields a cavity length of $116\lambda_0$. The length of our device is $24\lambda_0$, implying that the SAW wave travels beyond the bounds of the device and is not fully reflected by the reflectors. Thus for improving Q values the data here shows that

more reflector planes are needed. Such an approach will be appropriate for a high quality analog band-pass filter design.

The frequency response (s_{21}) of devices B fabricated on the 500Å SiO_2 layer, is shown in Fig. 4.8. For these devices the observed resonance frequency is at 1.50 GHz with a minimal insertion loss at 7.2 dB, and a high side-lobe suppression of 24 dB. The extracted acoustic velocity was the same as in device A at 4814.4 m/s. The 3 dB bandwidth is measured to be 97.1 MHz, resulting in a quality factor of 153. High side-lobe suppression was achieved in both devices. The s_{11} values were measured at -11 dB for both devices, indicating only a 10% reflection of the input power. Thus, good impedance matching is achieved without the use of external inductors and capacitors.

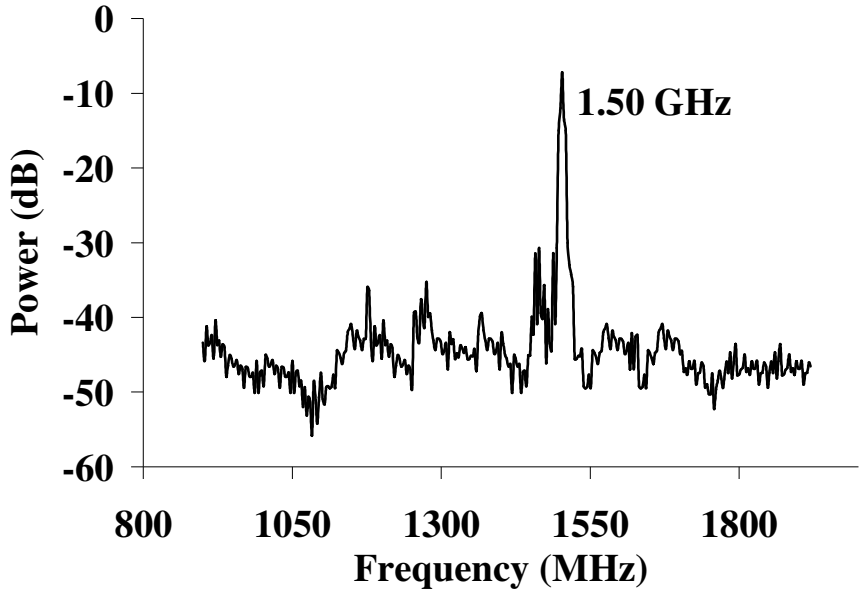

Figure 4.8: Frequency response of device B with finger width and spacing of 0.8μm, generated a fundamental frequency of 1.50 GHz.

4.4. Study of SiO_2 Thickness on SAW Device Performance

The growth of ZnO on SiO_2/Si presents a challenge due to the strain introduced in the film by the underlying SiO_2 layer. The XRD characterization indicated that growth of ZnO on a 2000 Å thick SiO_2 layer resulted in a highly strained film as indicated in Fig. 2.14. Therefore, a study on the effect of SiO_2 thickness on the strain and SAW device performance was done, and the SiO_2 thickness was optimized. Device set A was developed and characterized for a ZnO film grown on a 2000 Å thick SiO_2 layer.

The frequency response for these devices is shown in Fig. 4.9a. The spectrum indicates the presence of two peaks at 732 MHz and 1.17 GHz, which are not harmonically related. In order to understand the effects of interface strain in the operational parameters of the devices, we annealed the films before fabricating the devices. The films were annealed in air at 500 ^{0}C for 45 minutes, which, as discussed in our XRD study previously (Chapter 2), resulted in a strain reduction of 0.3 %. Annealing of the films revealed the presence of a fundamental mode at 508 MHz and its first harmonic at 1.15 GHz along with a second fundamental mode at 708 MHz. Annealing reduces the strain in the grown ZnO layers by creating defects and dislocations at the interface with SiO_2, which in turn results in the reduction of the measured acoustic velocity. This is reflected by the uniform downward shift in the frequency response by ~20 MHz, which can be used as a measure of the strain introduced in the film. The two fundamental frequencies observed at 508 MHz and 708 MHz correspond to surface acoustic velocities of 3454.4 m/s and 4814.4 m/s respectively, which indicates that the acoustic waves propagate in two different layers within the ZnO film. The higher velocity waves propagate in the top layer of the ZnO film that has reduced strain and the lower

velocity waves propagate in a ZnO layer adjacent to the SiO_2 interface where the strain is higher.

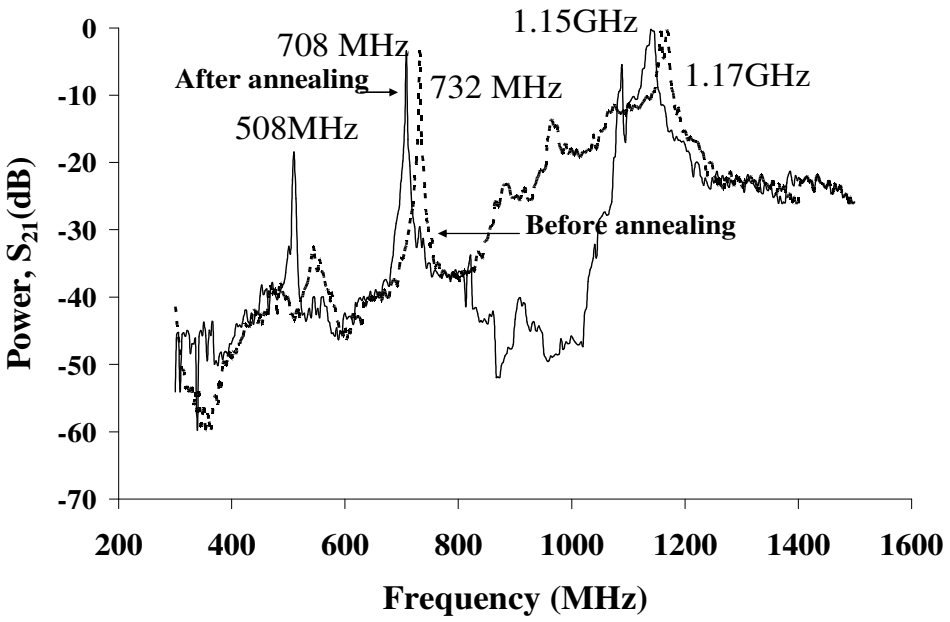

(a)

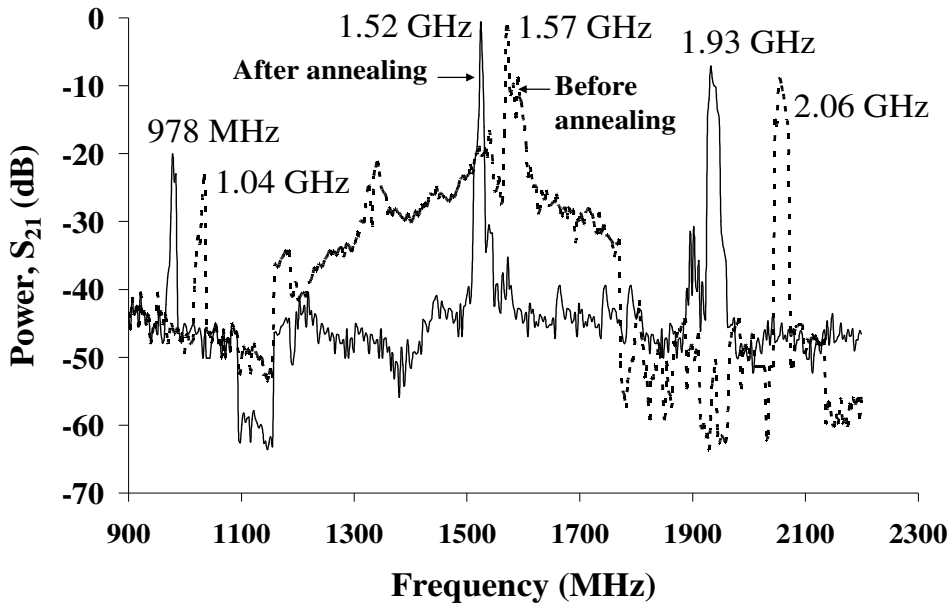

(b)

Figure 4.9: Effect of annealing on LM-SAW device performance. (a) device A fabricated on a 2000Å SiO_2 layer. Annealing causes a strain reduction to 2%, and a downward shift in the peak frequencies by 20 MHz. (b) device B fabricated on a 2000Å SiO_2 layer, indicating a similar downward frequency shift.

A similar observation is made in device B, developed also on a 2000Å thick SiO_2 layer, as shown in Fig. 4.9b. The figure shows that prior to annealing, a fundamental mode at 1.04 GHz with its first harmonic at 2.06 GHz along with a second fundamental mode at 1.57 GHz, are present in the frequency spectrum. Annealing the ZnO film at 500^0C in air, shifts the peaks downward in frequency again, and generates a fundamental mode at 978 MHz with a first harmonic at 1.93 GHz, and a second fundamental mode at 1.52GHz. These fundamental frequencies at 978 MHz and 1.52 GHz correspond to acoustic velocities of 3129.6 m/s and 4864 m/s, respectively.

Fig. 4.9 also indicate significant bulk-wave interference as seen in the upper stop-band for both sets of devices. Since bulk waves have higher velocities than surface waves, interference between bulk and SAW waves at the receiving IDT will be most pronounced at the high-frequency end of the spectrum. However, upon annealing, this interference is seen to decrease. Annealing results in the partial relaxation of strain through the generation of defects at the interface between ZnO and SiO_2 and this leads to scattering of the deeper bulk waves thus reducing their effect.

Our results show that strain plays an important role in the propagation of surface acoustic waves in ZnO films grown on SiO_2. The highly strained film generates multiple non-harmonically related frequencies. As seen in Fig. 2.15 however, reducing the SiO_2 layer thickness to 500 Å, results in a substantial reduction in strain to 0.56%, and the generation of a single acoustic velocity of 4814.4 m/s. Since mass sensitivity of a based biosensor depends on acoustic velocities, the alleviation of strain to obtain a single propagation velocity in the guiding layer is an important factor in device performance.

4.5 Dispersion Relationship of a ZnO/SiO_2/Si Love-Mode-SAW system

4.5.1 Theoretical Modeling and Numerical Simulation

The response of a guiding layer/substrate system to the deposition of a mass can be viewed as the propagation of acoustic waves in a three layer system where the mass constitutes the topmost layer [166]. This can be seen schematically in Fig. 4.10 where a three layered system with displacement in the x_2 direction is shown.

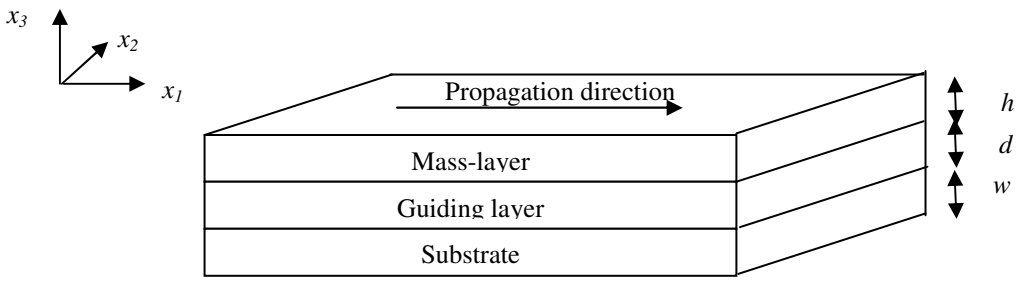

Figure 4.10: Definition of axes and propagation direction for shear horizontally polarized waves is a three-layered system, the displacement is in the x_2 direction.

For the finite substrate Love wave device, we consider a substrate of thickness, w, density ρ_s and Lame constants μ_s and λ_s, overlaid with a wave-guide layer of thickness d, density ρ_l and Lame constants μ_l and λ_l,. The third layer consists of an applied mass of thickness h, density ρ_p and Lame constants μ_p and λ_p. This is referred to as the perturbing mass layer.

Wave propagation in an isotropic material of density ρ and Lame constants λ and μ. The displacements u_j are described by the equation of motion

$$\rho \frac{\partial^2 u_j}{\partial t^2} = (\lambda + \mu) \frac{\partial S_{ii}}{\partial x_j} + \mu \nabla^2 u_j \quad \ldots (4.3)$$

The strain and stress tensors S_{ij} and T_{ij} can be expressed as follows.

$$S_{ij} = \frac{1}{2}\left(\frac{\partial u_i}{\partial x_j} + \frac{\partial u_j}{\partial x_i}\right) \quad \ldots (4.4)$$

$$T_{ij} = \lambda \delta_{ij} S_{kk} + 2\mu S_{ij} \quad \ldots (4.5)$$

The solutions to the equation of motion are chosen to have propagation along the x_1 axis with displacements in the x_2 direction of the saggital plane (x_2,x_3). They must also satisfy the boundary conditions on the displacements u and T_{i3} component of the stress tensors. Specifically, these must both be continuous at the interfaces between the substrate and the guiding layer and the perturbing mass layer. The T_{i3} component of stress tensors must vanish at the free surfaces of the substrate and perturbing mass layer.

Solution to the love wave problem is sought by using displacements in the guiding layer u_l, the substrate u_s and the perturbing mass layer u_p, as follows.

$$u_l = (0,1,0)\left[A_l e^{-jT_l x_3} + B_l e^{jT_l x_3}\right] e^{j(\omega t - k_1 x_1)} \quad \ldots (4.6a)$$

$$u_s = (0,1,0)\left[C_s e^{-jT_s x_3} + D_s e^{jT_s x_3}\right] e^{j(\omega t - k_1 x_1)} \ldots (4.6b)$$

$$u_p = (0,1,0)\left[E_p e^{-jT_p x_3} + F_p e^{jT_p x_3}\right] e^{j(\omega t - k_1 x_1)} \quad \ldots (4.6c)$$

Where ω is the angular frequency and $k_1 = \left(\frac{\omega}{v}\right)^{1/2}$ is the wave vector where v is the phase velocity of the solution. The constants A_l, B_l, C_s, D_s, E_p and F_p are constants determined by the boundary conditions specified above. A traditional Love wave solution occurs when the substrate thickness tends to infinity. Also the shear velocity of the substrate, $v_s = \left(\mu_s / \rho_s\right)^{1/2}$ is greater than the shear velocity of the guiding layer, $v_l = \left(\mu_l / \rho_l\right)^{1/2}$ and the wave vector T_s is real so that the substrate displacement, u_s decays with depth.

Substituting Eq. (4) into the equation of motion describing the layers in Eq. (4.3) with the relevant layer parameters, gives the equations for the wave vectors T_s, T_l and T_p:

$$T_s^2 = \omega^2\left(\frac{1}{v^2} - \frac{1}{v_s^2}\right) \quad \ldots(4.7a)$$

$$T_l^2 = \omega^2\left(\frac{1}{v_l^2} - \frac{1}{v^2}\right) \ldots (4.7b)$$

$$T_p^2 = \omega^2\left(\frac{1}{v_p^2} - \frac{1}{v^2}\right) \ldots (4.7c)$$

Imposing the boundary conditions and defining $\xi = \frac{\mu_s T_s}{\mu_l T_l}$, the dispersion relationship equation can be derived (the detailed algebraic treatment can be seen in [20]). The following equation represents the dispersion relationship for acoustic propagation in the three layered system.

$$\tan(T_l d) = \xi \tanh(T_s w) - \xi_p \tan(T_p h) x\left[1 + \xi \tan(T_l d)\tanh(T_s w)\right] \ldots (4.8)$$

The second term on the right-hand side of Eq. (4.8) is due to the presence of the perturbing mass layer. Setting the thickness, h, of the perturbing mass layer to zero generates the dispersion equation for the two-layer system of a substrate with a guiding layer.

$$\tan(T_l d) = \xi \tanh(T_s w) \quad \ldots (4.9)$$

Also note that as $w \to \infty$ with T*s* being real, $\tanh(T_s w) \to 1$, Eq. (4.8) gives the limit of the Love wave perturbed by an arbitrary thickness perturbing mass layer.

Eq. (4.8) has no closed form solution, thus we have numerically evaluated the relationship for a two layer system consisting of ZnO as the guiding layer and SiO_2/Si as the substrate. The guiding layer parameters are v_l = 4814 m/s and ρ_l = 5670 kg/m^3 for ZnO. Numerical results [167] on the velocity of waves in the SiO_2 layer of a ZnO/SiO_2/Si structure have indicated that as the thickness of the SiO_2 layer is reduced, the velocity of the SAW wave in the SiO_2 layer is increased. Normalized thickness is defined as the thickness of the layer with respect to λ_0 of the device. For small normalized SiO_2 layer thicknesses (<0.01), it has been shown [167] that the velocity in SiO_2 approaches that of quartz (5100m/s). Thus, under these conditions the amorphous SiO_2 layer is considered to be elastically equivalent to fused quartz. Therefore in our simulations, a substrate of thickness w=100 μm with a density and velocity typical to that of quartz (ρ= 2655 kg/m^3 and v_s=5100 m/s) were chosen.

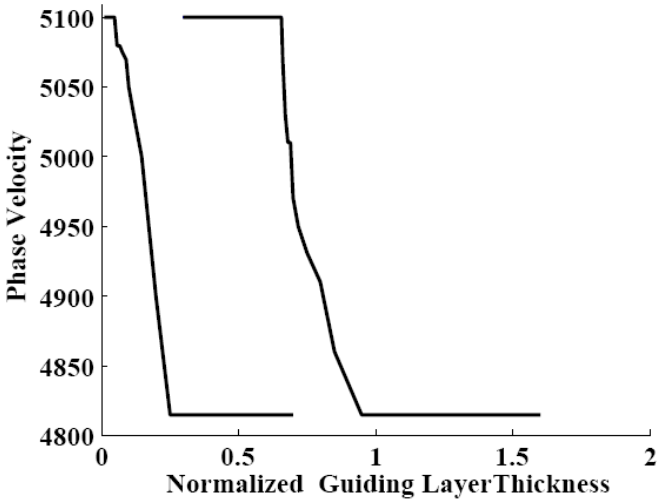

Figure 4.11: The theoretical phase velocity curves as a function of normalized guiding layer thickness ($d/\lambda_l=df/v_l$) is shown. The first two modes of love waves are indicated for a device operating at a center frequency of 700 MHz. The Love mode waves propagate with a velocity varying between 5100 m/s (SiO_2) and 4814 m/s (ZnO).

Fig. 4.11, shows the theoretically simulated dispersion curves of the ZnO/SiO_2/Si structure. The velocity of Love waves varies between the acoustic velocity of the waves in the SiO_2 substrate (5100 m/s) and that in the guiding layer of ZnO (4814.4 m/s). Two modes of the love waves are generated, with the second mode being generated for larger guiding layer thickness. At very small thickness of the guiding layer, the love wave mode is localized in the SiO_2 substrate. As this thickness increases, the love wave slowly transitions into the ZnO guiding layer until the mode is entirely localized in the guiding layer and there is no displacement in the substrate. Further increases in the wave guide layer thickness do not significantly alter wave speed from a value close to the substrate speed.

4.5.2 Experimental Verification of the Dispersion Relationship

ZnO films with thicknesses varying between 136 nm and 1.36 μm were grown and device A was fabricated on each one of them. The phase velocity at each of these guiding layer thicknesses was determined. Fig. 4.12, we see the increasing frequency of operation in device A for decreasing ZnO film thicknesses. The corresponding phase velocities for each guiding layer thickness are calculated ($v = \lambda f$) and plotted in Fig. 4.13. The dotted line in Fig. 4.13 represents the experimentally obtained dispersion curve for the first Love mode wave and is seen to match closely to the theoretically obtained curve for the device. Also the slope of the dispersion curve is seen to be high, which necessitates high accuracy of the thickness of the guiding layer to achieve a specific phase velocity. The experimental evaluation was performed only for the first Love wave mode.

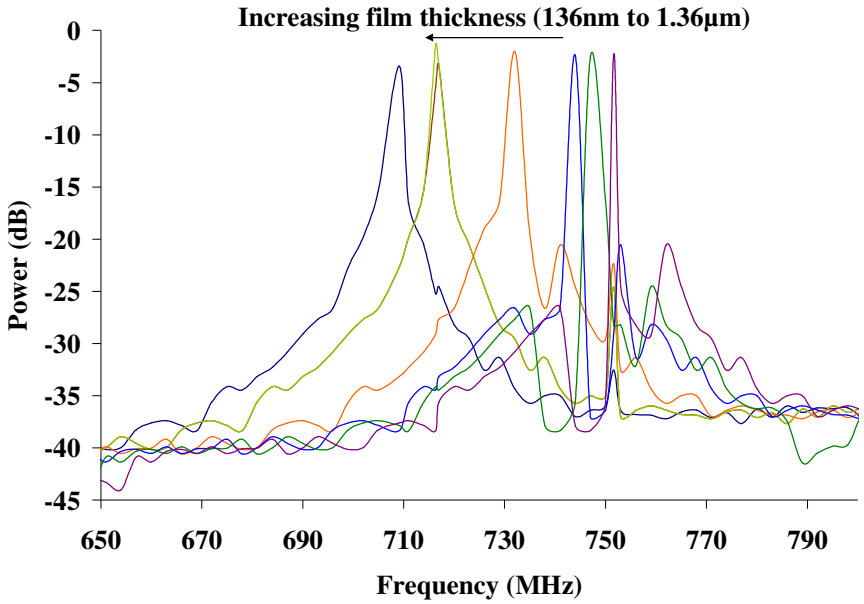

Figure 4.12: Dependence of LM-SAW device frequency on ZnO guiding layer thickness.

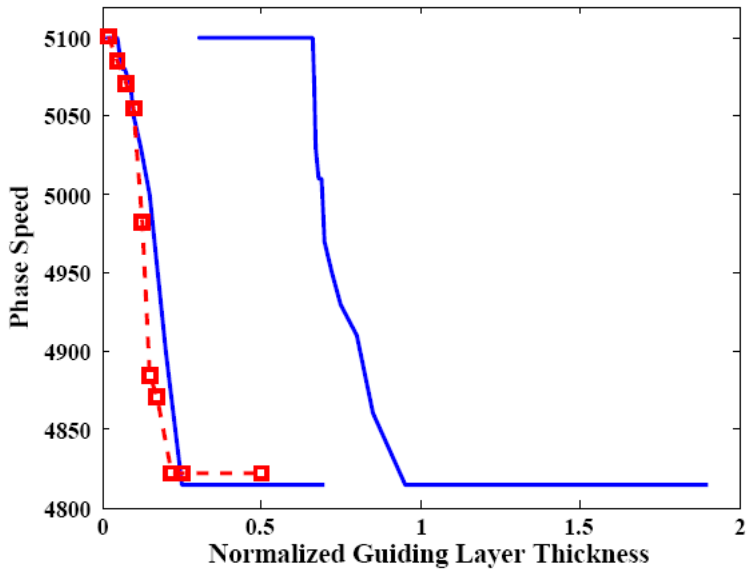

Figure 4.13: Solid lines are the theoretical phase velocity curves as a function of normalized guiding layer thickness ($d/\lambda_l=df/v_l$). The dotted line represents the experimentally verified phase velocities of device A for the first Love wave mode.

The close agreement between the theoretically predicted and experimentally generated phase velocities shows that the surface acoustic waves generated are guided shear horizontal waves or Love mode waves. Thus the ZnO guiding layer on a SiO_2/Si substrate system is suitable for the development of Love mode devices.

4.6 Summary

This chapter describes the design, fabrication and characterization of a Love mode SAW device in the ZnO/SiO_2/Si system. Two sets of devices were developed. Device A was designed to operate in the sub-GHz range (λ=6.8μm) and achieve reduced insertion losses by reducing the metallization ratio from the typical value of 0.5. Device B was designed to achieve a fundamental frequency of operation in the GHz range (λ=3.2 μm). Both the finger width and spacing were maintained at 0.8μm, thus yielding a metallization ratio of 0.5.

The effect of the SiO_2 layer thickness on SAW device performance was studied. The SAW frequency spectrum for a device with a 2000Å thick SiO_2 layer, indicated the presence of two non-harmonically related frequencies, corresponding to two acoustic velocities at 3129.6 m/s and 4864 m/s, respectively. This indicates the presence of two layers of wave propagation in the ZnO film. The higher velocity propagates in the top layer of the ZnO film that has reduced strain and the lower velocity propagates in the ZnO layer adjacent to the SiO_2 interface where the strain is higher. However reducing the SiO_2 layer thickness to 500 Å, results in a substantial reduction in strain to 0.56%, and the generation of a single acoustic velocity of 4814.4 m/s. Since mass sensitivity of an LM-SAW based biosensor depends on acoustic velocities, the alleviation of strain to

obtain a single propagation velocity in the guiding layer is an important factor in device performance.

The dispersion relation for a $ZnO/SiO_2/Si$ Love mode SAW device has been numerically evaluated. The velocity of Love waves varies between the acoustic velocity of the wave in the SiO_2 substrate (5100 m/s) and that in the guiding layer of ZnO (4814.4 m/s). At very small thickness of the guiding layer, the love wave mode is localized in the SiO_2 substrate. As this thickness increases, the love wave slowly transitions into the ZnO guiding layer until the mode is entirely localized in the guiding layer and there is no displacement in the substrate The dispersion relationship was experimentally verified by growing different ZnO guiding layer thicknesses and the theoretical and experimental values were found to match closely. This provides validation that the waves produced in our system are guided shear wave or love waves.

CHAPTER 5： DEVELOPMENT OF LOVE MODE SURFACE ACOUSTIC WAVE MASS TRANSDUCERS

5.1 Background

Investigation of Love-wave devices for mass sensing intensified in the early 1990s as a result of the work undertaken by Gizeli et al. at Cambridge University [168,169]. This work demonstrated the feasibility of using polymer/quartz Love-wave devices as liquid phase mass sensors. Although polymers are suitable candidates for guiding layers due to their low density and low shear velocity, they are also acoustically lossy. With a polymer guiding layer, the acoustic propagation loss increases quickly with increasing layer thickness [170]. To decrease losses, Kovacs et al. introduced a SiO_2 guiding layer on a 90° rotated ST-cut quartz substrate [171,172] instead of a polymer, and Ogilvy [173] and Du et al. [174,175] carried out comprehensive studies on the SiO_2/90° rotated ST-cut quartz structure.

Further research concentrated on improving mass sensing properties by the choice of substrate and guiding layer materials, such as YX $LiTaO_3$[176] and $LiNbO_3$ [177] for substrates and either polymers [178] or metals [179] for guiding layers

5.2 Mass Sensitivity of Acoustic Devices: An Introduction

Mass loading of an acoustic wave device results in lowering the phase velocity of the propagating acoustic wave. Mass sensitivity (S_m) is defined as the change in phase velocity due to the applied mass in the limit that this mass tends to zero.

$$S_m = \lim \frac{(\Delta v)}{(v_0 \Delta m)},\ \Delta m \to 0 \quad \ldots(5.1)$$

where Δm is the added mass, Δv is the change in phase velocity and v_0 is the unperturbed phase velocity. The mass sensitivity is measured from the smallest applied mass that results in a phase velocity shift. In acoustic resonators, where the phase and group velocities are the same, this lowering of the phase velocity can be equivalently obtained as the shift in the resonant frequency and the mass sensitivity can then be defined as

$$S_m = \lim \frac{(\Delta f)}{(f_0 \Delta m)}, \Delta m \to 0 \quad \ldots(5.2)$$

The first quartz crystal sensors were developed by Sauerbrey to measure mass deposited on the crystal surface [10]. The model, which is still widely used, considers the added mass to be simply an extension of the crystal thickness. The resulting shift in the operating frequency was determined as

$$\Delta f = -2 f_0^{\,2} (c\rho)^{1/2} \Delta m / A \quad \ldots (5.3)$$

where Δf is the resonant frequency shift due to the added mass, Δm is the added mass and A is the area of the crystal. This is valid for small amounts of added mass; however the equation over predicts the frequency shift when the added mass gives a frequency shift greater than 2% of the unloaded resonant frequency. Miller and Bolef considered the loaded crystal as a compound resonator which gave Sauerbrey's equation with higher order terms [180]. This extends the model range to frequency shifts up to 15% of the unloaded value. When the quartz crystal resonator is immersed in a fluid, the energy is lost to the fluid through viscous coupling and the frequency shift due to fluid loading was

first modeled by Kanazawa and Gordon [181]. They predicted that the frequency shift was given by

$$\Delta f_n = -f^{3/2}(\rho_1\eta_1 / n\pi\mu_s\rho_s)^{1/2} \ldots (5.4)$$

where f is the fundamental resonant frequency, f_n is the resonant frequency of the nth mode, μ_s is the shear stiffness of the quartz substrate, ρ_s and ρ_l are the densities of the quartz substrate and the loading layer respective and η_l is the viscosity of the loading layer.

Modeling of the thickness shear mode (TSM) response to mass loading layers has developed well beyond the simple Sauerbrey and the Kanazawa and Gordon equations and the frequency and the damping response of a quartz crystal to single or multiple viscoelastic layers which contain the rigid mass and Newtonian liquid limits, can now be calculated [182-184]. However these original equations still provide an important conceptual reference for how solid and liquid properties and changes in operating frequencies influence acoustic wave response. In particular, the $f^{1/2}$ and $f^{3/2}$ mass and liquid loading frequency responses of the TSM indicate that for higher sensitivity, the fundamental frequency should be increased. In TSM resonators, this implies that increasing frequencies requires a reduction in crystal thickness and the crystals then become fragile. This has motivated the development of SAW based mass sensing devices, where the frequency of operation is a function of purely the IDT geometry. In particular, Love wave devices use a shear horizontal polarization and concentrate the acoustic energy in the guiding layer grown on an appropriate substrate, thus offering the opportunity of higher mass sensitivities [185]. In addition, the atomic displacement is in-

plane resulting in minimal insertion losses in liquid environments, and making it a promising device for biosensor applications [186,187].

The theoretical framework for understanding the mass sensitivity of layer guided Love wave sensors has been derived rigorously by McHale et. al. in [166] and is discussed in greater detail in the next section. This analysis showed that the guiding layer thickness affects mass sensitivity of the device through the slope of the dispersion curve and in order to achieve maximum sensitivity, the device should operate in the region where the slope of the dispersion curve is the maximum.

A Love mode sensor consisting of a SiO_2 guiding layer on ST-cut quartz was shown to achieve a maximum mass sensitivity of 14.9 m^2/kg [188]. McHale et. al. showed that for a PMMA layer coated on an ST-cut quartz substrate, the maximum achievable mass sensitivity was two orders of magnitude higher at 1750 m^2/kg.[166].

5.3 Theoretical Formulation and Modeling of Perturbation Theory of Love Wave Devices

When the two-layer Love wave system is perturbed by a mass layer of thickness, *h*, as seen in Fig 4.10., the phase speeds and wave vectors of the substrate and the guiding layer changes. This can be represented as

$$\begin{aligned} T_l^0 &\rightarrow T_l^0 + \Delta T_l \\ T_s^0 &\rightarrow T_s^0 + \Delta T_s \\ \xi^0 &\rightarrow \xi^0 + \Delta\xi \end{aligned} \quad \ldots (5.5)$$

where the subscripts *s* and *l* denote the substrate and guiding layer respectively and *T* represents the corresponding wave vector. The superscript zero indicates the values of the quantities when $\Delta h = 0$ (i.e., solutions of Eq. (4.9)). The left hand side of the three

layered dispersion equation (Eq. (4.8)), can be written as

$$\tan(T_l d) = \frac{\tan(T_l^0 d) + \tan(\Delta T_l d)}{1 - \tanh(T_l^0 d)\tan(\Delta T_l d)} \quad \ldots (5.6)$$

The first term on the right hand side of Eq. (4.8) can be written as

$$\xi_s \tan(T_s w) = (\xi + \Delta\xi)\left[\frac{\tan(T_s^0 w) + \tan(\Delta T_s w)}{1 + \tanh(T_s^0 w)\tan(\Delta T_s w)}\right] \quad \ldots (5.7)$$

and the second term can be written to the first order as $\approx \xi_p^0 T_p^0 \Delta h\left[1 + \xi^0 \tan(T_l^0 d)\tanh(T_s^0 w)\right]$.

The expansion in $\Delta\xi$ can be written in terms of ΔT_l and ΔT_s (with $\xi = \frac{\mu_s T_s}{\mu_l T_l}$) and both these quantities can be related to the change Δv in wave speed, v_0, by using Eq. 4.7. Details of the derivation can be obtained from [166]. Thus Eq. 4.8 can be reduced to the ratio $\Delta v / v_0$. For an infinitesimally small mass perturbation, this is found to be

$$\frac{\Delta v}{v_0} = \frac{1}{\rho_l}\left[\frac{\frac{v^2{}_p}{v^2{}_0}}{\frac{v^2{}_l}{v^2{}_0}}\right]\frac{1}{v_l}\left(\frac{dv}{dx}\right)_{x=d}\Delta h \quad \ldots (5.8)$$

Substituting, Eq. (5.8) in the definition for mass sensitivity (Eq. (5.1)), we get

$$S_m = \frac{1}{\rho_l}\left[\frac{1 - \frac{v^2{}_p}{v^2{}_0}}{1 - \frac{v^2{}_l}{v^2{}_0}}\right]\frac{1}{v_0}\left(\frac{dv}{dx}\right)_{x=d} \quad \ldots (5.9)$$

In a two layered system with an infinitely thick substrate and a wave-guiding layer with finite thickness, the frequency enters the calculation of the wave speed, v0, through the two dimensionless combinations $d/\lambda_l = df/v_l$ and $w/\lambda_s = wf/v_s$. We

introduce the dimensionless quantity $z = d/\lambda_l = df/v_l$, so that a change in the guiding layer thickness, d is equivalent to a change in operating frequency, f. Thus

$$\left(\frac{dv}{dx}\right)_{x=x_0} = \frac{f_0}{v}\left(\frac{dv}{dz}\right)_{z=z_0} \quad \ldots (5.10)$$

The mass sensitivity function then becomes

$$S_m = \frac{1}{\rho_l}\left[\frac{1-\frac{v^2{}_p}{v^2{}_0}}{1-\frac{v^2{}_l}{v^2{}_0}}\right]\frac{f_0}{v_l}\left(\frac{d\log_e v}{dz}\right)_{z=z_0} \quad \ldots(5.11)$$

Thus the mass sensitivity S_m depends on the slope of the dispersion curve ($d\log_e v/dz$), which in turn is a function of the frequency of operation of the device (f_0) and the thickness of the guiding ZnO layer (d). S_m can be maximized by maximizing this slope of the dispersion curve. Another consequence of Eq. (5.11) is that for a given Love mode wave, the peak sensitivity is directly proportional to frequency, provided the slope of the dispersion curve is kept a constant. In order to do this, any frequency increase must be accompanied by a corresponding reduction in the ZnO guiding layer thickness so as to keep the value of z a constant at the appropriate operating point.

The mass sensitivity for the ZnO/SiO_2/Si Love wave system was numerically evaluated using the same parameters as those described in chapter 4. The guiding layer parameters are v_l = 4814 m/s and ρ_l = 5670 kg/m^3 for ZnO. The phase velocity without any perturbation is v_0 (=4814.4 m/s)and v_p is obtained from the numerically evaluated dispersion curve. For the purpose of our simulation, we used device A (operating at 708 MHz) and device B operating at 1.5 GHz, but with the same slope of the dispersion curve as device A.

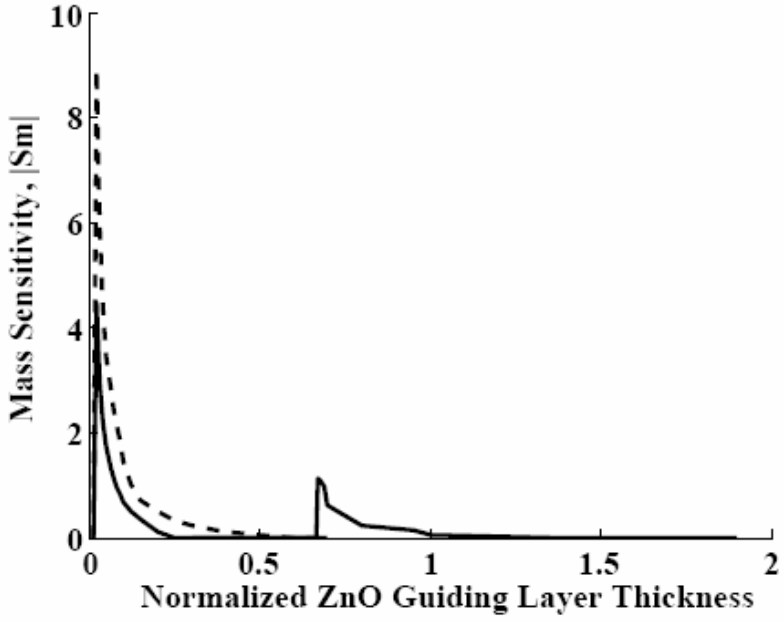

Figure 5.1: Theoretically determined mass Sensitivity, $|S_m|$, in 1/(pg /μm^2) for the first two Love modes shown in Fig 3 (a). The dotted line represents the mass sensitivity of a device operating at 1.5 GHz

Fig 5.1 shows the simulated mass sensitivity curves for device A (solid lines) and device B (dotted line). The maximum slope of the dispersion curve in Fig. 4.11 is obtained for a ZnO thickness of 340 nm or a normalized thickness of 0.05. The corresponding maximum sensitivity in Fig. 5.1, was evaluated to be 4.562 1/(pg/μm^2) for the first mode of operation in device A. This is substantially higher (by a factor of 2.6) than that obtained for a PMMA guiding layer on a quartz substrate (1.750 1/(pg/μm^2)) [166]. The data indicates that this material system provides a sharp transition in the dispersion curve as needed for the targeted high mass sensitivity.

It follows from equation (5.11) that in order to scale the mass sensitivity directly as a function of device frequency, the thickness of the ZnO guiding layer must be reduced, such that the slope of the dispersion curve remains a constant. The maximum mass sensitivity of the device B, but with the same slope as that of device A is 9 ($1/(pg/\mu m^2)$), which scales directly with the device frequency. Thus when this system is used as a sensor, it should be made to operate at the guiding layer thickness where the mass sensitivity is maximized.

Eq. (5.11) defines the mass sensitivity as the fractional change in the phase speed due toe mass deposition. In order to relate this to the fractional change in the frequency of operation of the device, further analysis must be performed. McHale et. al.,[129] have shown that when a shear horizontally polarized SAW device is combined with a guiding layer, in order to slow the wave down and confine it close to the surface, the resulting system generates dispersion in the wave. Consequently, the phase velocity is not equal to the group velocity. They have shown that the fractional change in the frequency can be related to the fractional change in phase speed in a dispersive medium by the ratio of the group velocity (v_g) to the phase velocity (v).

$$\Delta f / f_0 = \left(v_g / v \right) \left(\Delta v / v_0 \right) \quad \ldots (5.12)$$

Furthermore, they show that

$$\frac{v}{v_g} \approx 1 + \rho_l d \mid S_m \mid \quad \ldots (5.13)$$

where ρ_l and d are the density and thickness of the guiding layer respectively. S_m is the mass sensitivity of the system as calculated from Eq. (5.11) as the fractional change in phase velocity. Eq. (5.13) predicts that group velocity will always be less than phase velocity. Using the theoretically evaluated values for S_m, and v_g/v is evaluated and

plotted for both devices A and B (fig. 5.2). Since the phase velocity is always larger than the group velocity, S_m^f will be smaller than S_m, possibly by an order of magnitude

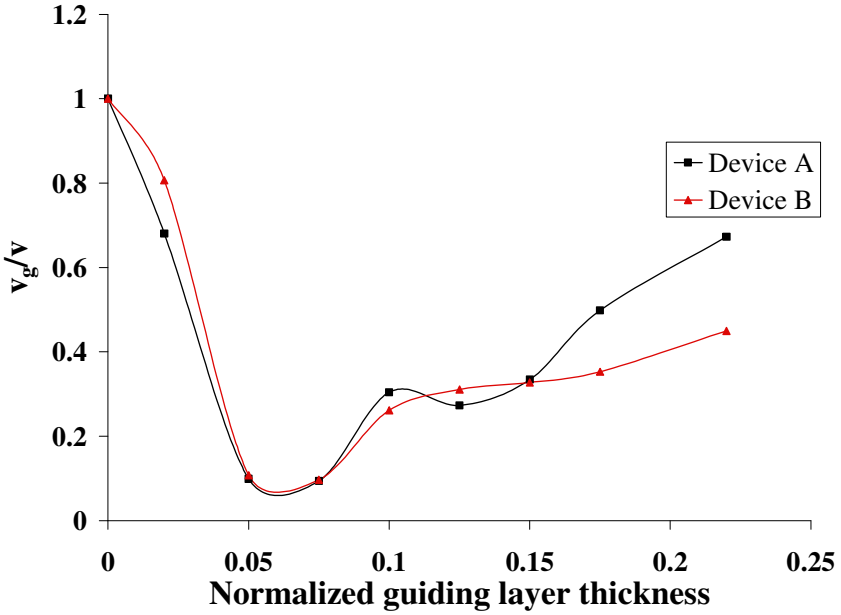

depending on the operating point.

Figure 5.2: The ratio of group to phase velocities evaluated for devices A and B given the mass sensitivities in Fig 5.1

Thus the mass sensitivity when measured as the fractional change in frequency with respect to the original frequency can be evaluated as

$$S_m^f = \lim_{\Delta m \to 0} \frac{1}{\Delta m}\left(\frac{\Delta f}{f_0}\right) = \frac{v_g}{v} S_m \quad \ldots (5.14)$$

This difference between types of mass sensitivity needs to be emphasized, because there is no difference between phase and frequency based mass sensitivity for a quartz crystal microbalance when operated with no coating layer. Therefore, any relative comparison of a QCM to a Love wave device will depend on whether phase velocity or frequency based mass sensitivity is used. The applicability of Eq. (5.14) was confirmed by McHale et. al

[189], using a Love wave device consisting of a polymer on a Lithium Tantalate substrate operating at a frequency of 93 MHz. In this work, we experimentally determine the frequency mass sensitivity (S_m^f)of the ZnO based Love mode device and evaluate the phase velocity based mass sensitivity (S_m) using Eq. 5.14. This is then directly compared this to the theoretically determined value of S_m.

5.4 Experimental Verification of ZnO based LM-SAW mass sensitivity

In order to accurately evaluate the mass loading capability of the sensors, a well-characterized polystyrene-polyacrylic acid diblock copolymer with a density of 1.077 g/cc, was used. For controlled mass loading measurements, square windows were opened in the photoresist between the input and output IDTs using standard photolithography (Fig 5.3). Two windows with sizes 5x5 μm^2 and 20x20 μm^2 were fabricated. After the photoresist was developed and post baked, the copolymer was spin cast on the sample surface and allowed to settle before the photoresist was lifted-off. This resulted in a well-defined window consisting of the copolymer film only.

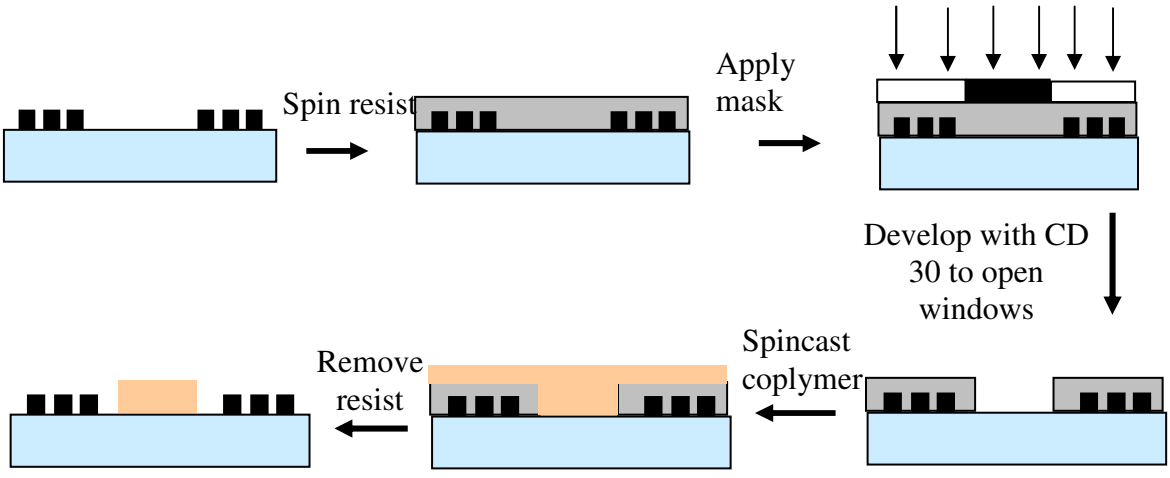

Figure 5.3: Standard lithography was used to open windows between the IDTs for copolymer mass deposition

The mass deposited on each window area was calculated as the product of the window area, the height of the copolymer measured by a Tencor Instruments Alpha-Step 500 profilometer, and the known density of the deposited copolymer. The thickness of the copolymer can be controlled by varying the spin casting speed during deposition. In the present work the spin casting speed was varied between 350 and 750 rpm. As seen in Fig. 5.4, this resulted in copolymer thicknesses between 5 μm and 0.5 μm, respectively.

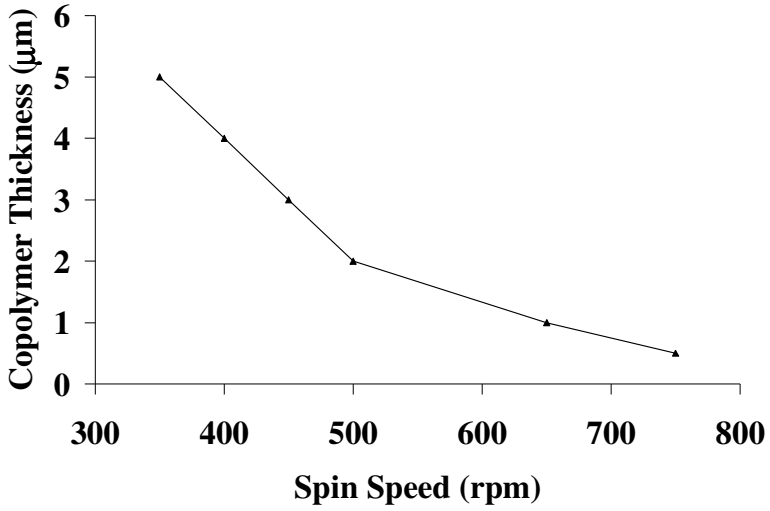

Figure 5.4: Copolymer thickness as a function of the spin casting speed

In order to experimentally verify the mass sensitivity achieved in this ZnO based LM-SAW system, we deposited the copolymer in the windows and measured the frequency shift in the SAW device. The mass of the copolymer deposited in the smaller sized windows was 53.85 fg, while in the larger sized windows was 0.861 pg. The frequency spectrum of devices A and B were measured with and without mass loading. With mass loading the propagating velocity of the Love wave and thus the measured

frequency of the LM-SAW device is reduced. The frequency shift (Δf) is defined as the frequency of the Love mode device without mass loading minus that with mass loading.

Mass sensitivity (S_m^f) was first evaluated as the frequency shift per MHz per unit area of applied mass. Then the mass sensitivity as a fractional change in phase velocity was evaluated from Eq. 5.24 as $S_m = \frac{v}{v_g} S_m^f$. This can now be directly compared to the theoretical obtained values for mass sensitivity.

As seen in Fig. 5.5(a), the measured mass sensitivity for both devices closely matches the theoretically estimated values. Maximum sensitivity in device A is achieved for a normalized thickness of the ZnO film of 0.05, corresponding to a 340nm thick ZnO film. Thus, for this thickness of the guiding layer, we achieve maximum shift of frequency due to the applied mass, in the LM-SAW device. The mass sensitivity measured for applied masses of 53.85 fg, and 0.861 pg, is 4.162 and 4.456 1/(pg/μm^2), respectively. These values of sensitivity are matched to within 6.5% of each other.

For device B (Fig 5.5 (b)), the thickness of the guiding layer was reduced to achieve the same slope in the dispersion curve as in device A. The maximum sensitivity in device B is obtained for a 160 nm thick ZnO guiding layer as compared to 340 nm in device A. In this case, for applied masses of 53.85 fg, and 0.861 pg, the maximum measured sensitivity is 8.687 and 8.599 1/(pg/μm^2) respectively. Fig. 5.5 also indicates that experimental values for mass sensitivity sometimes exceed the theoretical values. This may happen when the applied mass is not as well-confined within the window boundaries and, hence the experimentally evaluated mass exceeds the estimated mass applied in the theoretical simulations.

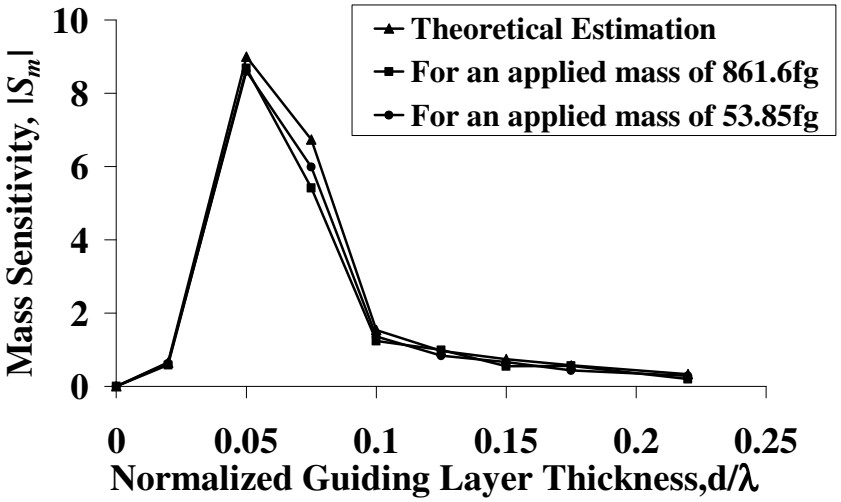

(a)

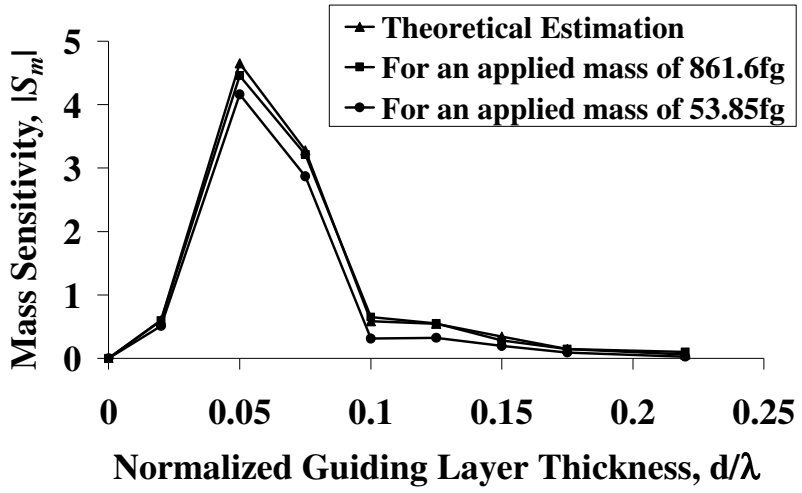

(b)

Figure 5.5: Mass Sensitivity measurements for devices A and B in $1/(pg/\mu m^2)$ for an applied polymer mass of 53.85fg and 0.861pg. (a) Device A achieves a maximum sensitivity of 4.283 while (b) device B achieves a maximum sensitivity of 8.89**.**

.For biosensing experiments, it is highly desirable to use the most sensitive

geometry for each device. Devices A and B were therefore developed on ZnO films that generated the maximum sensitivity (340 nm and 150 nm for devices A and B respectively), and the frequency shift was observed as a function of increasing applied mass. Fig. 5.6 shows that device B, having almost twice the sensitivity of device A, generates a larger frequency shift for the same applied mass.

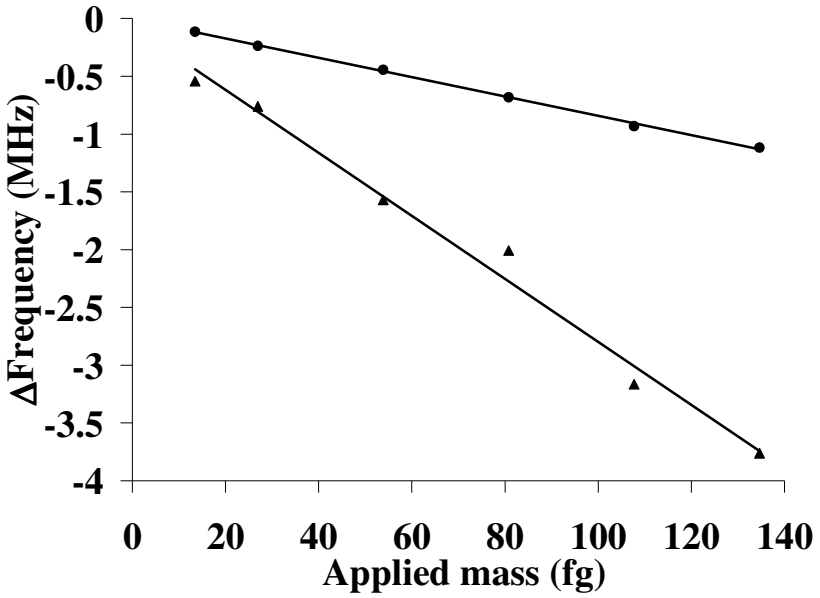

Figure 5.6: Frequency change for device A and B as a function of applied mass on a **5x5** μ^2m area for a constant guiding layer thickness. The thickness of ZnO guiding layer is 340 nm for device A and 160nm for device B.

5.5 Summary

This chapter describes the calibration of LM-SAW device as a mass sensor. The numerical modeling of the mass perturbation of the ZnO/SiO_2/Si Love wave Device is carried out.

Numerical evaluation of the mass sensitivity of this system and its experimental

verification was carried out. Windows of different sizes were opened in the space between the IDTs and different copolymer masses were deposited. The frequency shift as a result of the applied masses was determined and the mass sensitivity curve was thus experimentally established.

Mass sensitivity is known to be a function of the frequency of operation of the device as well as slope of its dispersion curve. In order to maximize the mass sensitivity, the slope of the guiding layer can be maximized by optimizing the guiding layer thickness. For device A, the optimized guiding layer thickness was found to 340 nm, yielding an operating frequency of 747.7 MHz and for device B, this was 160 nm, yielding an operating frequency of 1.586 GHz. Corresponding to these guiding layer thicknesses, the maximum mass sensitivity measured for an applied masses of 53.85 fg, was 4.162 ($1/pg/\mu m^2$) and 8.687 ($1/pg/\mu m^2$) respectively for devices A and B respectively.

Other guided shear SAW devices have been recently reported in literature on different guiding layer/substrate structures with mass sensitivities varying from 0.01 to 14.2 ($\mu m^2/pg$). McHale et. al. [166] reported a SiO_2/quartz device operating at 100 MHz with a mass sensitivity of 0.014 ($\mu m^2/pg$). A AlN/Al_2O_3 shear SAW biosensor to detect rabbit immunoglobin, operating at 350 MHz was also reported to have a similar mass sensitivity of 0.01 ($\mu m^2/pg$) [190]. However these devices exhibit very low mass sensitivities and both SiO_2 and AlN have low surface reactivities. ZnO on quartz substrates was reported to operate at 150 MHz with a mass sensitivity of 0.8 ($\mu m^2/pg$) [191]. Our prototype sensor is developed on a structure grown directly on SiO_2/Si for CMOS compatibility and demonstrated a substantially higher frequency of operation and

sensitivity as compared with the above reported sensors. The sensitivity of our sensor is comparable only to one other reported sensor, which uses PMMA on $LiTaO_3$. However PMMA exhibits as poor chemical and temperature resistance as well as poor surface reactivity[192].

Thus the $ZnO/SiO_2/Si$ system with its high surface reactivity and high frequency of operation is highly suited to develop biosensors with high mass sensitivities.

CHAPTER 6 : A ZnO/SiO_2/Si IL-6 BIOSENSOR PROTOTYPE

6.1 Introduction

In this chapter, we describe the development of the IL-6 biosensor prototype. The procedure for IL-6 immobilization on the ZnO films in the window area of the SAW device is developed and specificity of IL-6 binding is studied through the immobilization of the IL-6 monoclonal antibody. The morphological and binding properties of the proteins at each stage are observed using scanning electron microscopy (SEM). The frequency shift of the sensor upon application of the proteins at each step of the immobilization procedure is measured in order to accurately measure the IL-6 mass. Finally, the sensor is tested in human serum.

6.2 Protein immobilization procedure on the ZnO sensor surface

Immobilization of IL-6 onto the ZnO films through BSA was achieved through a five step process as we have previously discussed in chapter 2 [193]. This involved the hydroxylation of the ZnO surface with ultra pure water, followed by silanization with 3-Aminopropyltriethoxysilane (ATES). ATES was used as the bridge to which gluteraldehyde was bound. This surface modification allowed the bovine serum albumin (BSA) to covalently bind to gluteraldehyde, and the IL-6 to electrostatically bind onto BSA.

The silanization process of ZnO films was done with 3-Aminopropyltriethoxysilane (ATES 99%, Aldrich) solution: (95% aqueous solution of ethanol= 4:100 by volume) at room temperature for 4 to 5 hours. The alkylamininosilane-derivatized surface was thus formed. In order to salinize the exposed ZnO surface in the

windows of the LM-SAW devices, the samples could not directly be placed in the ATES solution. This is because ATES is highly alkaline and attacks the film of photoresist thus dismantling the patterned windows. Vapor priming of the ATES solution has been used to successfully overcome this problem [194]. The devices were then rinsed by sonication in ethanol for 1 to 2 minutes, washed in ultra pure water and baked at 110 ^{o}C for 10 to15 min.

The silanized samples were immersed in a 2ml of 2% gluteraldehyde solution (Grade I, 70% Sigma) in 10 mM sodium phosphate-buffered saline (PBS) at pH 7.4, and shaken for 12 hours at 4^{o}C. The samples were then washed thoroughly in ultra pure water to remove the excess gluteraldehyde, and then dried in N_2 gas, before inserting in the SEM for visualization.

The aldehyde activated surfaces were used for covalent attachment of the bovine serum albumin (BSA-Sigma Aldrich). The BSA concentration was adjusted to 0.1mg/ml with 10 mM PBS, and 1 to 2ml of BSA in PBS solution was incubated for 12 to 18h at 4^{o}C in a shaker. The samples were rinsed three times in 10mM of PBS, rinsed in ultra pure water, and dried in N_2 gas. IL-6 [rhL-6 recombinant human-*E. coli* derived-10µg, R&D System, Minneapolis MN, 55413] proteins were bound electrostatically to BSA. Different concentrations of IL-6 (100pg/ml to 2µg/ml) were diluted in a 0.1mg/ml BSA solution in 10 mM PBS, and 10 to 15µl were spotted on the samples and kept for 12 to 18h at 4^{o}C. The morphological evaluation and ELISA analysis of the above binding procedure was previously discussed in chapter 3. With IL-6 now bound onto the LM-SAW devices, the mass of the bound protein was quantified by the resonant frequency shift of the device.

In order to ensure specificity of the IL-6 binding through the IL-6 antibody, the gluteraldehyde activated surfaces were also used for covalent attachment to the monoclonal anti-human IL-6 antibody [Monoclonal recombinant human-*E. coli* derived IL-6 antibody-500µg, R&D System, Minneapolis MN, 55413]. The attachment of the IL-6 protein to the antibody is covalent in nature. The antibody concentration of 1µg/ml was diluted in 10 mM PBS and kept for upto 24h at 4^oC. The samples were then rinsed three times in 10mM of PBS, rinsed in ultra pure water, and dried in N_2 gas. Different concentrations of IL-6 (20ng/ml to 2µg/ml) were diluted in a 0.1mg/ml BSA solution in 10 mM PBS, and the samples were incubated in them in a shaker for 24h at 4^oC.

To evaluate the morphology of the IL-6 antibody and the IL-6 protein without the influence of ATES and gluteraldehyde, IL-6 antibody was directly adsorbed onto the ZnO surface and then IL-6 was bound to the antibody. The samples were first placed in a solution of 1µg/ml of antibody for 6h at 4^0C. Different concentrations of IL-6 (200ng/ml to 2µg/ml) were diluted in a 0.1mg/ml BSA solution in 10 mM PBS, and the samples were incubated in this solution for 2h at 4^oC.

Finally, our devices were used to detect the quantity of IL-6 in normal human serum (Innovative Research, Southfield, MI, 48034). Two types of serum were used in our analysis. Serum A consisted of pooled human serum from multiple donors below the age of 55 (IPLA-SER1) and serum B consisted of normal human serum from a single female donor over 55 years of age (IPLA-SER6). A 250µl assay dilutent consisting of a buffered protein base with preservative is first added to each sample. (RD1D assay dilutent-6ml, R&D System, Minneapolis MN, 55413). This enhances the binding of IL-6 in the human serum to the sample, while inhibiting the attachment of other proteins

present in human serum. The samples are incubated for up to 3 days at room temperature in 1ml of the serum. The samples were then washed 4 times with 2ml of PBS with a 2-3 minute soak time provided in the PBS solution between each of the washes.

6. 3. Morphological Studies of IL-6 Binding

Once the LM-SAW devices are fabricated with the window openings, the exposed ZnO surface in the windows were inspected in the SEM prior to any immobilization treatment. The surfaces were found to be morphologically featureless and clean. Fig. 6.1 shows the optical image of the LM-SAW device with a window opened between the input and output IDTs. The morphology of IL-6 particles when bound onto ZnO thin films, through BSA was previously discussed in chapter 3. In this chapter, we investigate the morphology of IL-6 binding through the IL-6 antibody on the ZnO films.

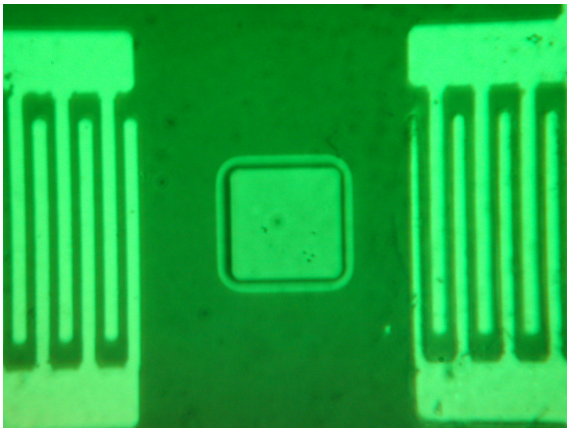

Figure 6.1: Optical Image of the window opening between the input and output IDTs of the SAW device. The ZnO surface in this region is exposed, while the remaining area is coated with 1813 Shipley positive resist. Protein immobilization is performed in this window.

6.3.1 IL-6 attachment through antibody adsorption

We first adsorbed the IL-6 antibody directly onto the ZnO surface and inspected it in the SEM. This study was performed to establish the morphology of the antibody and IL-6, when directly bound to the ZnO surface. Fig 6.2(a). shows the SEM image of the IL-6 antibody bound onto the ZnO surface. The IL-6 antibodies assume a distinctly spherical shape with a lateral size distribution ranging between 0.5 and 3μm. The antibody spheres show a brighter perimeter and a darker interior. When the IL-6 protein is applied, it binds with the antibody creating a cluster of spheres, as seen in fig 6.2 (b). The lateral dimension of this cluster extends to approximately 6μm. The IL-6 protein is also composed of circles with a darker interior surrounded by a bright rim. The single spherical particles seen in Fig. 6.2(b) could either be an antibody or an unattached IL-6 protein directly adsorbed onto ZnO.

6.3.2 IL-6 immobilization through covalent attachment of IL-6 antibody

Next, the IL-6 proteins were covalently bound onto ZnO separately through BSA as well as the IL-6 antibody. During the immobilization process, the terminal aldehyde group in gluteraldehyde binds to the amine group of the BSA or the IL-6 antibody. This method avoids non-specific attachment of the protein directly to the solid phase [140]. However binding the IL-6 protein onto BSA is electrostatic in nature, while binding the IL-6 onto its antibody is covalent in nature. Thus the latter is more stable, controllable and specific.

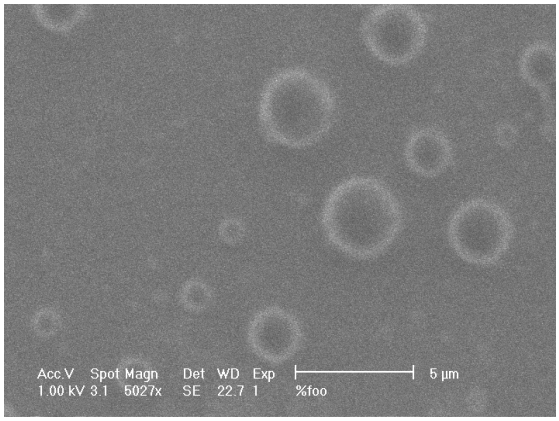

(a)

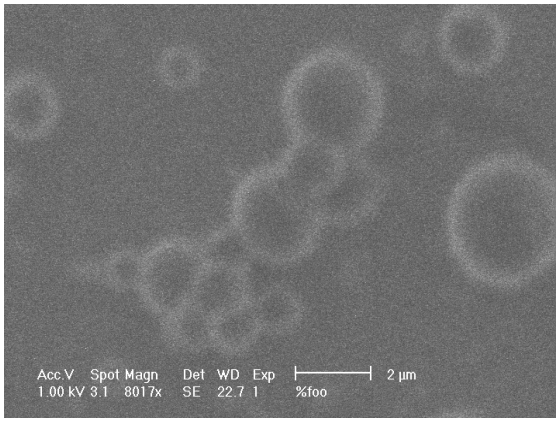

(b)

Figure 6.2: SEM images taken during protein immobilization (a) SEM image upon application of the IL-6 antibody indicates a spherical particles of the antibody (b) The SEM image upon application of IL-6 onto the antibody indicates further clustering of IL-6 close to the antibody .

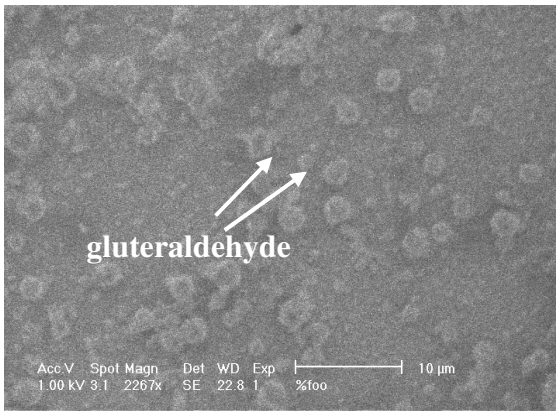

(a)

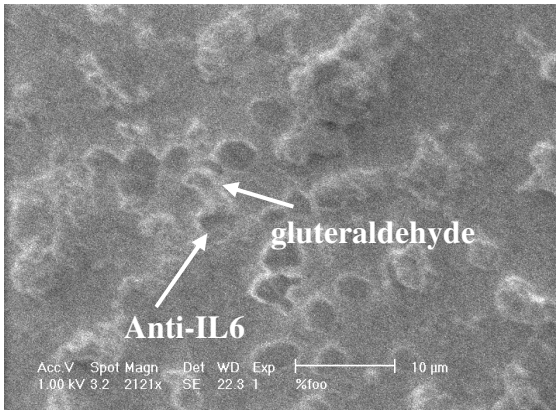

(b)

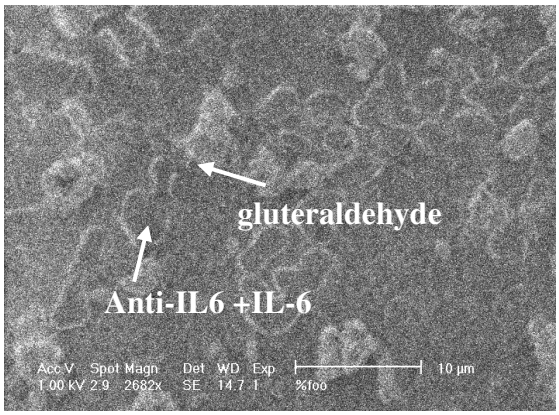

(c)

Figure 6.3: SEM images taken during protein immobilization(a) SEM image upon application of ATES+ gluteraldehyde indicates coagulated particles of ATES and gluteraldehyde. (b) SEM image upon application of the IL-6 antibody indicates a cluster of the antibody that is attached to gluteraldehyde (c) The SEM image upon application of IL-6 onto the antibody indicates further clustering of IL-6 close to the antibody .

Fig. 6.3 shows the SEM images taken during the IL-6 immobilization process through the IL-6 antibody onto the exposed ZnO surface in the window area. Fig 6.3(a) shows the SEM image after gluteraldehyde is bound onto ATES. Typical lateral size distribution of these coagulated particles is 1 to 4μm as shown in the image, and it is found to be consistent throughout the window from larger area surveys of the ZnO surface.

Fig. 6.3(b) shows the SEM image when IL-6 antibody is bound covalently onto gluteraldehyde. The lighter areas in the SEM image represent gluteraldehyde, while the antibody consists of particles with a bright rim encircling a darker interior. The antibody is made up of distinct spherical particles that tend to arrange themselves around gluteraldehyde. The lateral size distribution of the antibody is typically between 2 and 5μm. This morphology is consistent with that of the antibody when it is directly adsorbed onto the ZnO thin films (Fig 6.2(a)).

Fig. 6.3(c) shows the SEM image of the exposed ZnO film in the windows, after the application of IL-6 onto the antibody. IL-6 binds covalently onto the antibody generating cluster formations. As seen in the figure, the IL-6 protein seems to merge into the antibody creating the cluster. The IL-6 morphology is also somewhat spherical, with a brighter rim surrounding a darker interior. This is consistent with the image of IL-6 seen in fig. 6.2(b).

Once the IL-6 binding is complete, the photoresist is taken off with acetone and the sample is rinsed thoroughly in ultra-pure water. The samples are then dried with N_2 gas before determining the frequency response.

6.4 Frequency Response and Mass measurements

The frequency response of the SAW devices was first measured before the protein immobilization process. The devices were developed on films with a ZnO thickness of 340nm for device A and 160nm for device B. The resonant frequency obtained (denoted as f_0) from each device type was measured to be 747.7 MHz for device A and 1.586 GHz for device B.

6.4.1 IL-6 attachment through the antibody adsorption

First, the IL-6 antibody was adsorbed directly onto an exposed window of size 5x5 μm^2 for both devices. The resonant frequency of operation in devices A and B was measured (f_1) after antibody adsorption. The average frequency shift (f_0- f_1) was measured to be 6.7 KHz and 21.55 KHz for devices A and B respectively. Different quantities of the IL-6 protein (200ng/ml to 2µg/ml) were then applied and the frequency was measured (f_2) again.

Figure 6.4(a) shows the frequency shift (f_0- f_2) generated after the application of the IL-6 protein onto a 5x5 μm^2 window area of devices A and B. The frequency shift observed when the applied IL-6 concentration is less than 500ng/ml is the same as when there is no IL-6 applied. i.e. $f_2 = f_1$. In other words, the frequency shift after IL-6 is adsorbed is measurable only when the applied IL-6 concentration exceeds 500 ng/ml. This indicates that adsorption is not an efficient mechanism for protein binding.

Mass sensitivity of the device is calculated as the frequency shift of the device per unit area of applied mass. The mass sensitivity of the device was experimentally evaluated in chapter 5. For device A, it was evaluated to be 4.162 and 4.456 ($1/pg/\mu m^2$) in a 5x5 μm^2 and 20x20 μm^2 area respectively. For device B, this was evaluated to be

8.687 and 8.559 (1/pg/μm^2) in the 5x5 μm^2 and 20x20 μm^2 area respectively. By measuring the frequency shift upon protein deposition, the mass deposited in the window can therefore be determined.

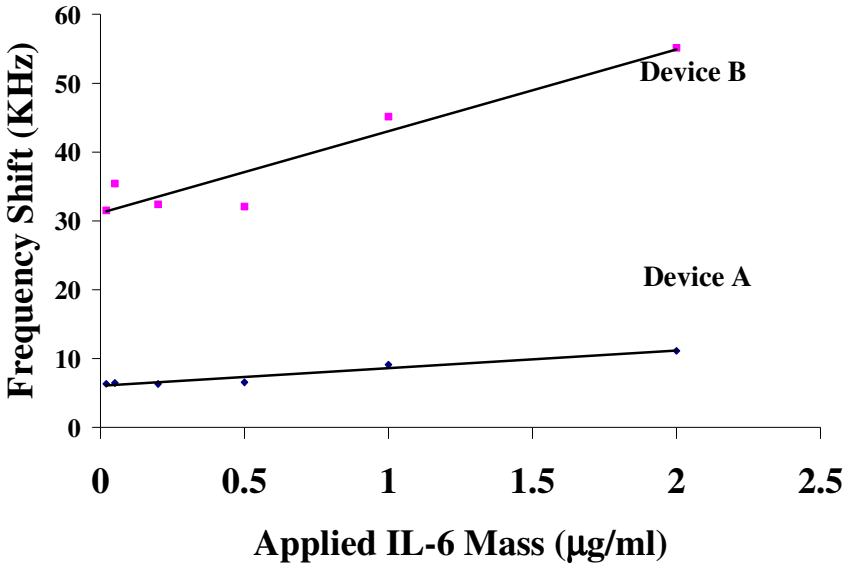

(a)

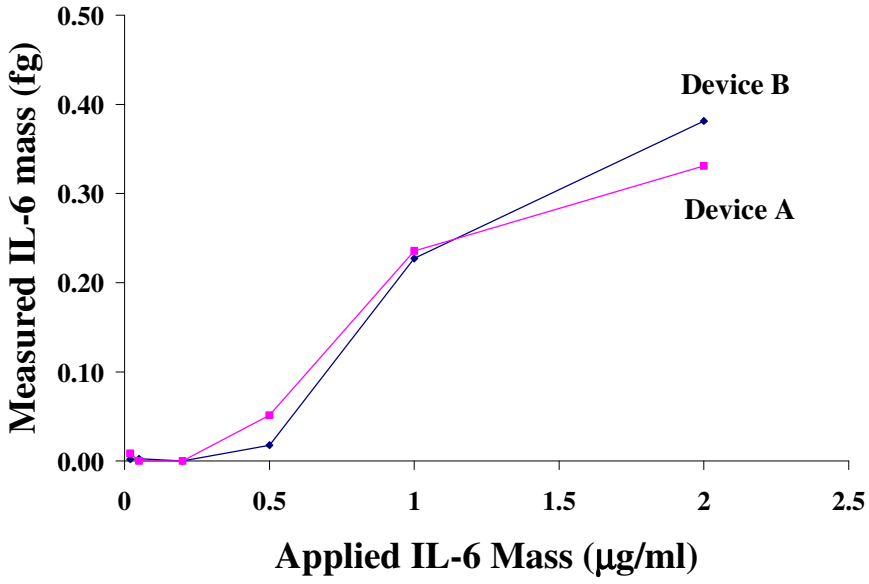

(b)

Figure 6.4: (a) Frequency shift vs adsorbed (antibody + IL-6) mass on the ZnO/SiO_2/Si guided shear acoustic wave sensor for devices A and B in a 5x5 μm^2 window (b) Measured vs adsorbed IL-6 mass on the sensor for devices A and B in a 5x5 μm^2 window

Fig. 6.4(b) indicates the quantity of antibody plus IL-6 mass adsorbed onto the exposed window area. The amount of mass adsorbed is not measurable for applied IL-6 masses less than 500 ng/ml. A maximum of 0.4 fg of mass was measured for an applied IL-6 mass of 2 μg/ml.

6.4.2 IL-6 immobilization through BSA

Following the adsorption experiments, the IL-6 protein was then immobilized in the window through BSA, as described in section 6.2 and the frequency spectra of the sensors were obtained. The frequency was measured after the application of ATES, gluteraldehyde, and BSA (f_3). This mass can be obtained from the frequency shift, $f_0 - f_3$. Then different amounts of IL-6 (20 ng/ml - 2μg/ml) were applied and the frequency of the sensors was measured (f_4). To evaluate the IL-6 mass deposited, we measured the frequency shift after IL-6 immobilization minus the frequency shift after the BSA deposition ($f_3 - f_4$). Fig. 6.5 indicates the IL-6 mass deposited as a function of the IL-6 mass applied.

6.4.3 IL-6 Immobilization through the IL-6 antibody

As described in section 6.2, for the specific binding of the IL-6 protein, the IL-6 antibody was bound to gluteraldehyde, and the frequency spectra of the sensors were measured after the application of ATES, gluteraldehyde, and the IL-6 antibody (f_5). Then different amounts of IL-6 (20 ng/ml - 2μg/ml) were applied in both windows and the frequency of operation of the devices was measured (f_6). The mass of IL-6 can then be determined from the difference in the frequency shift after application of the antibody and that after application of the IL-6 protein ($f_5 - f_6$). Fig. 6.6 shows the mass deposited on

devices A and B for both windows. From Figs. 6.5 and 6.6, it is seen that the maximum IL-6 mass deposited through BSA is less than that through the antibody due to the electrostatic nature of IL-6 to BSA binding as opposed to the covalent nature of IL-6 to antibody binding. As observed in the Fig. 6.6, the measured IL-6 mass has a linear relationship with the applied IL-6 mass. This is an important property of the biosensor, which has a wide and linear range of detection.

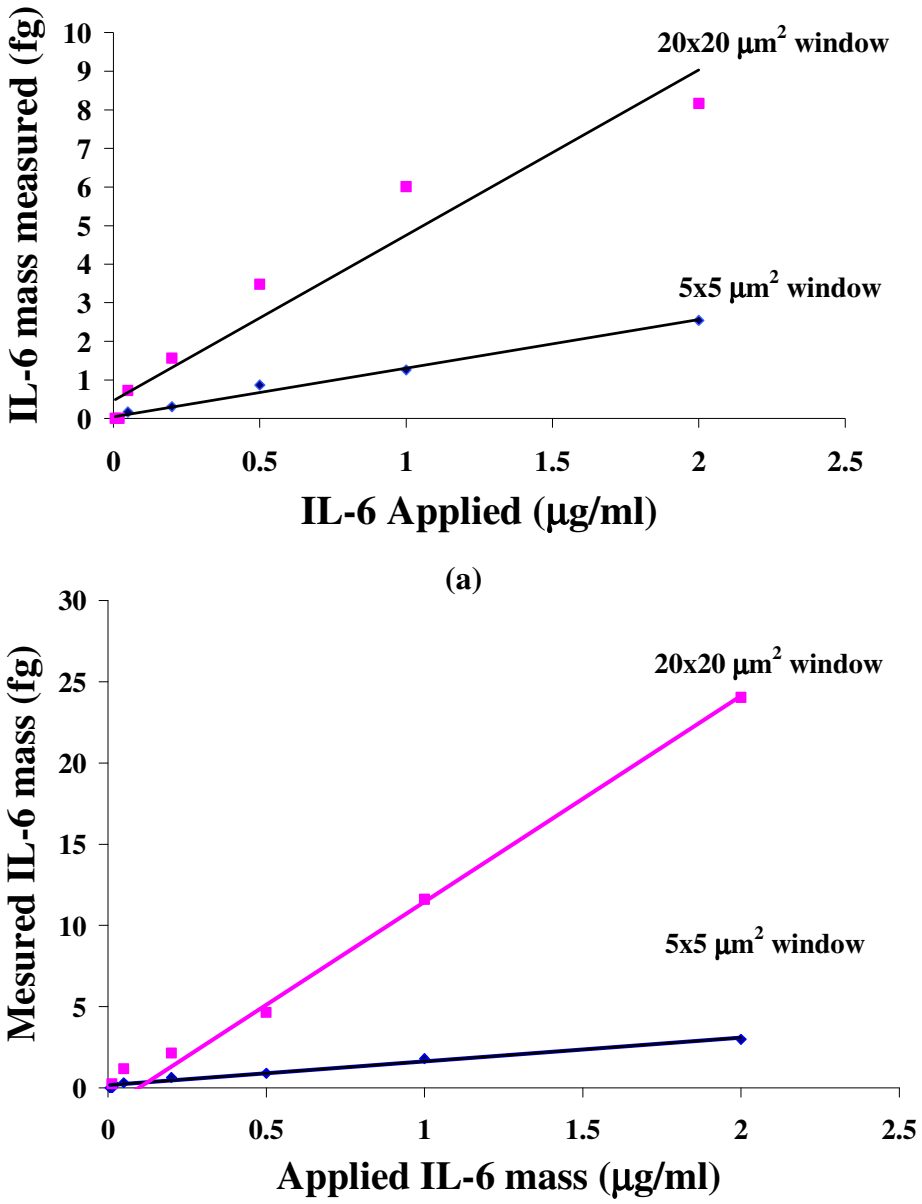

Figure 6.5: Measured vs applied IL-6 mass through BSA binding on the $ZnO/SiO_2/Si$ SAW sensor in 5x5 μm^2 and 20x20 μm^2 windows for (**a**) Device A operating with a center frequency of 747.7 MHz (**b**) Device B operating with a center frequency of 1.586 GHz

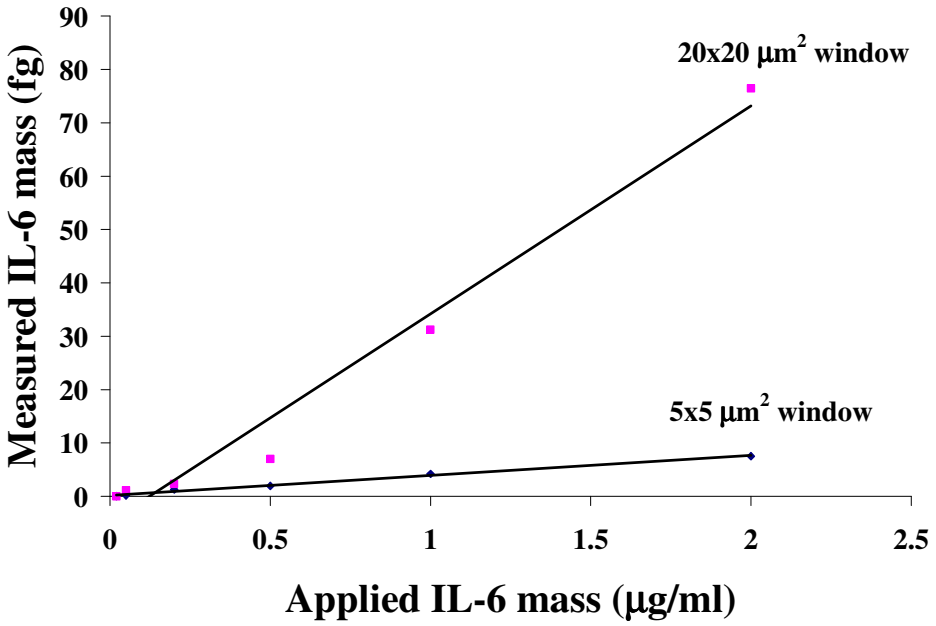

(a)

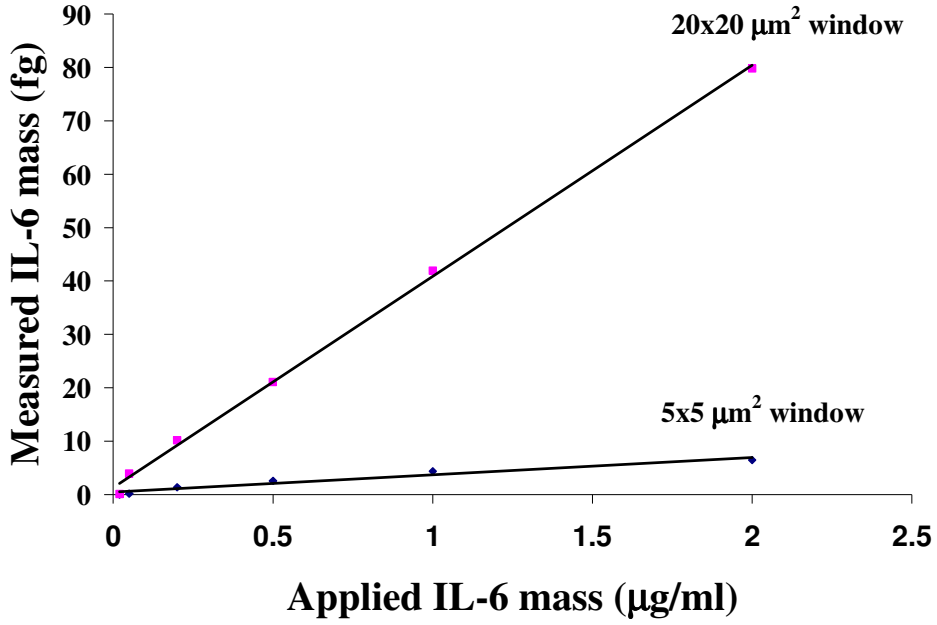

(b)

Figure 6.6: Measured vs applied IL-6 mass through IL-6 antibody binding on the $ZnO/SiO_2/Si$ SAW sensor in 5x5 μm^2 and 20x20 μm^2 windows for (**a**) Device A operating with a center frequency of 747.7 MHz (**b**) Device B operating with a center frequency of 1.586 GHz

6.5 IL-6 Detection in Human Serum

Finally the biosensor functionalized with the monoclonal IL-6 antibody was used to detect the presence of IL-6 in human serum. The biosensor consisted of device A with a 20x20 μm^2 window. Human serum A, which consists of pooled human serum from multiple donors under the age of 55, was first applied onto the biosensor and incubated for 3 days. Repeated measurements of the frequency yielded results within 4.5% of each other and the average mass of IL-6 measured was 2.27 fg. Serum B, which is from a single female donor, whose age is above 55, yielded a higher average mass measurement of 6.81 fg. Thus the mass measured in serum B is approximately three times higher in serum B. This is understood to be the result of age related increased IL-6 levels.

To confirm increased IL-6 levels in human serum B, an independent ELISA measurement was performed with a Quantikine High Sensitivity Human IL-6 Immunoassay kit (performed by Machaon Diagnostics, Inc., Oakland, CA, 94609). The ELISA results were done in duplicate using the high precision kit. Serum A was measured to be at 6 and 10 pg/ml of IL-6 in the two measurements, and fell within the linear range of calibration of the ELISA kit. Serum B was measured in duplicate also, and found to have IL-6 concentrations that fell outside the linear range of calibration of the ELISA kit. Hence, the kit provided only minimum IL-6 values per measurement for this serum, which were >10 and >25 pg/ml of IL-6. In order to get a more accurate reading by ELISA, a second kit needs to be calibrated for the above predicted range and used for the measurement, which makes it expensive, elaborate, and impractical for real-time measurements. It does however; show a higher level of IL-6 in serum B, in agreement

with our sensor. Thus our biosensor can effectively measure trace amounts of IL-6 present in the human serum, directly.

6.6 Summary

This chapter describes the development of the $ZnO/SiO_2/Si$ based SAW device as a biosensor for detection of IL-6 proteins. The immobilization technique for IL-6 through the IL-6 antibody onto the device was developed and its morphology was studied using the SEM technique.

A technique to bind the IL-6 (through BSA as well as the IL-6 antibody) in the window opened between the IDT fingers was developed. A key feature of the technique is to use vapor priming to bind the ATES onto the exposed ZnO film. Once the IL-6 was bound, the frequency shift due to the protein mass binding was measured. Since the mass sensitivity of the sensor has been previously calibrated, the mass of the applied protein could now be determined.

The measured mass of IL-6 scales almost linearly with the applied IL-6 mass and the minimum measurable mass of the bound protein was approximately 1.4 fg in device A and 4 fg in device B. Also, the mass of IL-6 deposited through BSA and the IL-6 antibody are comparable.

Finally, the biosensor was used to detect the presence of IL-6 in normal human serum. For normal human serum for pooled donors below the age of 55 (serum A), the quantity of IL-6 measured was 2 fg as compared to normal human serum from a single female donor above the age of 55 (serum B), where the IL-6 quantity was ~ 7fg. This could be the result of age resulted chronic illnesses that lead to increased IL-6 production in the blood. The increased IL-6 levels in the human serum B were confirmed with

ELISA. We have therefore developed a highly sensitive biosensor capable of detecting a few femtograms of protein mass.

CHAPTER 7 : CONCLUSIONS

7.1 Summary

This thesis presents the design and development of a ZnO/SiO_2/Si Love mode SAW biosensor for the detection of the IL-6 protein in trace amounts for the first time. The research includes the growth and characterization (structural and optical) of the ZnO films, the development of an effective immobilization technique for the binding of the IL-6 protein onto the ZnO film surface, and the design and fabrication of a Love mode ZnO/SiO_2/Si SAW biosensor for Interleukin-6. As the selective identification of the chemical constituents of biological systems becomes increasingly important for biomedical diagnosis, detection of these constituents in trace levels becomes important for advanced biosensor applications. Thus the results in this thesis will impact effective and reliable operation of biosensors

In this thesis, the challenging growth of ZnO thin films on Si and SiO_2/Si substrates was achieved and high quality, c-axis oriented films suitable for our SAW device structure, were obtained as shown by the structural and optical characterization of the films. Furthermore, electrical characterization of the films on Si substrates revealed that we can achieve control over the p or n-type conductivity of the films, by controlling the growth parameters of the films, and undoped p-type ZnO films were demonstrated, for the first time in pulsed laser deposition. The study of the effect of SiO_2 thickness on ZnO film quality revealed that a 50 nm thick SiO_2 layer was the optimum thickness for film quality (minimum strain) and effective wave propagation.

The immobilization of the IL-6 protein was achieved through BSA on the ZnO surface, and the morphology of the bound bio-molecules was evaluated at each step for the first time. Measurements of the bio-materials on the surface using a modified solid phase ELISA, showed that ZnO offers a much better surface for protein binding, yielding up to ten times more IL-6 bound on ZnO than SiO_2.

The SAW device design, fabrication and characterization resulted in devices operating at resonant frequencies of 708 MHz and 1.5 GHz. The acoustic velocity of the waves was consistently measured to be 4814.4 m/s. The velocity dispersion curve of the system was modeled and experimentally verified for this system. Furthermore, the measurement result indicates that the SAW waves produced were guided shear waves or Love mode waves. This was a significant result in the development of the sensors as it allowed the sensors to be used without the attenuation of the waves in liquid media.

The model for mass sensitivity of the ZnO/SiO_2/Si Love mode sensor provided an optimum ZnO thickness for effective wave guiding. It is shown that the device achieved maximum mass sensitivity at the optimum ZnO thickness where the energy sharing between the ZnO and SiO_2 layers is maximum. The experimental evaluation of the mass sensitivities was achieved by applying a well-characterized copolymer mass. These experimental mass sensitivities were compared with the theoretical ones and found to be in excellent agreement.

For increased specificity the IL-6 immobilization technique was developed for direct binding through the monoclonal antibody on the window areas on the SAW devices, and the morphology at each step was evaluated. The frequency shift generated

due to the bound protein was measured and the mass of applied protein was calculated. A prototype biosensor was used to successfully detect IL-6 in human serum.

The thesis provides important parameters for the design, fabrication, and characterization of the biosensor for protein sensing. The presented device design and experimental techniques are suitable for measurement in a wide range of applied protein mass and can be used for detection both in air and liquid environments.

7.2 Future Work

The current study focused on the development of device quality thin films in Love mode SAW devices for biosensing applications. The development of both conductivity types (p and n) ZnO films opens up the development of ZnO p-n junctions necessary for UV laser applications and gas sensors.

Furthermore, the development of binding techniques for other proteins, DNA, as well as enzymes, and other biological elements, is a natural extension of this thesis. Optimization of incubation times in each step of the immobilization will promote better binding of the protein providing for improved sensor performance.

The SAW devices can be further improved by optimizing the distance between the IDTs to improve quality factor of the SAW filter. The window area provided between the IDT fingers can be increased to promote the binding of a larger quantity of the protein as this improves the ability of the sensor to detect ultra low levels of the protein. The ability of developing an array of these sensors to detect different biomolecules will be an added advantage.

The next step for the optimized sensor is to be part of a chip where all peripheral signal generating and read-out circuitry is on-chip for a real-time smart card or tag biosensor.

Bibliography

[1] K.V. Dyke, C.V. Dyke and K. Woodfork (Eds.), *Luminescence Biotechnology: Instruments and Applications*. Boca Raton, FL: CRC Press, 2002.

[2] F.S. Ligler, C.R. Taitt, *Optical Biosensors: Present and Future*. Amsterdam: Elsevier Science, 2002.

[3] L.J. Kricka, J. Strobel and P. E Stanley, "Bioluminescent fusion conjugates and bioluminescent immunoassays: 1988-1998", *The Journal of Biological and Chemical Luminescence*, vol.14, no.1, pp. 39-46, 1999.

[4] V. Lopez-Avila and H. H. Hill, "Field Analytical Chemistry" *Analytical Chemistry,* vol. 69, pp. 289R-305R, 1997.

[5] J. Janata, M. Josowicz, P. Vanysek, and D. M. DeVaney, "Chemical Sensors" *Analytical Chem*istry, vol. 70, pp. 179R-208R, 1998.

[6] C.L. Boozer, Q. Yu, S. Chen, C.Y. Lee, J. Homola, S.S. Yee, and S. Jiang, "Surface Functionalization for Self-Referencing Surface Plasmon Resonance (SPR) Biosensors by Multi-Step Self Assembly", *Sensor and Actuators B*, vol. 90, no. 1, pp. 22-30, 2003.

[7] D. Marazuela and M.C. Moreno-Bondi, "Fiber-optic biosensors – an overview", *Analytical and Bioanalytical Chemistry*, vol. 372, no. 5-6, pp. 664-82, 2002.

[8] G. Patounakis, K.L. Shepard and R. Levicky, "Active CMOS array sensor for time-resolved fluorescence detection", *IEEE Journal of Solid-State Circuits*, vol. 41, no. 11, pp. 2521-30, 2006.

[9] H. Eltoukhy, K. Salama and A.E. Gamal, "A 0.18μm CMOS bioluminescence detection lab-on-chip", *IEEE Journal of Solid-State Circuits*, vol. 41, no.3, pp. 651-652, 2006.

[10] G. Sauerbrey, "The use of quartz oscillators for weighing thin layers and for microweighing", *Zeitschrift für Physikalische Chemie.*, vol. 155 pp.206-222.1959.

[11] A. Janshoff, H. Galla and C. Steinem, "Piezoelectric Mass-sensing devices as biosensore- An alternative to optical biosensors?", *Angewandte Chemie*, vol. 39, no. 22, pp. 4004-4032, 2000.

[12] B.A. Cavic, G.L. Hayward and M. Thompson, "Acoustic waves and the study of biochemical macromolecules and cells at the sensor–liquid interface", *Analyst*, vol. 124, pp. 1405-1420, 1999.

[13] A. F. Collings and F. Caruso, "Biosensors: recent advances", *Reports on Progress in Physics*, vol. 60, pp. 1397-1445, 1997.

[14] F Li, J. Wang, T. Shun and Q. Wang," Quartz Thickness Shear Mode Resonators for Living Cells Based Functional Biosensors**",** *Proceedings of the IEEE Ultrasonics Symposium,* pp. 333-338, 2004.

[15] E.V. Olsena, S.T. Pathiranab, A.M. Samoylovb, J.M. Barbareea, B.A. Chinc, W.C. Neelyd, V. Vodyanoyb, "Specific and selective biosensor for Salmonella and its detection in the environment", *Journal of Microbiological Methods*, vol. 53 pp. 273– 285, 2003.

[16] B.A. Cavic and M. Thompson , "Protein adsorption to organosiloxane surfaces studied by acoustic wave sensor", *Analyst*, vol. 123, 2191–2196, 1998.

[17] D.D. Stubbs, L.Sang-Hun and W.D. Hunt, "Molecular recognition for electronic noses using surface acoustic wave immunoassay sensors", *IEEE sensors*, vol. 2, no. 2, pp. 294-300, 2002.

[18] R.P. O'Toole, S.G. Bums, G. J. Bastiaans and M.D. Porter, "Thin Aluminum Nitride Film Resonators: Miniaturized High Sensitivity Mass Sensors", *Analytical Chemistry*, vol. 64, pp. 1289-1294, 1992,

[19] J.J. Caron, J.C. Andle and J.F. Vetelino, "Surface acoustic wave substrates for gas sensing applications" *Proceedings of the IEEE Ultrasonics Symposium*, vol. 1, pp. 461-466, 1995.

[20] R.M. White., P.J. Wicher, S.W. Wenzel and E.T. Zeller, "Plate mode ultrasonic oscillator sensors", *IEEE Transactions on Ultrasonics Ferroelectrics and Frequency Control,* vol. 34, pp. 162-71, 1987.

[21] M. J. Vellekoop, G. W. Lubking, P. M. Sarro and A. Venema, "Evaluation of liquid properties using a silicon lamb wave sensor", *Sensors Actuators A*, vol. 43, pp. 175-80, 1994.

[22] S. J. Martin, S.J. Ricco, T.M. Niemczyk and G.C. Frye, "Characterization of SH acoustic plate mode liquid sensors", *Sensors Actuators*, vol. 20, pp. 253-68, 1989.

[23] B. Jakoby and M. Vellekoop, "Properties of Love waves: Applications in sensors", *Smart Materials and. Structures*, vol. 6, pp. 668-679, 1997.

[24] E. Gizeli, "Design considerations for the acoustic waveguide biosensor", *Smart Materials and. Structures*, vol. 6, pp. 700-706, 1997.

[25] G.L. Harding and J. Du, “Design and Properties of quartz-based Love wave acoustic sensors incorporating silicon dioxide and PMMA guiding layers”, *Smart Materials and. Structures,* vol. 6, pp. 716-720, 1997.

[26] F. Herrmann, M. Weihnacht and S. Buttgenbach, “Properties of sensors based on shear-horizontal surface acoustic waves in $LiTaO_3/SiO_2$ and quartz/SiO_2 structures”, *IEEE Transactions on Ultrasonics Ferroelectrics and Frequency Control,* vol. 48, no.1 pp. 268-273, 2001.

[27] F. Bender, R.W. Cernosek and F. Josse, “Love-wave biosensors using cross-linked polymer waveguides on $LiTaO_3$ substrates”, *Electronics Letters*, vol. 39, no. 19, 2000.

[28] D.W. Branch and S. Brozik, "Low-Level Detection of a Bacillus Anthracis Stimulant Using Love-Wave Biosensors on 36° YX LiTaO3”, Report, Sandia National labs, SAND2003-0695, 2003.

[29] K. Tsubouchi, “ An asynchronous spread-spectrum wireless modem using SAW convolver”, *Proceedings of the International Symposium on surface acoustic wave devices for mobile communications*, pp. 215-222, 1992.

[30] A. Haddou, T. Gryba, J.E. Lefebvre, V. Sadaune, V. Zhang and E. Cattan, “Analysis of 900 MHz SAW filters on ZnO/GaAs structures”, *Proceedings of the IEEE Ultrasonics Symposium*, vol.1, pp. 91-94, 2 2000.

[31] M. Kadotaand H. Kando, “Small and low-loss intermediate frequency surface acoustic wave *filters* using zinc oxide film on quartz substrate”, *Japanese Journal of Applied Physics, Part 1*, vol.42, no.5B, pp. 3139-42, 2003.

[32] P.M. Verghese and D.R. Clarke, "Piezoelectric contributions to the electrical behavior or ZnO varistors", *Journal of Applied Physics*, vol. 87, pp. 4430-38, 2000.

[33] S. Chang, D.B.Hicks and R.C.O. Laugal, "Patterning of ZnO thin films", *Tech Digest: IEEE Solid State Sensor Actuator workshop*, vol. 41, pp.212-214, 1999.

[34] D. C. Reynolds, D. C. Loo and B. Jogai, "Optically pumped ultraviolet lasing from ZnO", *Solid State Communications*, vol. 99, pp. 873-875, 1996

[35] D.C. Look, D. C. Reynolds, J.R. Sizelove, R.L. Jones, C. W. Litton, G. Cantwell, and W.C. Harsh, "Electrical properties of bulk ZnO", *Solid State Communications*, vol. 105, pp. 399-401, 1998.

[36] T. Makino, C.H. Chia, N.T. Tuan, Y. Segawa, M. Kavasaki and A. Ohmoto A, "Exciton spectra of ZnO epitaxial layers on lattice-matched substrates", *Applied Physics Letters*, vol. 76, pp. 3549-3451, 2000.

[37] H.D Sun et .al, "Temperature dependence of Excitonic absorption spectra in ZnO/MgZnO multiquantum wells grown on lattice matched substrates" *Applied Physics Letters*, vol. 78, pp. 2464-2466, 2001.

[38] Y. Grinshpan, M. Nitzan and Y. Goldstein, "Hall mobility of electrons in quantized accumulation layers on ZnO surfaces", *Physics review B*, vol. 19, pp. 1098-1107, 1979

[39] G. Yoran, A. Many and Y. Goldstein, "Quantized electron accumulation layers on ZnO surfaces produced by low-energy hydrogen-ion implantation", *Journal of Applied Physics*, vol. 58, no. 9, pp. 3508-3514, 1985

[40] V. Bogatu, A. Goldenblum, A. Many and Y. Goldstein, “Surface quantum wells in hydrogen implanted ZnO”, *Physica Status Solidi. (b),* vol. 212, pp. 89-96, 1999

[41] F.J.V. Pressig, H. Zeng and E.S. Kim, “Measurement of piezoelectric strength of ZnO thin films in MEMS applications”, *Smart Materials and. Structures*, vol.7, pp 396-403, 1998.

[42] H. Nakahata, S. Fujii, K. Higaki, A. Hachigo, H. Kitabayashi, S. Shikata and N. Fujimori, “Diamond based surface acoustic wave devices”, *Semiconductor Science and Technology 1B,* vol. 18**,** no. 3, pp. S96-S104, 2003.

[43] V.I. Anisimkin, M. Penza, A. Valentini, F. Quaranta and L.Vasanelli, "Detection of combustible gases by means of a ZnO-on-Si surface acoustic wave (SAW) delay line", *Sensors and Actuators B: Chemical*, vol. 23, no. 2, pp. 197-201, 1995.

[44] A. Venema, E. Nieuwkoop, M.J. Vellekoop, W.J. Ghijsen, A.W. Barendsz and M.S. Nieuwenhuizen, “NO_2 Gas-Concentration Measurement with a SAW-Chemosensor”, *IEEE Transactions on Ultrasonics Ferroelectrics and Frequency Control* , vol. 34, no. 20, pp. 148-151, 1987.

[45] M. Penza, C. Martucci, V.I. Anisimkin and L. Vasanelli, “Deposition of doped and undoped ZnO thin films for gas sensors” , *Material Science Forum*, vol. 203, pp. 137-42, 1996.

[46] K. Kalantar-zadeh, D.A. Powell, S. Ippolitoand W. Wlodarski, “Study of layered SAW devices operating at different modes for gas sensing applications”, *IEEE Ultrasonics Symposium*, vol.1, pp. 191-194, 2004.

[47] S. Chu, R. Chang, C. Hong and Y. Chuang, “An investigation of preferred orientation of doped ZnO films on the 36° YX-$LiTaO_3$ substrates and fabrications

of Love-mode devices", *Surface & Coatings Technology*, vol.200, no.10, pp. 3235-4024, 2006

[48] S. Jian and S. Yuan Chu, "Characterization of ZnO thin film depositing on the 64° $LiNbO_3$ substrate and its applications on liquid sensors", I*ntegrated Ferroelectrics*, vol.69, pp. 55-63, 2005.

[49] K. Kalantar-Zadeh, W. Wlodarski, A.TrinchiIy, A. Holland and K. Galatsis, "Love Mode SAW Sensors with ZnO layer Operating in Gas and Liquid Media", *Proceedings of 2002 IEEE International Frequency Control Symposium and PDA Exhibition*, pp. 268-72, 2002.

[50] W. Water and Y. Yang, "The influence of calcium doped ZnO films on Love wave sensor characteristics", *Sensors and Actuators A (Physical)*, vol.127, no.2, pp. 360-365, 2006.

[51] W. Water, S. Wang, Y. Chen, and J. Pu, "Calcium and Strontium Doped ZnO Films for Love Wave Sensor Applications", *Integrated Ferroelectrics*, vol. 72, pp. 13–22, 2005

[52] Krishnamoorthy S. and Iliadis A.A., Development of high frequency ZnO/SiO_2/Si Love mode surface acoustic wave devices, Solid-State Electronics, Volume 50, Issue 6, June 2006, 1113-1118

[53] M. A. Febbraioand B.K. Pedersen BK, "Contraction-induced myokine production and release: is skeletal muscle an endocrine organ?", *Exercise Sport Science Review* , vol. 33, no. 3, pp. 114-119, 2005.

[54] A.K. Abbas, A.H. Lichtman and J.S. Pober, *Cellular and Molecular Immunology.* Philadelphia, PA: Saunders, 1997.

[55] J.K. Kiecolt-Glaser, K.J. Preacher, R.C. MacCallum, C. Atkinson, W.B. Malarkey, and R. Glaser," Chronic stress and age-related increases in the proinflammatory cytokine IL-6**"**, *Proceedings of the National Academy of Sciences*, vol. 100, no.15, pp. 9090-909, 2003.

[56] H.Z. Wu, K.M. He, D.J. Qiu and D.M. Huang , "Low-temperature epitaxy of ZnO films on Si(001) and silica by reactive e-beam evaporation*", Journal of Crystal Growth*, vol. 217, pp 131-137, 2000.

[57] Z. Yingxue, S. Xianghua, Y. Gencai, Z. Xinyi, Y. Wensheng, W. Shiqiang and X. Yaning, "Growth and characterization of ZnO thin film prepared by molecular-beam epitaxy on Si(100)", *Nuclear Techniques*, vol.26, no.1, pp. 9-12, 2003.

[58] H. Kim, K.S. Kim and C. Lee, "Low temperature growth of ZnO thin film on Si(100) substrates by metal organic chemical vapor deposition", Journal of *Materials Science Letters*, vol. 22, no. 15, pp. 1117-1118, 2003.

[59] Y. Zhang, Y. Cui, B. Zhang, H. Zhu, W. Li, Y. Chang, S. Yang and G. Du, "ZnO thin film grown on p-Si substrates by MOCVD", *Journal of Synthetic Crystal*, vol.34, no.6, pp. 1137-40, 2005.

[60] K. Tabuchi, W.W. Wenas, A. Yamada, A , M. Konagai, and K. Takahashi, "Optimization of ZnO films for amorphous silicon solar cells", *Japanese Journal of Applied Physics, Part 1,* vol.32, no.9A, pp. 3764-9, 1993.

[61] S.H. Jeong, B.S. Kim and B.T. Lee, "Photoluminescence dependence of ZnO films grown on Si(100) by radio-frequency magnetron sputtering on the growth ambient", *Applied Physics Letters* , vol. 82, no. 16, pp. 2625-2627, 2003.

[62] J. Li , S. Wu and J. Kang, "ZnO films deposited by RF magnetron sputtering", *Proceedings of the 13th International Conference on Semiconducting and Insulating Materials*, pp. 77-80, 2004.

[63] X. W. Sun and H. S. Kwok, "Optical properties of epitaxially grown zinc oxide films on sapphire by pulsed laser deposition", *Journal of Applied Physics*, vol. 86, no. 1, pp. 408-411, 1999.

[64] D. B. Chrisey and G. K. Hubler, *Pulsed Laser Deposition of Thin Films*, John Wiley & Sons, New York, 1994.

[65] R.D. Vispute, V. Talyansky, Z. Trajanovic, S. Choopun, M. Dawnes, R. P. Sharma, "High quality crystalline ZnO buffer layers on sapphire for pulsed laser deposition of nitrides", *Applied Physics Letters*.. vol. 70, pp.2735, 1997.

[66] S. Krishnamoorthy, A.A. Iliadis, A. Inumpudi., S. Choopun, R.D. Vispute and T. Venkatesan, Observation of resonant tunneling action in ZnO/Zn0.8Mg0.2O devices, *Solid-state Electronics,* vol. 46, pp. 1633, 2002.

[67] J. Zhao, X. Li, J. Bian, W. Yu and X. Gao, "Structural, optical and electrical properties of ZnO films grown by pulsed laser deposition (PLD)", *Journal of Crystal Growth*, vol.276, no.3-4, pp. 507-12, 2005.

[68] Z. Xu, H. Deng, J. Xie, Y. Li, Y. Li, X. Zu and S. Xue, "Photoconductive UV detectors based on ZnO films prepared by sol-gel method", *Journal of Sol-Gel Science and Technology,* vol.36, no.2, pp. 223-6, 2005.

[69] Y. Huang, L. Meidong, Z. Yike, L. Churong, X. Donglin and L. Shaobo, "Preparation and properties of ZnO-based ceramic films for low-voltage varistors

by novel sol-gel process", *Materials Science & Engineering B*, vol.B86, no.3, pp. 232-6, 2001.

[70] T.J. Bukowski, K. McCarthy, F. McCarthy, G. Teowee, T.P. Alexander, D.R. Uhlmann, J.T. Dawley and B.J.J Zelinski, "Piezoelectric properties of sol-gel derived ZnO thin films", *Integrated Ferroelectrics*, vol.17, no.1-4, pp. 339-47, 1997.

[71] U. Rossler and L. Bornstein, *Numerical Data and Functional Relationships in Science and Technology: Semiconductors*, vol. III,: Springer Verilog, Berlin, 1999.

[72] S. Choopun , R. D. Vispute, W. Noch, A. Balsamo, R.P. Sharma, T. Venkatesan, T, A.A. Iliadis and D.C. Look, "Oxygen pressure-tuned epitaxy and optoelectronic properties of laser-deposited ZnO films on sapphire", *Applied Physics Letters*, vol.75, no.25, pp. 3947-9, 1999.

[73] M. Okoshi, K. Higashikawa, and M. Hanabusa, "Pulsed laser deposition of ZnO thin films using a femtosecond laser", *Applied Surface Science*, vol.154-155, pp. 424-7, 2000.

[74] M. Zerdali, S. Hamzaoui, F. H. Teherani and D. Rogers, "Growth of ZnO thin film on SiO_2/Si substrate by pulsed laser deposition and study of their physical properties", *Materials Letters*, vol.60, no.4, pp. 504-8, 2006.

[75] M. Kumar, M, R.M. Mehra, A. Wakahara, M. Ishida, and A. Yoshida, "Pulsed laser deposition of epitaxial Al-doped ZnO film on sapphire with GaN buffer layer", *Thin Solid Films*, vol.484, no.1-2, pp. 174-83, 2005.

[76] Wiedeman L and Helvajian, H, "Laser photodecomposition of sintered $YBa_2/Cu_3/O_{6+}$ ejected species population distributions and initial kinetic energies for the laser ablation wavelengths 351, 248, and 193 nm", *Journal of Applied Physics,* vol.70, no.8, pp. 4513-23, 1991.

[77] W. Yang, "Wide bandgap MgZnO semiconducting thin films and applications to solar/visible blind ultraviolet photodetectors", Doctoral dissertation, University of Maryland, College Park, 2002.

[78] E. Millon, O. Albert, J.C. Loulergue, J. Etchepare, D. Hullin, W. Seiler, and J. Perriere, "Growth of heteroepitaxial ZnO thin films by femtosecond pulsed-laser deposition", *Journal of Applied Physics*, vol.88, no.11, pp. 6937-9, 2000.

[79] M. Okoshi, K. Higashikawa and M. Hanabusa, "395-nm and 790-nm femtosecond laser ablation of aluminum-doped zinc oxide", *Proceedings of the SPIE Engineering* , vol.4088, pp. 25-8, 2000.

[80] P. R. Willmott and J. R. Huber, "Pulsed laser vaporization and deposition", *Review of Modern Physics*, vol. 72, pp 315-328, 2000.

[81] B. Lewis and J.C. Anderson, *Nucleation and Growth of Thin Films*: Academic Press, London, 1978.

[82] K. Siegbahn, *ESCA Applied to Solids*: Almqvist and Wiksells, Uppsala, Sweden, 1967.

[83] T.L. Barr, *Modern ESCA: The principles and Practice of X-ray Photoelectron spectroscopy*: CRC Press, Boca Raton, 1994.

[84] B.D. Cullity, *Elements of X-ray Diffraction*: Addison-Wesley, New York, 1981.

[85] H.P. Klug and L. E. Alexander, *X-ray Diffraction for Polycrystalline and Amorphous Materials*: Wiley, New York, 1982.

[86] S. Perkowitz, *Optical Characterization of Semiconductors: Infrared, Raman and Photoluminescence Spectroscopy*: Academic Press Inc, San Diego, 1993.

[87] P. Dawson, G. Duggan, H. I. Ralph and K. Woodbridge, "Free excitons in room-temperature photoluminescence of GaAs-$Al_xGa_{1-x}As$ multiple quantum wells" *Physics Review* B, vol. 28, no. 12, pp. 7381-83, 1983.

[88] R.A. Smith, *Semiconductors*: Oxford University Press p.109, Second Edition (1978)

[89] R. D. Vispute, V. Talyansky, Z. Tranjonovic, S. Choopun, M. Downes, R.P. Sharma, T. Venkatesan, M. C. woods, R.T. Lareau, K.A. Jones and A.A. Iliadis, "High quality crystalline ZnO buffer layers on sapphire (001) by pulsed laser deposition for III–V nitrides", *Applied Physics Letters*, vol. 70, no.20 , pp. 2735-37,1997.

[90] R. E. Leuchtner," Mass spectrometry and photoionization studies of the ablation of ZnO: ions, neutrals, and Rydbergs", *Applied Surface Scie*nce, vol. 127, pp. 626-32, 1998.

[91] Y.Y. Villanueva, L. Da-Ren, and C. Pei, "Pulsed laser deposition of zinc oxide" , *Thin Solid Films*, vol.501, no.1-2, pp. 366-9 2006.

[92] F.K. Shan, B.C. Shin, S.W. Jang, Y.S.Yu, "Substrate effects of ZnO thin films prepared by PLD technique", *Journal of the European Ceramic Society*, vol.24, no.6, pp. 1015-18 2004.

[93] Z. Wang, L. Hu, J. Zhao, J. Sun and Z. Wang, "Effect of the variation of temperature on the structural and optical properties of ZnO thin films prepared on Si (111) substrates using PLD" *Vacuum*, , vol.78, no.1, pp. 53-7, 2005.

[94] Y.S. Yu, N. Gopalakrishnan, B.C Shin, H.S. Lim and G.Y. Kim, "Comparison of ZnO:GaN films on Si(111) and Si(100) substrates by pulsed laser deposition", *Physica B*, vol.376, pp.756-759, 2006.

[95] S.S. Kim and B. Lee, "Effects of oxygen pressure on the growth of pulsed laser deposited ZnO films on Si(001)", *Thin Solid Films*, vol. 446, no.2, pp. 307-12, 2004.

[96] F.K. Shan, G.X. Liu, W.J Lee, G.H. Kim, I.S Shin, B.C. Shin and Y.C. Kim, "Transparent conductive ZnO thin films on glass substrates deposited by pulsed laser deposition" , *Journal of Crystal Growth*, vol.277, no.1-4, pp. 284-92, 2005.

[97] S. Jeong, B. Kim and B. Lee, "Photoluminescence dependence of ZnO films grown on Si(100) by radio-frequency magnetron sputtering on the growth ambient", *Applied Physics Letters*, vol. 82, no. 16, pp. 2625-2627, 2003.

[98] E.G. Bylander, "Surface effects on the low-energy cathodoluminescence of zinc oxide", *Journal of Applied* Physics, vol. 49, pp. 1188-95, 1978

[99] K. Vanheusden, C.H. Seager, W.L. Warren, D.R. Tallant and J.A. Voiget, "Correlation between photoluminescence and oxygen vacancies in ZnO phosphors", *Applied Physics Letters*, vol. 68, pp. 403-405, 1996.

[100] B.Lin, Z. Fu and Y. Zai, "Green luminescent center in undoped zinc oxide films deposited on silicon substrates", *Applied Physics Letters*, vol. 79, pp. 943-945, 2001.

[101] Y.Y. Villanueva, D. Liu and P.T. Cheng, "Pulsed laser deposition of zinc oxide ", *Thin Solid Films*, vol.501, no.1-2, pp. 366-369, 2006.

[102] L. J. Martinez-Miranda, J.J. Santiago-Aviles, W.R. Graham, P.A. Henley and M.P. Siegal, "Xray structural studies of epitaxial yttrium silicide on Si (111)", *Journal of Materials Research*, vol. 9, no. 6, pp. 1434-1440, 1994.

[103] M.F. Seigal, L.J. Martinez-Miranda and M.P. Siegal, "A study of strain in thin epitaxial films of yttrium silicide on Si(111)", *Journal of Applied Physics*, vol. 75, no 3, pp.1517-1519, 1994.

[104] M. Zerdali, S. Hamzaoui, F.H. Tehrani and D. Rogers, "Growth of ZnO thin film on SiO_2Si substrate by pulsed laser deposition and study of their physical properties*",* *Materials Letters*, vol..60, no.4, pp. 504-508, 2006.

[105] M. Rusop, K. Uma, T. Soga and T. Jimbo, "Post-growth annealing of zinc oxide thin films pulsed laser deposited under enhanced oxygen pressure on quartz and silicon substrates", *Materials Science & Engineering B*, vol.127, no.2-3, pp. 150-153, 2006.

[106] J.N. Zeng, J.K. Low, Z. M. Ren and T. Liew, "Effect of deposition conditions on optical and electrical properties of ZnO films prepared by pulsed laser deposition", *Applied Surface Science*, vol.197-198, pp. 362-367, 2002.

[107] D. M. Bagnall, Y. F. Chen, Z. Zhu, T. Yao, S. Koyama, M. Y. Shen, and T. Goto , "Optically pumped lasing of ZnO at room temperature", *Applied Physics Letters*, vol. 70, pp. 2230-2234, 1997.

[108] D.C. Look, B. Claffin, I.. Alivov, and SJ Park ,"The future of ZnO light emitters", *Physics Status Solidi A*, vol. 201, no.10, pp. 2203-2212, 2004.

[109] X.L.Guo, J.H..Choi, H..Tabata and T..Kawai, "Fabrication and Optoelectronic Properties of a Transparent ZnO Homostructural Light-Emitting Diode", *Japanese Journal of Applied Physic*s, vol. 40, pp. L177-L180, 2001.

[110] M.H. Huang, S. Mao, H. Feick, H. Yan, Y. Wu, H. Kind, E. Weber, R. Russo, P. Yang, "Room-Temperature Ultraviolet Nanowire Nanolasers", *Science*, vol. 292, pp. 1897-1899, 2001.

[111] R. F. Service, "Materials Science: Will UV Lasers Beat the Blues?", *Science*, vol. 276, no. 5314, p. 895, 1997.

[112] D.C. Look, "Electrical and optical properties of p-. type ZnO", Semiconductor *Science and Technology*, vol. 20, no. 4, pp. S55-61, 2005.

[113] Xiong G, Wilkinson J, Mischuck B, Tuzemen S, Ucer KB and. Williams RT, "Control of *p*- and *n*-type conductivity in sputter deposition of undoped ZnO**",** *Applied Physics Letters*, vol. 80, pp.1195-1197 , 2002.

[114] Min-Suk Oh, Sang-Ho Kim, Seong-Ju Park and Tae-Yeon Seong, "Type conversion of intentionally undoped ZnO layers grown by pulsed laser deposition" , *Superlattices and Microstructures*, vol. 39, no. 1-4, pp. 130-137, 2006.

[115] K. Ellmer, "Resistivity of polycrystalline zinc oxide films: current status and physical limit", *Journal of Physics D: Applied Physics*, vol. 34, no. 21, pp.3097-3108, 2001.

[116] N. Brilis, D. Tsamakis, H. Ali, S. Krishnamoorthy and A. A. Iliadis, "Acceptor band and hopping conduction in p-type undoped ZnO films grown by pulsed laser deposition on (100) Si substrates", *Journal of Applied Physics*, submitted.

[117] N.F. Mott, "Conduction in glasses containing transition metal ions", *Journal of Non-Crystalline Solids*, vol 1, no. 1, pp. 1-17, 1968.

[118] D.C. Look, D.C. Reynolds, W. Kim, O. Aktas, A. Botchkarev, A. Salvador and H. Morkoc, "Deep-center hopping conduction in GaN**",** *Journal of Applied Physics*., vol. 80, no.5, pp. 2960-2963 ,1996.

[119] Y. Zhan, Y. Fung, H. Sun, D. Zhu, and S. Yao, "Study of protein adsorption on polymer coatings surface by combining quartz crystal microbalance with electrochemical impedance methods", *Sensors and Actuators B, Chemical,* vol.108, no.1-2, pp. 933-942, 2005.

[120] D. Kuhlmeier, E. Rodda, L.O. Kolarik, D. N. Furlong and A. Bilitewski, "Application of atomic force microscopy and grating coupler for the characterization of biosensor surfaces", *Biosensors and Bioelect*ronics, vol.18, no.7, pp. 925-933, 2003.

[121] H. Zheng, H. Okada, S. Nojima, S. Suye and T. Hori, " Layer-by-layer assembly of enzymes and polymerized mediator on electrode surface by electrostatic adsorption" *Science and Technology of Advanced Materials*, vol.5, no.3, pp. 371-376, 2004.

[122] L. Tay, N.L. Rowell, D.J. Lockwood and R. Boukherroub "In situ monitoring of protein adsorption on functionalized porous Si surfaces", *Journal of Vacuum Science & Technology A* vol.24, no.3, pp. 747-751, 2006.

[123] H. Sone, H. Okano and S. Hosaka, "Picogram mass sensor using piezoresistive cantilever for biosensor", *Japanese Journal of Applied Physics, Part 1*, vol.43, no.7B, pp. 4663-4666, 2004.

[124] S. Mittler-Neher, J. Spinke, M. Liley, G. Nelles, M. Weisser, R. Bace, G. Wenz, and W. Knoll, “Spectroscopic and surface-analytical characterization of self-assembled layers on Au”, *Biosensors and Bioelect*ronics**,** vol. 10, pp. 903–916, 1995.

[125] N. Patel, M.C. Davies, R.J. Heaton and C.J. Roberts, S.J.B. Tendler and P.M.Williams, “A scanning probe microscopy study of the physisorption and chemisorption of protein molecules onto carboxylate terminated self-assembled monolayers”, *Applied Physics A*, vol. no. 66, pp. S569-574, 1998.

[126] L. Tedeschi, C. Domenici, A. Ahluwalia, F. Baldini and A. Meneaglia, “Antibody immobilisation on fiber optic TIRF sensor”, *Biosensors and Bioelect*ronics, vol. 19, no. 2, pp. 85-93, 2003.

[127] S. Kodera, T. Okajima, H. Iwabuki, D. Kitaguchi, S. Kuroda, T. Yoshinobu, K. Tanizawa, M. Futai and H. Iwasaki, "Detection of Protein-Protein Interactions on SiO_2/Si Surfaces by Spectroscopic Ellipsometry", *Analytical Biochemistry,* vol. 321, pp. 65-70, 2003

[128] A. Ulman, *An Introduction to Ultrathin Organic Films from Langmuir Blodgett to Self-assembly*: Academic Press, New York, 1991.

[129] S. Storri, T. Santoni, M. Minunni and M. Mascini, “Surface modifications for the development of piezoimmunosensors”, *Biosensors and Bioelect*ronics, vol. 13, no. 3-4, pp. 347-357, 1998.

[130] C. D. Bain, E.B. Troughton, Y.T. Tao, J. Evall, G,M. Whiteside and R. G. Nuzzo, “Formation of monolayer films by the spontaneous assembly of organic thiols

from solution onto gold", *Journal of American Chemical Society,* vol. 111, pp.321-335, 1989.

[131] N. Barrie and M. Rapp, "Covalent bound sensing layers on surface acoustic wave (SAW) biosensors ", *Biosensors and Bioelect*ronics, vol. 16, no. 9-12, pp. 979-987, 2001.

[132] H..Zhang and E.S. Kim, "Micromachined Acoustic Resonant Mass Sensor", *Journal of Microelectromechanical System*s, vol. 14, no. 4, pp. 699- 706, 2005.

[133] R. Gabl, H. D. Feucht, H. Zeininger, G. Eckstein, M. Schreiter, R. Primig, D. Pitzer and W. Wersing, "First results on label-free detection of DNA and protein molecules using a novel integrated sensor technology based on gravimetric detection principles", *Biosensors and Bioelect*ronics, vol. 19, no. 6, pp. 615-620, 2004

[134] M.L. Phelan and S. Nock, "Generation of bioreagents for protein chips", *Proteomics*, vol. 3, no. 11, pp. 2123-2134, 2003.

[135] J.K. Kiecolt-Glaser, K.J. Preacher, R.C. MacCallum, C. Atkinson, W.B. Malarkey, and R. Glaser," Chronic stress and age-related increases in the proinflammatory cytokine IL-6**"**, *Proceedings of the National Academy of Sciences*, vol. 100, no.15, pp. 9090-9909, 2003.

[136] A. N. Vgontzas and G.P. Chrousos, "Sleep, the hypothalamic-pituitary-adrenal axis, and cytokines: multiple interactions and disturbances in sleep disorders", *Endocrinology and Metabolism Clinics of North America*, vol. 31, no. 1, pp. 15-30, 2002.

[137] M. Sarikaya, C. Tamerler, A. Jen, K. Schulten and F. Baneyx, "Molecular biomimetics: nanotechnology through biology", *Nature Materials*, vol. 2, pp. 577-585, 2003.

[138] J. H. Hoh and P.K. Hansma, "Atomic force microscopy for high-resolution imaging in cell biology", 1992, *Trends in Cellular Biology*, vol. 2, no.7, pp. 208-213, 1992.

[139] Quantikine HS Human IL-6 Immunoassay kit manual, R&D Systems, Minneapolis, MN 55413, USA.

[140] P.F. Ruhn, S. Garver and D.S. Hage," Development of dihydrazide-activated silica supports for high-performance affinity chromatography", *Journal of Chromatography A*., vol. 669, no. 1-2, pp. 9-19, 1994.

[141] E. Topoglidis, C.J. Campbell, A.E.G. Cass and J.R. Durrant," Factors that Affect Protein Adsorption on Nanostructured Titania Films. A Novel Spectroelectrochemical Application to Sensing", *Langmuir*, vol. 17, no. 25, pp. 7899-7906, 2001.

[142] A. Schulze and J. Downward, "Navigating gene expression using microarrays - a technology review", *Nature Cellular Biology*, vol. 3, E190-195, 2001.

[143] S. S. Pathak and E. Savelkoul, "Biosensors in immunology: the story so far", *Trends in Immunology*, vol. 18, no. 10, pp. 464. 1997.

[144] C.R. Narahari, L. Randers-Eichhorn, J.C. Strong, N. Ramasubramanyan, G. Rao and D.D. Frey, "Purification of Recombinant Green Fluorescent Protein Using Chromatofocusing with a pH Gradient Composed of Multiple Stepwise Fronts", *Biotechnology Progress*., vol. 17, no.1, pp. 150-160, 2001.

[145] M. Nisnevitch and M.A. Firer, “The solid phase in affinity chromatography: strategies for antibody attachment”, *Journal of Biochemistry and Biophysics Methods,* vol. 49, pp. 467-480, 2001.

[146] F. Zhang, X. Wang, S. Ai, Z. Sun, Q. Wan, Z. Zhu, Y. Xian, L. Jin and K. Yamamoto, *Analytical Chima Acta*, vol. 519, pp. 155-160, 2004.

[147] Y. Okahata, O. Shimizu and H. Ebato, “Detection of odorous substances by using a lipid-coated quartz crystal microbalance”, *Bulletin of the Chemical Society of Japan*, vol. 60, no. 11, pp. 3082-3088, 1990.

[148] N.J. Geddes, E.M. Pashinger, D. N. Furlong, Y. Ebara. Y. Okahata. K. A. Than and J. Edgar, “Piezoelectric crystal for the detection of immunoreactions in buffer solutions”, *Sensors Actuators B*, vol.. 17, pp. 125-31, 1994.

[149] K. Bodenhofer, A.Hierlemann, G. Noetzel, U.Weimer and W. Gopel, “Comparison of mass-sensitive devices for gas sensing: bulk acoustic wave (SAW) and surface acoustic wave (SAW) transducers”, *8th Int. Conf. Solid State Sensors Actuators and Eurosensors IX Tech. Digest*, vol. 2, pp. 728-31, 1995.

[150] T. W. Schneider and S.J. Martin, “Influence of compressional wave generation on thickness-shear mode resonator response in a fluid”*, Analytical Chemistry,* vol.67, pp. 3324-3335, 1995.

[151] R.M.White, “Introductory Lecture Acoustic interactions from Faraday's crispations to MEMS”, *Faraday Discussion,* vol.107, no. 1, pp. 1-13, 1997.

[152] S.J.Martin, S.J. Ricoo, T.M. Niemczyk and G.C. Frye 1989 “Characterization of SH acoustic plate mode liquid sensors”, *Sensors and Actuator, A*, pp. 253-268, 1989.

[153] R.L. Baer, C.A. FLory, M. Tom-Moy and D.S. Solomon, "STW chemical sensors", *Proceedings of the IEEE Ultrasonics Symposium.,* pp. 193-298, 1992.

[154] J. Du, G.L.Hargding, J.A. Oglivy, P.R. Dencher and M. Lake, "A study of Love wave acoustic sensors", *Sensors and Actuators, A 56*, pp. 211-219, 1996.

[155] E. Gizeli, A.C. Stevenson, N.J, Goddard, C.R. Lowe and A.C. Stevenson, "A novel Love plate acoustic sensor utilizing polymer overlayers", *IEEE transactions on Ultrasonics, Ferroelectrics and. Frequency. Control.* vol.39, pp. 657-659, 1992.

[156] G. Kovas, G.W. Lubic, M.J. Vellekoop and A. Venema, "Love waves for biochemical sensing in liquids", *Sensors Actuators, A 43*, pp.38-43, 1992.

[157] E. Gizeli, C.R. Lowe, M. Liley, H. Vogel, "Detection of supported lipid layers with the acoustic love waveguide device: application to biosensors", *Sensors and Actuators, B 34*, pp.295-300, 1996.

[158] Nakahata et al. "Diamond based surface acoustic wave devices" Semi. Science and Tech 1B (2003).

[159] S.Y. Chu, W. Water and J.T. Liaw, "A Study of Love Wave Acoustic Sensors in ZnO/Quartz Structure", *Integrated Ferroelectrics*, vol. 44, no. 1, pp. 91-100, 2002.

[160] Love A. E. H., *Some Problems of Geodynamics:* Cambridge University Press, Cambridge, 1967.

[161] Morgan D. P., *Surface-Wave Devices for Signal Processing* : Elsevier, New York), 1991.

[162] C.R. Gorla, N.W. Emanetoglu, S. Liang, W. E. Mayo, Y. Lua and M. Wraback, "Structural, optical, and surface acoustic wave properties of epitaxial ZnO films grown on $[1\bar{1}20]$ Sapphire by metalorganic chemical vapor deposition", Journal of Applied Physics, vol. 85, no. 51, pp. 2595-602, 1999.

[163] E.J. Staples, J. S. Schoenwald, R.C. Rosenfeld and C.S. Hartmann, "UHF surface acoustic wave resonators," *Proceedings of the. IEEE Ultrasonics Symposium*, pp.245-252, 1974.

[164] C. K. Campbell, *Surface Acoustic Wave Devices for mobile and wireless communications:* Academic Press, London, 1998.

[165] M. Ueda, J. Tsutsumi, S. Inoue, Y. Iwamoto, M. Miura, T. Matsuda , O. Ikata and Y. Satoh, "High Performance SAW Antenna Duplexer using Ultra-Low-Loss Ladder Filter and DMS for 1.9GHz US PCS", *Proceedings of the 2nd International Symposium on Acoustic Wave Devices for Future Mobile Communication Systems*, pp. 261-264, 2004.

[166] G. McHale, M.I. Newton and F. Martin, "Theoretical mass sensitivity of Love wave and layer guided acoustic plate mode sensors", *Journal of Applied Physics*, vol. 91, no. 12, pp. 9701-9710, 2002.

[167] R. Srivastava and A. Mansingh, "Surface acoustic wave transduction in the ZnO-SiO_2-Si structure", *Journal of Physics D: Applied. Physics,* vol. 21, pp. 1535-1536, 1988.

[168] E. Gizeli, N.J. Goddard, C.R. Lowe and A.C. Stevenson, "A Love plate biosensor utilizing a polymer layer". *Sensors and Actuators, B Chemical*, vol. 6, pp. 131–137, 1992.

[169] E. Gizeli, A.C. Stevenson, N.J. Goddard and C.R. Lowe, "A novel Love-plate acoustic sensor utilizing polymer overlayers", *Ferroelectric Freqequency Control*, vol. 39, pp. 657–659, 1992.

[170] G. Kovacs, G.W. Lubking, M.J. Vellekoop and A. Venema, "Love-wave for (bio)chemical sensing in liquids", *Proceedings of the IEEE Ultrasonics Symposium*, pp. 281–285, 1992.

[171] B. Jakoby, G.M. Insmail, M.P. Byfield and M.J. Vellekoop, "A novel molecularly imprinted thin film applied to a Love wave gas sensor", *Sensors and Actuators, A Physical*, vol. 76 pp. 93–97, 1999.

[172] G. Kovacs, M.J. Vellekoop, R. Haueis, G.W. Lubking and A. Venema, "A Love sensor for (bio)chemical sensing in liquids", *Sensors and Actuators, A Physical*, vol. 43, pp. 38-43, 1994.

[173] J.A. Ogilvy, "The mass loading sensitivity of acoustic Love wave biosensors in air", J. Phys. D: Appl. Phys. vol. 30, pp. 2497–2501, 1997.

[174] J. Du, G.L. Harding, J.A. Ogilvy, P.R. Dencher and M. Lake, "A study of Love-wave acoustic sensors", *Sensors and Actuators, A Physical*, Vol. 56, pp. 211–219, 1996.

[175] J. Du, G.L. Harding, A.F. Collings and P.R. Dencher, "An experimental study of Love-wave acoustic sensors operating in liquids", *Sensors and Actuators, A Physical*, vol. 60, pp. 54–61, 1997.

[176] J. Freudenberg, M.V. Schickfus, S. Hunklinger, "A SAW immunosensor for operation I liquid using a SiO_2 protective layer", *Sensors and Actuators, B Chemical*, vol. 76, no.1, pp. 147-151, 2001.

[177] C. Zimmermann, D. Rebiere, C. Dejous, J. Pistre, E. Chasting, R. Planade, "A Love-wave gas sensor coated with functionalized polyoxane for sensing organophosphorus", *Sensors and Actuators, B Chemical*, in press.

[178] G.L. Harding, "Mass sensitivity of Love-mode acoustic sensors incorporating silicon dioxide and silicon-oxy-fluoride guiding layers", *Sensors and Actuators, A Physical*, vol. 88, pp. 20–28, 2001.

[179] K. Kalantar-zadeh, D. Powell, W. Wlodarski, L. Li, "Study of a ZnO/64-$LiNbO_3$ SAW biosensor with a gold sensitive layer," Journal of Rare Metal Materials and Engineering, (in press).

[180] J. G. Miller and D. I. Bolef, "Sensitivity enhancement by the use of acoustic resonators in cw ultrasonic spectroscopy," *Journal of Applied Physics*, vol. 39, no. 10, pp. 4589-4593, 1968.

[181] K.K. Kanazawa and J.G. Gordon, "The oscillation frequency of a quartz resonator in. contact with a liquid", *Analytical Chima Acta*, vol. 175, pp. 99–105, 1985.

[182] S. Bruckenstein and M. Shay, "Experimental aspects of use of the quartz crystal microbalance in solution", Electrochimica. Acta, vol. 30, pp.1295-1300, 1985.

[183] A.R. Hillman. A. Jackson and S. J. Martin, "The problem of uniqueness of fit for viscoelastic films on thickness shear mode resonator surfaces", *Analytical Chemistry*, vol. 70, pp.540–549, 2001.

[184] S J. Martin, H.L. Bandey, R. W. Cernosek, A. R. Hillman and M. J. Brown, "Equivalent-circuit model for the thickness-shear mode resonator with a viscoelastic film near film resonance", *Analytical Chemistry,* vol. 72, pp.141-149, 2000.

[185] J. Du, G.L.Hargding, J.A. Oglivy, P.R. Dencher and M. Lake, "A study of Love wave acoustic sensors", *Sensors and Actuators, A Physical*, vol. 56, no.3, pp.211-219, 1996.

[186] D.S. Ballantine, R. M. White, S. J. Martin, A. Ricco, E. T. Zellers, G. C. Frye and H. Wohjlten, *Acoustic wave sensors*: Academic press, New York, 1997.

[187] M. Thompson and D. C. Stone, *Surface- Launched Acoustic Wave Sensors*, John Wiley and sons, New York, 1997.

[188] L.A. Francis, J. Friedt, R. D. Palma, C. Zhou, C. C. Bartic, A. Campitelli and P. Bertrand, "Techniques to evaluate the mass sensitivity of Love mode surface acoustic wave biosensors", *Proceedings of the IEEE Ultrasonics, Ferroelectrics and Frequency Control Conference*, pp. 241-249, 2004.

[189] G. McHale, F. Martin, and M.I. Newton, "Mass sensitivity of acoustic wave devices from group and phase velocity measurements", *Journal of Applied Physics,* vol. 92, no. 6, pp. 3368–3373, 2002.

[190] J. Xu, J. S. Thakur, F. Zhong, H. Ying, and G. W. Auner, "Propagation of a shear-horizontal surface acoustic mode in a periodically grooved AlN/Al_2O_3 microstructure", Journal of Applied Physics, vol. 96, no.1, pp. 212-217, 2004.

[191] F. Bender, R.W. Cernosek and F. Josse, "Love-wave biosensors using cross-linked polymer waveguides on $LiTaO_3$ substrates", Electronic Letter, vol. 36, no. 19, pp. 1672-1673, 2000.

[192] K. Kalantar-zadeh, W. Wlodarski, A. Trinchi, A. Holland "A novel Love mode sensor based on ZnO/ST-cut quartz crystal structure", *Sensors and Actuators A*, vol.100, pp. 135-139, 2002

[193] Krishnamoorthy S. and Iliadis A.A., "Development of high frequency $ZnO/SiO_2/Si$ Love mode surface acoustic wave devices", *Solid-State Electronics*, vol. 50, no. 6, pp.1113-1118, 2006.

[194] Kumagai, S. Yoshii, S., Yamada, K., Fujiwara, I., Matsukawa, N. and Yamashita, I., "Nanopatterning of vapor-deposited aminosilane film using EB lithography for ferritin protein adsorption", *Journal of Photopolymer Science and Technology*, vol. 18, no. 4, pp. 495-500, 2005.